The Dissertation Committee for Adrianna Brush Certifies that this is the approved version of the following dissertation:

Mechanistic Insights into Heterogeneously Catalyzed Methane Reactions

Committee:

Charles Buddie Mullins, Supervisor

Adam Heller

Simon Humphrey

Graeme Henkelman

Gyeong Hwang

Mechanistic Insights into Heterogeneously Catalyzed Methane Reactions

by

Adrianna Brush, B.S.

Dissertation

Presented to the Faculty of the Graduate School of

The University of Texas at Austin

in Partial Fulfillment

of the Requirements

for the Degree of

Doctor of Philosophy

The University of Texas at Austin

May 2017

Dedication

Dedicated to my grandfather, Norbert Leo Knue (1924-20012), Petty Officer, U.S.S. Pelias, and Professional Engineer at G.E.

The countless hours we spent troubleshooting, fixing, and building are some of my most cherished memories. You fueled the curiosity and creativity that is a fundamental aspect of who I am. This dissertation would not exist without your influence in my life. I am eternally grateful for the relationship we had.

Acknowledgements

First and foremost, I would like to thank my graduate advisor, Professor Charles Mullins for the support that he has given me over the course of my graduate career. I especially appreciate the independence and freedom that he gave me to pursue new areas of research and fabricate new equipment.

I would also like to thank my dissertation advising committee, Prof. Adam Heller, Prof. Simon Humphrey, Prof. Graeme Henkelman, and Prof. Gyeong Hwang for their time and insight throughout my graduate career.

I am grateful to have worked with a great group of labmates. I owe special thanks to Dr. Ming Pan for mentoring me my first year, Dr. Greg Mullen for building the classical catalyst reactor with me, and Dr. Wen-Yueh Yu and Edward Evans for their scientific insights and for keeping the lab fun and enjoyable to work in. I would like to thank the Mullins group as a whole for being a friendly and cooperative group.

A great deal of appreciation goes to the staff of the McKetta Department of Chemical Engineering. The equipment responsible for much of my research would not have been possible without Shallaco McDonald, Jim Smitherman, and Butch Cunningham. Kate Baird has been a phenomenal Graduate Program Coordinator. Kevin Haynes kept the gases coming that kept my experiments running. Carrie Brown was always so helpful and I enjoyed the conversations we've had. Thanks to Eddie and Ben for being on top of ordering equipment. Thanks to Randy and Jason for all their computer help.

Dr. Donggao Zhao with the Department of Geological Sciences at the University of Texas, Austin, taught me all about electron microscopy, and my second manuscript would not have been possible with him. Thanks also goes to Hugo Celio, who managed

the TGA and XPS. The talented undergraduates I worked with were instrumental in our various studies. Thanks especially to Robin DuPre, who worked with me for 2 years, as well as Shruti Kota and Jake Lam.

I would like to thank the Temple Foundation Graduate Fellowship Fund for financial support. I would also like to thank the Department of Energy and the Welsh Foundation, whose grants funded much of my research.

Finally, over the past 6 years, I have grown personally just as much as I have grown professionally. Thank you to my family and friends who have supported me throughout it all. Special thanks to my parents, Audrey Whaling, Denise Grab, Neeraja Koneru, Jon Bollinger, Ellen Line, Moni Burgin, Kevin Baldridge, and Jon Gladbach, who have been with me throughout this. I would also like to give a special thanks to the members of all the communities I have lived in or been a part of that have helped me find, love, and embrace my identity: ICC, Haus of Queer, ATXQ, QTxP, Trans & Genderqueer Social, Flipside, Nosh Pit, and DPW. A special thanks to Liz Elsen, Kristen Hogan, and all the staff and students at the UT Gender and Sexuality Center.

Mechanistic Insights into Heterogeneously Catalyzed Methane Reactions

Adrianna Brush, Ph.D.

The University of Texas at Austin, 2017

Supervisor: Charles Buddie Mullins

Catalysts play an exceptionally important role in our society. Most synthetic materials rely on a catalyst at some point during their production, and the efficiency improvements due to catalysts are key to achieving the goal of sustainable human existence. Methane reactions have become important due to methane's increasing source for energy and as a chemical feedstock. Understanding the mechanisms involved in catalyzed methane reactions will help direct future catalyst research.

In this dissertation, we investigate mechanistic aspects of methane reactions over heterogeneous catalysts. Using model studies, we explore the surface structures and mechanism of O-H bond dissociation of methanol, a methane derivative, coadsorbed with hydrogen on Au(111). Using a classical catalyst reactor, methane reforming reactions and methane dissociation over molybdenum carbide based catalysts were investigated. We determined that Ni/Mo_2C will simultaneously catalyze the Dry Methane Reforming and Steam Methane Reforming reactions, with the resulting syn-gas ratio (H_2:CO) capable of being "tuned" from 0.9 to 3.0 by adjusting the ratio of H_2O:CO_2 in the reactant oxidant mixture.

With an interest in developing transient techniques, we developed a novel apparatus capable of utilizing isotopically labeled gases more efficiently than current

designs for Steady State Isotopic Transient Kinetic Analysis (SSITKA) experiments. This more efficient design allows more experiments to be performed. Using this apparatus, we investigated the methane dissociation mechanism over commercial Mo_2C. We found that carbon exchange did not occur between the methane and the Mo_2C carbide carbon, in contradiction to previous studies' findings. Further, the dissociation of methane over Mo_2C was determined to involve a single C-H bond dissociation.

This dissertation provides insights into the mechanisms behind heterogeneously catalyzed methane reactions, particularly methane reforming reactions over Mo_2C based catalysts. In addition, valuable isotopic experimental techniques, such as SSITKA, can benefit from the efficiency improvements offered by the Pulse Injection Apparatus, facilitating more robust investigations into catalytic mechanisms and kinetics.

Table of Contents

List of Tables

List of Figures

Chapter 1: Introduction

1.1: The Importance of Methane Chemistry

Methane, also known commonly as natural gas, has emerged as an extremely important factor in the U.S., as well as the global, energy and petrochemicals industry. The U.S. Energy Information Administration projects that Natural Gas will account for 40% of U.S. energy by 2040.[1] The industrial sector is the largest consumer of natural gas, used primarily for energy generation and as a feedstock for methanol, ammonia, and fertilizer production. Methane can also be used as a feedstock for a wide range of hydrocarbon species. Interest in the use of methane for energy and chemical feedstocks has increased significantly over the past couple decades due to technological advancements, such as horizontal drilling and hydraulic fracturing, that have expanded the potentially recoverable supplies of methane.

However, use of methane as an energy source or as a feedstock for other, more valuable molecules, has a couple of significant impediments. First of all, methane cannot be liquefied at ambient temperatures, making it difficult to transport. As a result, producers must either construct miles of high pressure gas pipelines, or utilize special tankers refrigerated with liquid nitrogen, both of which add significant expense. Another strategy involves converting methane into a substance easier to transport, such as methanol.[2] However, this strategy has the same challenge as using methane as a chemical feedstock: it is difficult to efficiently convert methane into other, more useful species.

Currently, industrial conversion of methane involves two general steps: methane reforming with an oxidant to form "synthesis gas" ($CO + H_2$), and reaction of the synthesis gas to form methanol and other hydrocarbons via the Fischer-Tropsch process. This process has two major drawbacks. First, in order to make methanol, for example, methane is essentially over-oxidized to CO, then reduced back to methanol, an energy

intensive and inefficient method. Second, the equipment required for methane reforming results in high capital costs for any Gas-to-Liquids (GTL) plant. As a result, this makes GTL plants near natural gas wells uneconomical except in the most extreme circumstances, such as offshore wells or wells extraordinarily far away from ports or existing natural gas pipelines. While catalytic routes for direct oxidation of methane to methanol have been extensively researched, none has been able to achieve the conversion and selectivity required to replace the current GTL method.[3,4]

1.2: The Importance of Understanding Catalytic Mechanisms

Heterogeneous catalysts are solid materials that allow chemical reactions to occur with less energy and/or more selectivity than would have otherwise been possible. These materials are involved in the reaction, but theoretically end up unchanged at the end of the catalytic cycle. Most catalysts involve transition metal particles supported on a metal oxide support. There are a variety of mechanisms through which catalysts perform their function. Some assist in otherwise high-energy steps, such as initial bond dissociation of the reactant molecule. Others allow certain bond formation steps to be favored over others, increasing selectivity.[5]

However, many catalysts are developed and used without a good understanding of the mechanisms responsible for the efficiency or selectivity improvements. This causes much catalytic research to be primarily empirical and phenomenological, where researchers test a range of metals, supports, concentrations, and reaction conditions to determine which combination has the most promise. However, being able to understand the mechanistic reasons behind a particular catalyzed reaction allows a more focused, directed effort to improve catalytic materials. In addition, understanding the underlying mechanism of a catalytic reaction allows greater insight into the underlying kinetics,

giving direction towards possible improvements in the reaction conditions for these catalytic reactions.

Catalytic reactions, however, are complicated, and difficult to fully study and understand. The transition metal particles on the catalyst can have a wide range particle sizes, exposed crystal faces, and interactions with the support. The support, as well, can have several different morphologies and localized oxidation states that can affect the activity of a metal particle or even participate in the reaction. To tackle these complexities, investigators have developed two separate, but related, methods to study catalytic mechanisms.

Model studies utilize highly controlled catalysts and reaction conditions to precisely study a very specific catalytic condition. Experiments are performed in an Ultra-High Vacuum Chamber (pressures ~10^{-10}-10^{-9} Torr) in order to ensure tight control over the species and quantities introduced to the reactor. The catalytic material is typically a single crystal of a material, sometimes with another metal or metal oxide deposited onto or annealed into the single crystal. With this highly controlled system, precise measurements of resulting species' desorption temperatures can be made, which give insight into the bonding with the catalyst and other species on the surface.[6] In addition, the relative simplicity of the system allows the underlying chemical reaction mechanism to potentially be determined using Density Functional Theory (DFT). However, model studies suffer from a "material gap," where the vast complexity of the catalyst cannot be captured by studying one crystal face or interface. In addition, these studies suffer from a "pressure gap," where the higher pressures associated with ambient or industrial conditions change the behavior of molecules on the surface, or that a mechanism unlikely under model conditions is actually responsible for the catalytic behavior observed at ambient conditions.

On the other end of the spectrum are classical catalyst studies. These are studies that use the catalysts and reaction conditions close to or identical to industrial conditions, but on a laboratory scale. Catalysts are either bought from a commercial source or synthesized using "wet chemistry" techniques. For gas phase reactions, reactant gases are flowed through a prepared catalyst bed, heated by a heater, and the resulting products are measured with an analytical instrument, often gas chromatography and/or mass spectrometry. Development of classical catalysts tends to be primarily phenomenological. Typically, a set of catalysts is developed with a "scattershot" range of a certain property (ie, dopants, dopant concentration, etc.), and the trends in catalytic properties are determined empirically. Kinetic rates and reaction order are often determined via a series of steady state experiments at different temperatures and reactant concentrations. While classical catalyst experiments tend to determine catalytic activity and properties more similar to their ultimate industrial application, improvement and optimization of these catalysts can be slow and cumbersome without mechanistic information to direct study.[7]

1.3: Use of Isotopic Labeling in Catalyst Studies

Isotopically labeled species have been used in both model and classical catalyst studies to determine catalytic mechanisms and kinetics. In both types of studies, isotopic labeling allows researchers to probe which atoms and bonds are involved in a particular reaction, and can give insight into the mechanism involved. By using strategically placed isotopic labels on a molecule and a logical approach, one can deduce which mechanisms are possible, and which are not.[8,9] As a simple example, consider the dehydrogenation of methanol to formaldehyde in the presence of water ($CH_3OH \xrightarrow[H_2O]{} CH_2O + H_2$). If a combination of CH_3OH and D_2O were reacted together, the presence of HD would indicate that water directly participates in the reaction or can hydrogen exchange with the

methanol. Further, if CD_3OH and H_2O were reacted together, the presence of D_2 would indicate that the C-D (or C-H) bond breakage step is independent from the H-H (or H-D or D-D) bond formation step, since the other D must come from another molecule's C-D bond breakage step. Therefore, the mechanism allows a D atom to stay on the surface (either as an independent adatom or part of another molecule) long enough to find another D atom to bond with.

For model studies, these isotopic studies allow one to deduce possible mechanisms and kinetics. These studies can help guide DFT studies, and help corroborate the theoretical results with empirical observation. In addition, a common technique in model studies uses Temperature Programmed Desorption (TPD). In TPD, the temperature at which species desorb from the surface are an indication of that species' binding strength and/or the temperature at which a reaction affecting that species occurs. When a species is isotopically labeled, the kinetic isotope effect changes the bond strength and therefore any reaction kinetics associated with that atom. By comparing the desorption temperatures, conversions, and other aspects, the effect of the isotopic label can be compared to the theoretical kinetic isotope effect on proposed mechanisms and kinetics for the reaction.[6]

In classical catalyst studies, isotopic labeling is used to determine reaction kinetics and other aspects of a heterogeneously catalyzed reaction that would normally be difficult or impossible to determine by other methods. One of the more powerful techniques is Steady State Isotopic Transient Kinetic Analysis (SSITKA). In a classical catalyst reactor, a heterogeneously catalyzed reaction is brought to steady state. Then, one of the reactants is instantaneously switched to an isotopically labeled version of that reactant. An inert gas mixed into one of these reactants is used to determine the gas phase holdup, essentially the mass transport function, of the reactor system. Since the

isotopically labeled atom in the isotopically labeled reactant must work its way through the reaction mechanism and associated kinetics, there will be a delay in the emergence of the isotopically labeled atom into a product, compared to the gas phase holdup function. Simple analysis of these functions can provide several important insights, including the mean surface residence time. Combining this analysis with conversion measurements and physical properties of the catalyst, such as surface area, give a determination of the number of active species on the catalyst, as well as potential insights into the catalytic sites and mechanisms associated with the reaction. More rigorous modeling and inspection of the functions can give insights into the number of possible mechanistic pathways, whether these mechanisms are in parallel or in series, and other insights.[10,11]

1.4 An Overview of This Dissertation

My graduate career has been divided into two major areas, (1) model studies of a methane derivative, methanol, on gold and (2) investigations into methane reforming reactions over classical molybdenum carbide catalysts. While these two areas are somewhat distinct, they share a few common threads. First of all, the reactions investigated focus on methane reactions and one of the primary desired end products from methane reactions is methanol. Second, my collaborators and I have had a specific interest in studying mechanisms, particularly by using isotopically labeled reactants.

Chapter 2 focuses on the first major area of study. In this chapter, we use combinations of MeOH, MeOD, H_2, and D_2 to study methanol and hydrogen on Au(111). From these experiments, we were able to propose a methanol surface structure and mechanism for hydrogen exchange, which we were also able to extend to water and ethanol. This work was published in *Journal of Physical Chemistry: C*.[12]

In Chapter 3, we shift to the second major area of study, methane reforming reactions over molybdenum carbide catalysts. This chapter outlines the unusual characteristics of molybdenum carbide as a methane reforming catalysts, along with their unique challenges. In this chapter, we demonstrate that Ni/Mo_2C is able to simultaneously catalyze the Dry Methane Reforming reaction ($CO_2 + CH_4 \rightarrow 2CO + 2H_2$) and the Steam Methane Reforming reaction ($H_2O + CH_4 \rightarrow CO + 3H_2$), to "tune" the resulting synthesis gas ($CO + H_2$) ratio from 0.9:1 to 3:1 H_2:CO. This catalyst is able to perform this function with no evidence of coking, a major issue in methane reforming reactions, despite operating under conditions supposedly favorable for coke formation. This work has been published in *Fuel Processing Technologies*.[13]

In Chapter 4, we return to isotopic labeling techniques for insight into catalytic mechanisms and kinetics. In this chapter, a novel apparatus is described that allows Steady State Isotopic Transient Kinetic Analysis (SSITKA) studies to be performed more efficiently. With this design, researchers can better utilize the expensive isotopically labeled gases crucial to SSITKA experiments. This manuscript has been submitted to *Reaction Chemistry and Engineering*.[14] In Chapter 5, we describe how this apparatus was used to study the mechanism of methane dissociation on a commercial Mo_2C catalyst. A prior work in the literature had determined that methane could undergo facile carbon exchange with Mo_2C, indicating full methane dissociation, at temperatures above 550°C. Our studies, however, contradicted that interpretation and determined that the dissociation of methane on Mo_2C likely involves a single C-H bond dissociation at temperatures above 800°C. This work was published in *Reaction Chemistry and Engineering*.[15]

I conclude this dissertation in Chapter 6 by summarizing our key findings from these studies. In addition, I suggest future research opportunities based on our work and the equipment capabilities now present in the Mullins lab.

Chapter 2: Methanol O-H Bond Dissociation on H-Precovered Gold Originating from a Structure with a Wide Range of Surface Stability*

2.1: INTRODUCTION

Gold has generated a great deal of interest as a catalyst[16] since the discoveries of Haruta[17–19], Bond[20], and Hutchings[21] demonstrated the exceptional catalytic activity of nanostructured gold. Since then, supported gold nanoparticles have exhibited activity in a wide range of oxidation reactions, such as CO oxidation[22,23] and the water gas shift reaction[24,25]. Gold has also shown great promise in hydrogenation reactions[26], including hydrogenation of alkynes and various selective hydrogenation reactions[27–29]. However, while several fundamental studies of oxidation reactions involving gold have been performed[18,30–34], few fundamental studies of hydrogenation reactions on gold have been reported[35,36]. Key to understanding the catalytic mechanisms of hydrogenation reactions on gold is studying the fundamental interactions of hydrogen atoms and chemical reactants on the gold surface[37].

A primary impediment to performing these fundamental studies is that, while supported gold nanoparticles are able to dissociate molecular hydrogen[38], the Au(111) single crystal is not[39,40]. In order to investigate the role of gold and fundamentally study hydrogenation reactions on gold alone, hydrogen adsorption is achieved by flowing H_2 through an electron-beam heated tungsten tube in a UHV chamber, allowing atomic hydrogen adsorption on the Au(111) single crystal surface[35,41]. Using this technique to simulate the dissociation of molecular hydrogen by supported gold nanoparticles, gold's

*This work was previously published: A. J. Brush, M. Pan and C. B. Mullins, *J. Phys. Chem. C*, 2012, **116**, 20982–20989. The author of this dissertation was responsible for developing and conducting the UHV experiments and analyzing the data.

reactivity for reactions involving hydrogen can be isolated and studied.

Alcohols are an important class of molecules for study regarding their interactions with hydrogen atoms on a gold surface. The reaction of hydrogen coadsorbed with carbon monoxide to produce methanol, including methanol's interaction with hydrogen, has been studied on several other model catalysts, such as Pd(111)[42] and Ni(100)[43], as well as on supported gold catalysts[44]. Similarly, the decomposition of methanol and ethanol to produce hydrogen, among other products, has been studied for gold nanoparticles on various supports[45,46]. Previous work has also demonstrated the ability for aldehydes and alcohols to combine on a hydrogen covered gold surface to form asymmetrical ethers[47]. A key aspect of the proposed mechanism for this ether forming reaction involves the dissociation of the alcohol O-H bond on the gold surface, induced by the coadsorbed hydrogen. Additionally, hydrogen bonding networks of alcohols on a gold surface have also been discovered. Baber et al. have shown that the first adsorbed layer of methanol on a Au(111) surface forms hexamer rings, zigzag type chains, and 18 molecule rings, with the second adsorbed layer forming no discernible structure[48]. Studying how adsorbed hydrogen atoms alter these hydrogen bonding networks and affect the O-H bond can help confirm the proposed mechanisms of previous work, as well as lead to mechanistic insight for other reactions.

Here we study the interaction of methanol and hydrogen coadsorbed on a Au(111) single crystal surface. We demonstrate that this coadsorption induces an adsorbate structure, or set of structures, with a wide range of desorption energies. Using isotopically labeled reactants, we demonstrate that gold can dissociate the O-H bond, allowing hydrogen originating from the methanol O-H group to exchange with hydrogen originally adsorbed on the surface. These isotopic studies also demonstrate that the hydrogen released from a methanol molecule desorbs from the gold surface at a higher temperature

than hydrogen originating from the surface, providing insight into the adsorbate structure of the methanol-hydrogen network. Additionally, adsorbed MeOH exhibits an inhibiting effect on deuterated methanol's (MeOD) ability to hydrogen exchange, leading to more evidence of a proposed mechanism. Finally, similar isotopic studies were performed with ethanol, suggesting that this phenomenon may be common to alcohols and even O-H groups in general[41].

2.2: EXPERIMENTAL METHOD

All reactions were performed in an ultrahigh vacuum (UHV) chamber with a base pressure of ~2 X 10^{-10} Torr[35,41,49], employing a supersonic molecular beam for delivery of reactants. The chamber consists of 5 differentially pumped subchambers, including a subchamber where the supersonic molecular beam is generated and a scattering chamber equipped with a quadrupole mass spectrometer (QMS), an Auger electron spectrometer (AES), and low energy electron diffraction (LEED) optics. The Au(111) single crystal, a circular sample 12mm in diameter and 2mm thick, is mounted on two copper electrical feedthroughs in the scattering chamber and connected to a K-type (Alumel/Chromel) thermocouple. The sample can be cooled to 77K via a liquid nitrogen reservoir and resistively heated to 900K (by the supporting Mo wire) and controlled by a proportional-integral-differential (PID) controller.

Prior to each experiment, the sample surface was cleaned by exposure to a NO_2 molecular beam for two minutes while the sample temperature was held at 800 K[50]. Periodically, Ar ion sputtering was used to remove contaminants from the surface, after which the surface structure was restored by annealing the sample at 800 K for 15 minutes. Sample cleanliness and surface structure were confirmed by AES and LEED. In order to populate the gold surface with hydrogen adatoms, molecular hydrogen was

flowed through a homemade device employing a high-temperature electron-beam heated tungsten filament[51,52]. Following hydrogen adatom deposition, if used for the experiment, reactants were then deposited onto the surface via the supersonic molecular beam. Temperature-programmed desorption (TPD) data was acquired by heating the sample at a constant rate, and utilizing the QMS to detect the desorbed species. The hydrogen/deuterium relative coverage on the surface is determined by comparing the TPD peak area to that of the gold sample saturated with H/D. Similarly, the coverage of a reactant is determined by comparing the TPD peak area of the most appropriate mass fragment to that of 1ML of reactant, which is defined as the coverage exhibiting the maximum integration area for the monolayer feature without the presence of a multilayer feature.

Au(111) typically restructures into a "herringbone" 22 X √3 surface structure under ultra-high vacuum[53,54]. It has been previously shown that certain species, such as oxygen atoms, can cause the Au(111) surface to adopt a 22 X 1 surface structure with small 3D islands of gold and/or oxidized gold[55,56]. However, we do not believe that adsorption of hydrogen atoms or methanol molecules affect the Au(111) herringbone 22 X √3 surface structure. LEED of the Au(111) sample surface after adsorption of H adatoms was not significantly different from LEED of the Au(111) sample surface after reconstruction via the annealing process described above. Additionally, Baber et al. have shown with STM that Au(111) retains its herringbone 22 X √3 structure with adsorption of methanol[48].

2.3: Results and Discussion

2.3.1: Coadsorption of Methanol and Hydrogen

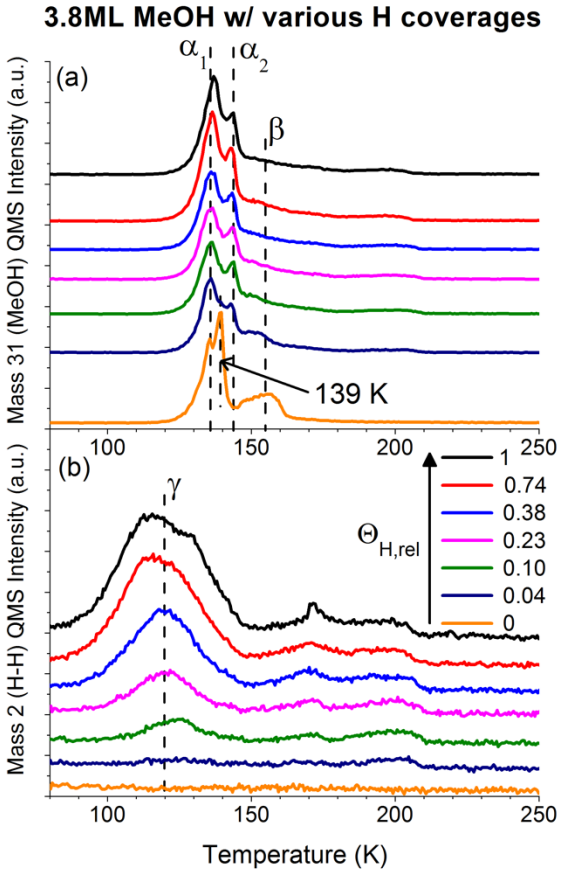

Figure 2.1: QMS spectra of MeOH/H/Au(111). 3.8 monolayers of methanol were coadsorbed with various coverages of hydrogen, as indicated by the legend. a) *m/z* = 31, indicative of methanol; b) *m/z* = 2, indicative of hydrogen. All species were adsorbed at 77 K. The heating rate was 1 K/s.

To begin exploring the interaction of methanol and hydrogen on Au(111), various coverages of hydrogen were coadsorbed with 3.8 monolayers (ML) of methanol on the Au(111) surface. Figure 2.1 displays QMS spectra for *m/z* = 31, indicative of methanol (Figure 2.1a), and *m/z* = 2, indicative of hydrogen (Figure 2.1b), for these experiments. Methanol on a clean Au(111) surface (Figure 2.1a, $\Theta_{H,rel}$ = 0) displays a monolayer feature (β), centered at 155K, and two multilayer features, centered at 136K (α_1) and

139K (α_2). This is in agreement with previous work regarding methanol on clean Au(111)[57] and Pt(111)[58] which found that methanol forms 1-2 layers of an amorphous methanol phase (α_2) on top of the monolayer, as well as a crystalline phase of bulk methanol (α_1).

Coadsorption of methanol with increasing amounts of hydrogen on the Au(111) surface causes the monolayer feature (β) to broaden into a flat "tail" feature, ranging from 148 K to 210 K. This implies that the hydrogen induces some strongly bound methanol with a wide range of adsorption energies. Additionally, the α_2 peak shifts from 139 K with no hydrogen coadsorption, to 143 K with hydrogen coadsorption, indicating that the methanol phase immediately above the monolayer layer is more strongly bound with hydrogen coadsorption. This is possibly due to an increased level of hydrogen bonding between the monolayer and the amorphous layer, suggesting that the hydrogen adatoms may alter the monolayer hydrogen bonding networks reported by Baber et al.[48] This could be due to a change in the orientation of the monolayer methanol molecules, allowing a lone pair or H from the O-H group to more easily hydrogen bond with the amorphous layer above the monolayer. It should be noted that the α_1 crystalline phase did not experience a change in desorption temperature, indicating that hydrogen coadsorption did not affect the crystalline phase.

The *m/z* = 2 spectra in Figure 2.1b gives insight into the behavior of hydrogen in this system. Low hydrogen coverages ($\Theta_{H,rel} < 0.1$) show that hydrogen desorbs with broad features centered at 170 K and 200 K. With increasing coverages, these features form a broad flat desorption feature from 148 K to 210 K, coinciding with the methanol "tail." For coverages $\Theta_{H,rel} = 0.10$ and higher, a large broad desorption peak centered at 120 K also appears, attributed to simple hydrogen adatom recombination, which would desorb at 115 K for hydrogen adsorbed on the clean Au(111) surface[35]. This feature is

labeled as "γ" in Figure 2.1b, and will henceforth be referred to as the γ feature in this report. These features suggest that the hydrogen adatoms preferentially interact with the methanol molecules to create adsorbate structure(s) with a broad range of desorption temperatures. Above a critical coverage required to saturate the interaction, the remaining hydrogen adatoms recombine and desorb as if on a clean Au(111) surface, although with the peak temperature shifted about 5 K higher.

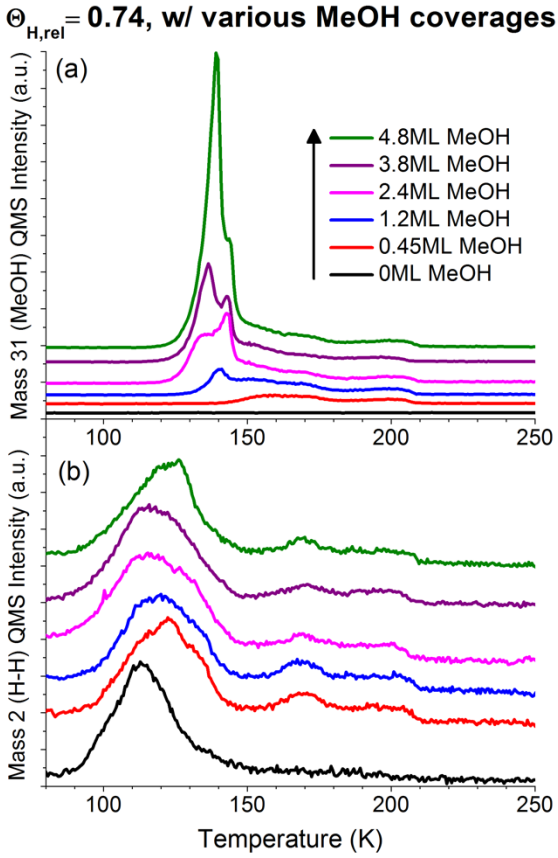

Figure 2.2: QMS spectra of MeOH/H/Au(111). $\Theta_{H,rel}$ = 0.74 of hydrogen were coadsorbed with various coverages of methanol, as indicated by the legend. a) *m/z* = 31, indicative of methanol; b) *m/z* = 2, indicative of hydrogen. All species were adsorbed at 77 K. The heating rate was 1 K/s.

Next, we coadsorbed a fixed amount of hydrogen ($\Theta_{H,rel}$ = 0.74) with various amounts of methanol. Figure 2.2 displays the QMS spectra for *m/z* = 31 (Figure 2.2a),

indicative of methanol, and *m/z* = 2 (Figure 2.2b), indicative of hydrogen, for these experiments. For methanol coverages below ~1 monolayer, methanol desorbs in a broad, flat "tail" feature ranging from 145 K to 210 K, similar to the tail observed in Figure 2.1a. With increasing methanol coverage, the methanol spectra first displays a feature at 143 K, corresponding to the α_2 feature mentioned earlier. This confirms that the α_2 phase forms immediately above the monolayer, as suggested above. Similarly, a feature appears at 135-139 K for coverages greater than ~2 monolayers, corresponding to the α_1 crystalline phase desorption.

The *m/z* = 2 spectra for $\Theta_{H,rel}$ = 0.74 of hydrogen on clean Au(111) (Figure 2.2b, 0ML MeOH) displays a single desorption feature at 115 K, corresponding to simple hydrogen adatom recombination. This γ feature broadens and shifts to 120 K with methanol coadsorption, similar to a phenomenon reported by Pan et al. for H_2O and H coadsorbed on Au(111)[41]. They suggest this is due to an increased diffusion length for hydrogen adatom recombination caused by the adsorbed water. Since several similar phenomena are observed in the MeOH/H/Au(111) and H_2O/H/Au(111) systems, it is reasonable to speculate that the shift in the MeOH/H/Au(111) system is also due to an increased diffusion length for hydrogen adatom recombination. Additionally, the strongly-bound broad hydrogen desorption feature from 150K to 210 K, noted in Figure 2.1, appears with sub-monolayer coverages of methanol. This lends evidence to the hypothesis that the "tail" feature is caused by a favored adsorbate structure induced by interaction of hydrogen adatoms and the methanol monolayer.

2.3.1: H/D Studies to explore Hydrogen Exchange

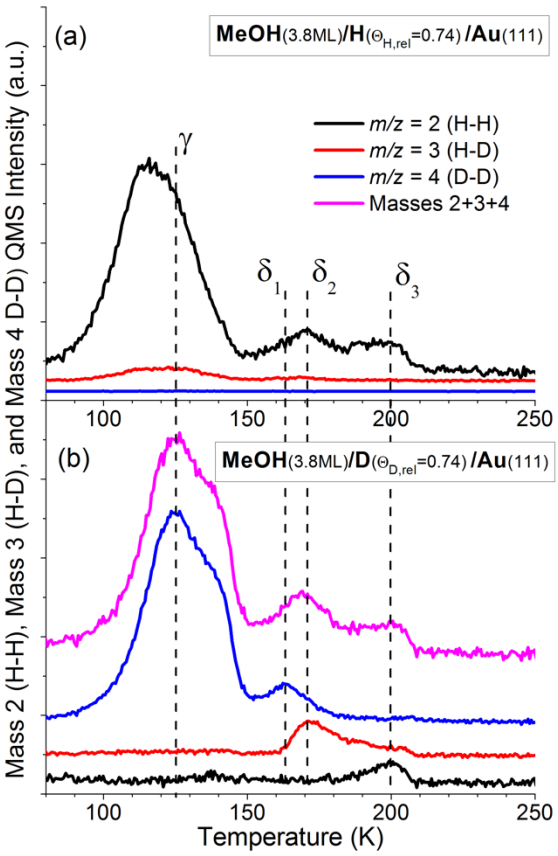

Figure 2.3: QMS spectra of *m/z* = 2, 3, and 4 for methanol (MeOH) coadsorbed with hydrogen (H) or deuterium (D) on Au(111). "Masses 2+3+4" is the composite spectra of adding the signals of *m/z* = 2, 3, and 4 together from 3b. a) 3.8 monolayers of MeOH coadsorbed with $\Theta_{H,rel} = 0.74$ of hydrogen; b) 3.8 monolayers of MeOH coadsorbed with $\Theta_{D,rel} = 0.74$ of deuterium. All species were adsorbed at 77 K. The heating rate was 1 K/s.

In order to further illuminate the nature of the interaction between methanol and hydrogen on gold, as well as probe for hydrogen exchange between methanol and adsorbed hydrogen, isotopic studies were performed. Methanol (MeOH) was coadsorbed with deuterium (D) on the Au(111) surface and the resulting spectra were compared to the MeOH/H/Au(111) experiments described above. Figure 2.3 depicts the QMS spectra for *m/z* = 2, *m/z* = 3, and *m/z* = 4, which correspond to H-H, H-D, and D-D desorption,

respectively, for MeOH/H/Au(111) (Figure 2.3a) and MeOH/D/Au(111) (Figure 2.3b). Figure 2.3a displays a *m/z* = 2 (H-H) spectra similar to those in Figures 2.1 and 2.2, along with a featureless *m/z* = 4 (D-D) spectra, which is expected. The *m/z* = 3 (H-D) spectra displays a small feature centered at ~120K, which is attributed to D impurities in the gas handling plumbing.

Regarding coadsorption of MeOH and D, the D-D desorption spectra has similarities with the H-H spectra for MeOH/H/Au(111). The large feature at 125 K is the same γ feature, corresponding to D adatom recombination, which desorbs at a slightly higher temperature than H, a phenomenon seen previously on clean Au(111)[35]. However, the "tail" appears to have split into 3 distinct features: 1) a D-D desorption feature centered around 162 K, denoted "δ_1," 2) a H-D feature centered around 170 K, denoted "δ_2," and 3) a H-H feature centered at 200 K, denoted "δ_3." The presence of H-D and H-H features prove conclusively that the H-precovered Au(111) surface can dissociate the methanol O-H bond and allow hydrogen exchange between methanol and hydrogen adatoms. Additionally, if the *m/z* = 2, *m/z* = 3, and *m/z* = 4 spectra of the MeOH/D/Au(111) experiment are simply added together, the composite spectra, depicted in Figure 2.3b and labeled "Masses 2+3+4," results. Slight differences in ionization probability and QMS sensitivity for H-H, H-D, and D-D do not allow this composite spectra to be analyzed quantitatively. However, the striking similarity between the "Masses 2+3+4" spectra in Figure 2.3b and the *m/z* = 2 spectra in Figure 2.3a give some qualitative evidence that "tail" feature in the MeOH/H/Au(111) system can be deconstructed into the phenomena behind the δ_1, δ_2, and δ_3 features in the MeOH/D/Au(111) system.

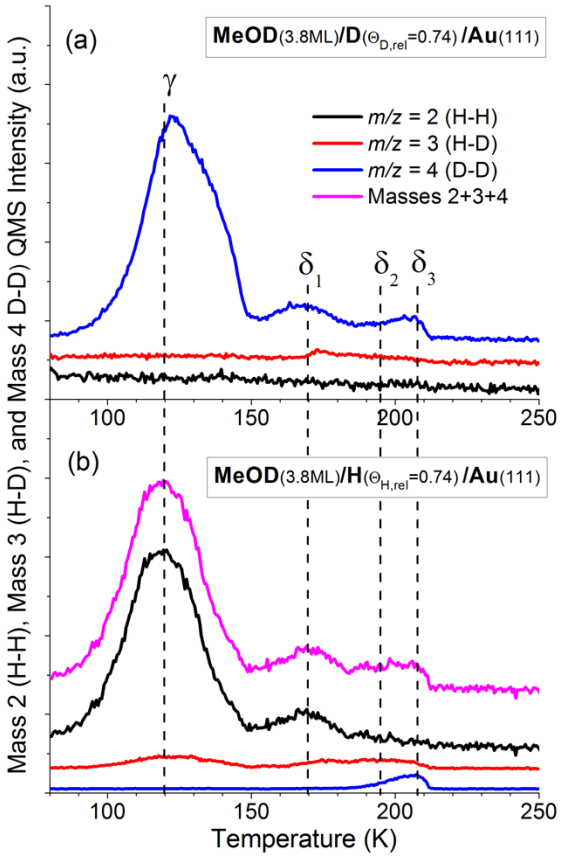

Figure 2.4: QMS spectra of *m/z* = 2, 3, and 4 for deuterated methanol (MeOD) coadsorbed with deuterium (D) or hydrogen (H). "Masses 2+3+4" is the composite spectra of adding the signals of *m/z* = 2, 3, and 4 together from 4b. a) 3.8 monolayers of MeOD coadsorbed with $\Theta_{D,rel}$ = 0.74 of deuterium; b) 3.8 monolayers of MeOD coadsorbed with $\Theta_{H,rel}$ = 0.74 of hydrogen. All species were adsorbed at 77 K. The heating rate was 1 K/s.

To further explore these phenomena, deuterated methanol (MeOD) was coadsorbed with hydrogen (H) and deuterium (D) separately on the Au(111) surface. Figure 2.4 depicts the *m/z* = 2, *m/z* = 3, and *m/z* = 4 spectra for the MeOD/D/Au(111) (Figure 2.4a) and MeOD/H/Au(111) (Figure 2.4b) systems. The MeOD/D/Au(111) system displays similar behavior to the MeOH/H/Au(111) system depicted in Figure 2.3a: the D-D (*m/z* = 4) desorption spectra displays a large γ desorption feature, centered

at 125 K, with a broad "tail" ranging from about 150 K to 210 K. Additionally, the H-H (*m/z* = 2) desorption feature is expectedly flat and the H-D (*m/z* = 3) desorption feature exhibits small desorption features, which is likely due to H impurities in the MeOD reactant and the gas handling plumbing.

Coadsorption of MeOD with H, shown in Figure 2.4b, shows a similar behavior to the MeOH/D/Au(111) system (Figure 2.3b). There is a large γ peak for H-H desorption, but the "tail" is again split into 3 distinct features: 1) a H-H desorption feature centered at 170 K, denoted as "δ_1," 2) a broad H-D desorption feature centered at 195 K, denoted as "δ_2," (this feature is more distinct under magnification; a magnified *m/z* = 3 spectra for a similar system can be seen in Figure 2.6a) and 3) a D-D desorption feature centered at 207 K, denoted as "δ_3," however these features appear less distinct in Figure 2.4 than in Figure 2.3. Similar to Figure 2.3b, the *m/z* = 2, *m/z* = 3, and *m/z* = 4 spectra from the MeOD/H/Au(111) spectra in Figure 2.4b have been simply added together to form a composite spectra, labeled "Masses 2+3+4" in Figure 2.4b. Again, while this composite spectra cannot be analyzed quantitatively, the similarity between this composite spectra and the *m/z* = 4 spectra in Figure 2.4a strongly suggests that the phenomena that result in the δ_1, δ_2, and δ_3 features are also responsible for the "tail" feature.

The similarities between the MeOH/D/Au(111) system (Figure 2.3b) and the MeOD/H/Au(111) system (Figure 2.4b) provides valuable insight into the hydrogen exchange phenomenon occurring on the surface. The stratification of the *m/z* = 2, *m/z* = 3, and *m/z* = 4 spectra can be attributed to the origin of the hydrogen atoms: whether they originated from the surface, denoted as H_s, or whether they originated from a methanol molecule, denoted as H_m. Consequently, the H/D desorption spectra of any combination of MeOH or MeOD with H or D can be broken down into 4 distinct features: 1) γ, H_s-H_s desorption indicated by the large peak at low temperature, 2) δ_1, the low temperature

region of the "tail" where H_s adatoms interact with methanol molecules but recombine with themselves (H_s-H_s), 3) δ_2, the medium-high temperature feature where a H_m, from hydrogen exchange, combines with a H_s to form a H_m-H_s molecule, and 4) δ_3, the high temperature feature of hydrogen atoms originating exclusively from the methanol hydrogen exchange combining with themselves (H_m-H_m).

Figures 2.3 and 2.4 clearly depict that the hydrogen products of the hydrogen exchange reaction desorb at higher temperatures than hydrogen adatoms originating from the surface. This suggests that the methanol/hydrogen surface structure(s) involved in hydrogen exchange also desorb at higher temperatures, since the "tails" for the hydrogen and methanol desorption spectra line up. The methanol species involved in this hydrogen exchange also appear to be "locked" into adsorbate structure(s) that desorb at higher temperatures. Figure 2.5 compares spectra for a MeOH/D/Au(111) system (black) with a MeOH/H/Au(111) system (red) to probe for MeOD, the methanol product of the hydrogen exchange reaction from the MeOH/D/Au(111) system.

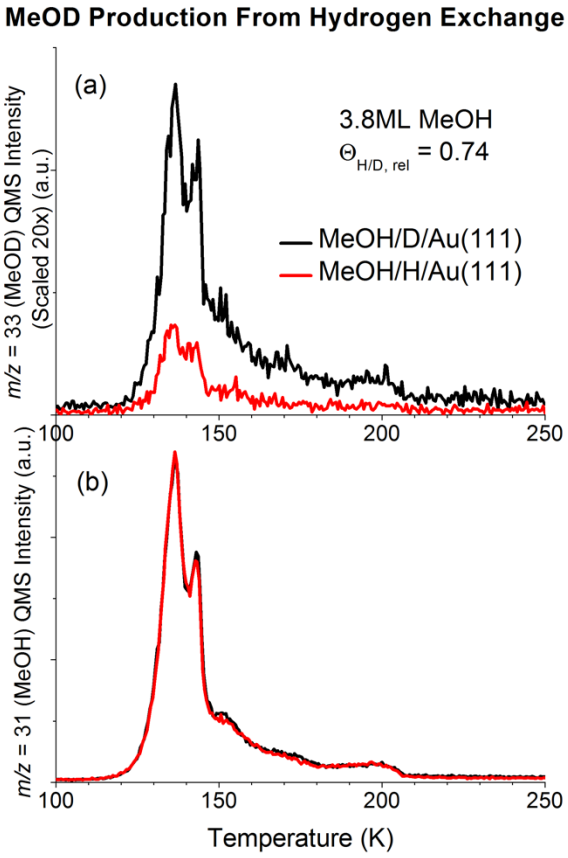

Figure 2.5: QMS spectra for 3.8ML MeOH coadsorbed with either $\Theta_{H,rel}$ = 0.74 of H (red) or $\Theta_{D,rel}$ = 0.74 of D (black). a) *m/z* = 33, scaled 20x relative to (b), indicative of MeOD. b) *m/z* = 31, indicative of MeOH, though MeOD makes a negligible contribution. All species were adsorbed at 77 K. The heating rate was 1 K/s.

Figure 2.5a displays the *m/z* = 33 spectra, indicative of MeOD, for these two systems. While the MeOH/H/Au(111) system does exhibit a signal, which can be attributed to natural isotopic abundance, the MeOH/D/Au(111) system exhibits a much larger feature, confirming that MeOD is, in fact, produced. The difference in the *m/z* = 33 integration area between the MeOH/D/Au(111) and MeOH/H/Au(111) systems indicate that approximately 0.2-0.3 monolayers of MeOD are produced via the hydrogen exchange reaction. The more interesting aspect of this spectra, however, is its similarity

to the *m/z* = 31 feature in Figure 2.5b, indicative of MeOH (although a MeOD mass fragment does make a negligible contribution). The similarity in shape between the *m/z* = 33 and the *m/z* = 31 features for the MeOH/D/Au(111) system indicate that the MeOD is well mixed into every layer and phase of the 3.8 monolayers of methanol on the surface. Experiments of MeOH coadsorbed with MeOD, shown in Supporting Information Figure A1 and A2, show that MeOH and MeOD will mix thoroughly on both clean Au(111) and H-precovered Au(111) at temperatures below the initial desorption temperature, ~120 K. Similarly, previous work[59,60] has shown that methanol and ethanol are able to thoroughly mix on a Pt(111) surface between 105 K and 110 K. This ability to mix is in contrast to the stratification of the hydrogen products noted earlier. Additionally, this observation also indicates that the hydrogen exchange occurs at temperatures lower than ~120 K, the initial onset of methanol desorption, suggesting that methanol is able to separate from the reaction structure while the exchanged hydrogen remains adsorbed.

A possible explanation for this phenomenon comes from previous work by Pan et al. who performed similar isotopic studies with water and hydrogen/deuterium on Au(111)[41] that exhibited similar behavior. Their DFT calculations show that it is energetically unfavorable for a single water molecule to bond to a hydrogen adatom to form H_3O on the surface, but it is energetically favorable for a water dimer or cluster to incorporate an extra hydrogen atom. Additionally, it is energetically favorable for a water molecule on the edge of a hydrogen-bonded water cluster to bind to a surface hydrogen adatom and break off from the cluster, leaving one of its original hydrogens on the cluster. They then speculate that the parts of the water clusters without an extra hydrogen atom desorb at lower temperatures, leaving only dimers and small clusters with an extra hydrogen to break apart, which desorb at the highest temperatures.

Since the H_2O/H/Au(111) system exhibits similar behavior to the MeOH/H/Au(111) system discussed in this report[41], and since methanol has been shown to create hydrogen-bonding networks on Au(111)[48], we can speculate that a similar mechanism could be responsible for the results reported here. Let us use the MeOH/D/Au(111) system to illustrate our proposed mechanism for this exchange reaction. A methanol molecule on the edge of a hydrogen-bonded network (dimer or larger cluster of methanol) on the Au(111) surface could bind to a surface deuterium adatom, D. This methanol molecule could then break off of the cluster, forming MeOD, leaving its original hydroxyl hydrogen, H, bound to the edge of this network. This MeOD molecule can now mix into the other layers (recall this observation from Figure 2.5) while the removed H stays bound to the cluster or dimer. As the temperature increases, the species largely uninvolved in the methanol-deuterium interactions (the multilayer methanol molecules (α_1 and α_2 features) and γ hydrogen molecules) desorb first. Then, coadsorbed methanol molecules and deuterium adatoms that were interacting with each other on the surface, but did not undergo hydrogen exchange, desorb, forming the δ_1 D-D feature, and methanol desorption at the same temperature. With increasing temperature, the dimers and small clusters containing an extra hydrogen atom start to desorb, releasing one of their H atoms. At the lower temperatures, these H atoms can combine with the few remaining D adatoms to create the H-D (δ_2) feature. But, at higher temperatures, only H atoms remain, creating the H-H (δ_3) feature.

2.3.3: The inhibiting effect of MeOH on MeOD hydrogen exchange

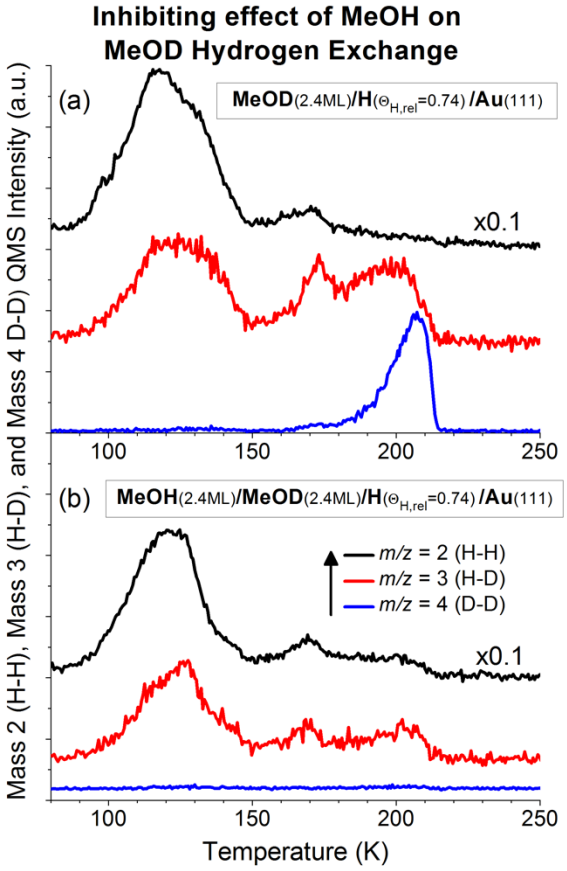

Figure 2.6: QMS spectra of *m/z* = 2, 3, and 4. a) $\Theta_{H,rel}$ = 0.74 of hydrogen, then 2.4ML deuterated methanol (MeOD) deposited on Au(111) b) $\Theta_{H,rel}$ = 0.74 of hydrogen, then 2.4ML deuterated methanol (MeOD), then 2.4ML methanol (MeOH) deposited on Au(111) surface. All species were adsorbed at 77 K. The heating rate was 1 K/s.

Figure 2.6a depicts the H-H (*m/z* = 2), H-D (*m/z* = 3), and D-D (*m/z* = 4) desorption spectra of 2.4 monolayers of MeOD coadsorbed with $\Theta_{H,rel}$ = 0.74 of hydrogen. The presence of distinct H-D and D-D features indicates that the MeOD/H/Au(111) system is clearly able to experience hydrogen exchange, as noted above. However, when 2.4ML MeOD and 2.4ML MeOH are coadsorbed (regardless of order) with $\Theta_{H,rel}$ = 0.74 of hydrogen, no D-D desorption features, and only small H-D

desorption features are present in the 150 K – 210 K temperature range, as seen in Figure 2.6b. It should be noted that the *m/z* = 3 feature centered at 130 K in Figure 2.6b is due to deuterium impurities in the gas handling plumbing, and is observed with the same intensity in corresponding MeOH/H/Au(111) experiments. These results suggest that the presence of MeOH inhibits the ability of MeOD to hydrogen exchange.

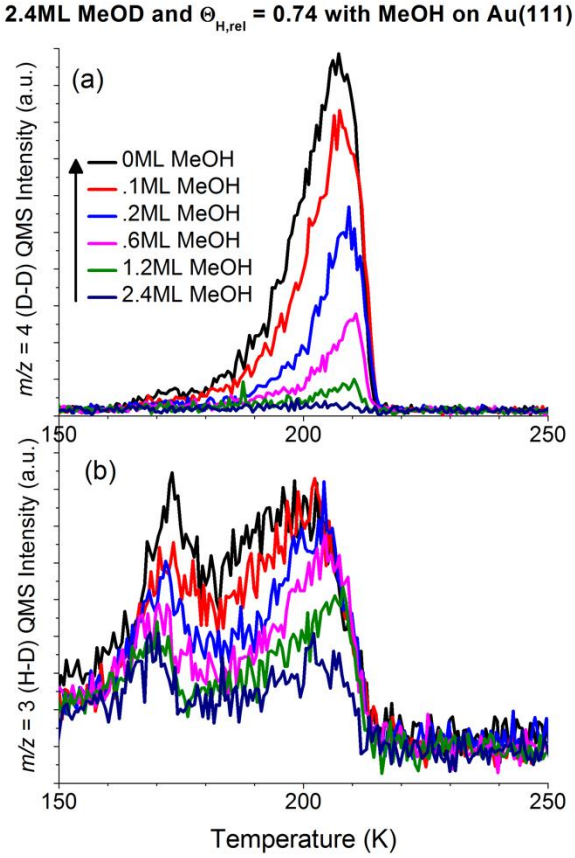

Figure 2.7: 2.4ML deuterated methanol (MeOD) coadsorbed with various amounts of MeOH on H-precovered ($\Theta_{H,rel}$ = 0.74) surface. MeOD:MeOH ratios given by legend. a) *m/z* = 4, indicative of D-D desorption b) *m/z* = 3, indicative of H-D desorption. All species were adsorbed at 77 K. The heating rate was 1 K/s.

To further explore this inhibiting effect, 2.4 monolayers of MeOD and $\Theta_{H,rel}$ = 0.74 of hydrogen were coadsorbed with various amounts of MeOH. Figure 2.7 depicts the

D-D (Figure 2.7a) and H-D (Figure 2.7b) desorption spectra for these experiments. The results show that MeOH significantly decreases the amount of MeOD hydrogen exchange products, even with a ~0.1ML of MeOH coverage (approximately 20:1 MeOD:MeOH ratio). A possible explanation for this behavior is that the number of possible hydrogen exchange reactions is limited and that MeOH and MeOD molecules are in competition for these limited possible reactions. Since the hydrogen exchange reaction involves breaking the O-H or O-D bond in methanol, and an O-H bond requires less energy to break than an O-D bond, due to zero-point energy differences, the MeOH would preferentially undergo hydrogen exchange compared to MeOD. Additionally, this phenomenon is consistent with the speculated mechanism proposed earlier that the hydrogen exchange reaction leaves a hydrogen on a methanol dimer or cluster. With this proposed mechanism, the number of possible reactions would be limited by the number of dimers and clusters in the monolayer that can incorporate an extra hydrogen atom. The MeOH molecules are preferentially able to hydrogen exchange and leave their H on the clusters and dimers at lower temperatures, leaving fewer clusters and dimers that can stably accept a D atom from a MeOD that readily undergoes a hydrogen exchange reaction at a higher temperature than the MeOH. That ~0.2-0.3 monolayers of MeOD is produced, as mentioned above, suggests that there is an average of approximately 3-5 methanol molecules in the monolayer for every extra hydrogen atom.

2.3.4: Similarities for Ethanol and Water

To explore whether this phenomenon is exclusive to methanol, similar experiments using ethanol were performed. Comparisons similar to those depicted in Figures 2.1-2.6, A1, and A2 are depicted in Figure A4-A11, respectively. Figure A4 depicts the H_2 and EtOH desorption spectra for 1.9 monolayers of ethanol coadsorbed

with various coverages of hydrogen, while Figure A5 depicts $\Theta_{H,rel} = 0.74$ of hydrogen coadsorbed with various coverages of ethanol. Both of these plots show the formation of the monolayer "tail" feature seen previously in the methanol experiments. The *m/z* = 2, *m/z* = 3, and *m/z* = 4 spectra for EtOH/H are compared to EtOH/D in Figure A6, and the spectra for EtOD/D are compared to EtOD/H in Figure A7. These plots also show stratified H-H, H-D, and D-D plots for EtOH/D and EtOD/H, similar to that seen in Figures 2.3 and 2.4, which can also be added together to create a composite spectra similar to the EtOH/H or EtOD/D spectra. Figure A8 shows that the deuterated ethanol product from the EtOH/D shows a similar ability to mix into multiple layers of ethanol on the surface, similar to that seen in Figure 2.5. Additionally, Figure A9 demonstrates the inhibiting effect EtOH has on the ability for EtOD to hydrogen exchange, similar to the phenomenon seen in Figure 2.6. Ethanol also has a similar ability to mix as methanol, as evidenced by mixing seen in EtOH/EtOD coadsorption on clean Au(111) and H-precovered Au(111), depicted in Figure A10 and A11, respectively. As noted above, this is also supported by previous work indicating that methanol and ethanol can thoroughly mix on a Pt(111) surface between 105 K and 110 K[59,60].

Thus, all of the phenomena observed with methanol on a H-precovered Au(111) surface are also observed with ethanol, indicating that these phenomena may be common to alcohols. Similar isotopic experiments using water have also been studied, as mentioned before. In addition to displaying an ability to hydrogen exchange, a similar stratification of hydrogen desorption based on the origin of the hydrogen (H_{water} vs. $H_{surface}$) was reported[41]. This may be an indication that this behavior is due to the O-H group, and may be common to species with the O-H functional group in general.

2.4: CONCLUSIONS

We have shown that the interaction of methanol and hydrogen coadsorbed on an Au(111) surface induces an adsorbate structure, or set of structures, with a wide range of desorption energies, producing a "tail" feature, indicating stronger bonding, in the TPD spectra of methanol and hydrogen. Coadsorption of methanol with hydrogen also induces a more strongly bound second layer, indicated by increased desorption temperature. This phenomenon is likely explained by increased hydrogen bonding interactions between the monolayer and the layer(s) above it, induced by the coadsorbed hydrogen adatoms.

Using isotope studies, we have shown that the hydrogen from the methanol O-H group is able to exchange with a hydrogen adatom from the surface. Additionally, the hydrogen desorption spectra indicates that hydrogens originating from methanol desorb at higher temperatures than hydrogens originally adsorbed to the gold surface. Meanwhile, the methanol products of hydrogen exchange are able to mix into every layer of methanol on the surface, suggesting that the hydrogen exchange reaction takes place at low temperature (<120 K). These results, combined with previous work with water, lead us to speculate on the mechanism for hydrogen exchange. Specifically, that methanol molecules on the edge of a cluster will bind to a hydrogen adatom, then break the O-H bond, leaving this hydrogen on the cluster. The sections of the clusters with an extra hydrogen atom require the most energy to break apart, and thus desorb at a higher temperature, releasing a hydrogen originating from methanol in the process.

Coadsorbing MeOD and MeOH on a H-precovered Au(111) shows that even small amounts of MeOH can inhibit the ability of MeOD to hydrogen exchange. This behavior suggests that MeOH and MeOD are in competition for a limited number of possible hydrogen exchange reactions, and that the weaker O-H bond in MeOH (compared to the O-D bond in MeOD) allows it to preferentially participate in these

hydrogen exchange reactions. This is consistent with the hypothesis proposed earlier, since the number of monolayer dimers and clusters that can stably accommodate an extra hydrogen atom limits the number of hydrogen exchange reactions.

The findings in this report provide insight into the interactions between O-H groups and hydrogen adatoms on the Au(111) surface. This work demonstrates that H-precovered Au(111) can dissociate an alcohol O-H bond, providing evidence that this is a feasible intermediate for organic reactions on a gold surface. Additionally, this work provides insight into the interactions of alcohols on a hydrogen-covered gold surface, complimenting previous work regarding methanol surface structure on a clean gold surface and providing insight for further understanding of hydrogenation reactions on gold, which could aid in the determination of reaction mechanisms involving alcohols, hydrogen, and/or gold and help direct further research toward the discovery of new reactions that occur over gold.

Chapter 3: Tunable Syn Gas Ratio via Bireforming Over Coke-Resistant Ni/Mo_2C Catalyst*

3.1: INTRODUCTION

Since Levy and Boudart demonstrated that tungsten carbide (WC) exhibited catalytic activity similar to Pt[61], metal carbide based catalysts have attracted a significant amount of attention due to their catalytic similarity to noble metal catalysts[62–65]. Along with WC, molybdenum carbide (Mo_2C) catalysts have been one of the primary carbides studied, particularly for reactions involving hydrocarbons[66–71]. After Green and coworkers demonstrated that WC and Mo_2C catalyzed methane reforming reactions with activities comparable to Ir and Ru[72–77], studies of methane and hydrocarbon reforming catalyzed by Mo_2C have become a popular vein of research[78–80].

Part of the interest in carbide based catalysts is due to their unusual mechanisms, especially for methane reforming reactions. While the actual catalytic mechanism(s) are still unclear, Mo_2C-based catalysts appear to balance competing oxidation and carburization reactions. This is supported by the fact that Mo_2C deactivates via oxidation to MoO_2[72,74,77,79,81–83], and that C^{13} labeling studies have demonstrated carbon exchange between Mo_2C and CH_4[76,82]. LaMont and Thomson [84] proposed the following as the possible competing carburization and oxidation reactions for Dry Methane Reforming (DMR):

$$Mo[]Mo + CH_4 \leftrightarrow Mo[C]Mo + 2H_2 \quad (1)$$

$$Mo[C]Mo + CO_2 \leftrightarrow Mo[C]Mo\cdots OCO \quad (2)$$

$$Mo[C]Mo\cdots OCO \leftrightarrow Mo[]Mo + 2CO \quad (3)$$

$$Mo[]Mo + CO_2 \leftrightarrow Mo[O]Mo + CO \quad (4)$$

*This work was previously published: A. Brush, E. J. Evans, G. M. Mullen, K. Jarvis and C. B. Mullins, *Fuel Process. Technol.*, 2016, **153**, 111–120. The author of this dissertation was responsible for developing and performing the reaction runs, and performing BET, XRD, TGA SEM, SEM-EDX, and GC/conversion analysis.

where the catalytic cycle is represented by reactions 1-3, with (3) being the rate determining step. The first step in the deactivation of the catalyst via oxidation to MoO_2 is represented by reaction 4, with the stability of the catalyst determined by the relative rate of (4) versus (1). A mechanism for Steam Methane Reforming (SMR) was not proposed, but likely also consists of competing carburization and oxidation reactions, since Mo_2C shows similar catalytic and deactivation behavior for the SMR reaction as the DMR reaction[81]. Additionally, Darujati, Lamont and Thomson demonstrated that H_2 and CO inhibited catalyst oxidation under methane reforming conditions and that a "carburizing ratio" (defined as: $R_s = \frac{P_{H2} + P_{CO}}{P_{CO2} + P_{H2O}}$) of 0.8 or higher stabilizes the Mo_2C catalyst at atmospheric conditions[81]. Lamont and Thomson later demonstrated that this ratio could be obtained by including H_2 or CO in the reactant stream, recycling the product stream, or operating under mass-transfer limited, high conversion conditions that give a high R_s at the catalyst surface[85].

One branch of this research has been to incorporate other metals that catalyze methane reforming into Mo_2C. In particular, the addition of Ni or Co to Mo_2C during catalyst synthesis has demonstrated an increased reactivity and stability compared to pure Mo_2C for methane reforming reactions[86–91]. Ni-based catalysts are the most commonly used in methane reforming reactions[3], where Ni is often responsible for the methane decomposition step[92]. It is likely that Ni performs a similar function in Ni/Mo_2C catalysts. This is supported by the findings of Shi et al[87] who found that Ni/Mo_2C with a Ni:Mo ratio of 1:2 showed high, stable activity for the DMR reaction. However, a lower Ni:Mo ratio of 1:3 oxidized to Ni/MoO_2 with deactivation, similar to Mo_2C catalysts, but a higher Ni:Mo ratio of 1:1 showed carbon formation, interpreted as coking, but no

oxidation to MoO_2, with deactivation, a mechanism more typical of Ni-based methane reforming catalysts[2,93,94].

These findings demonstrate the potential benefit of using Ni/Mo_2C as a catalyst for certain methane reforming applications. A major issue in Ni-based catalysts is preventing coking, which causes catalyst deactivation and the potentially dangerous phenomenon of "whiskering," where formation of carbon filaments can plug the reactor or destroy the catalyst[95–97]. This is particularly true for reactions run at high temperature, where coking becomes an even greater issue for Ni-based catalysts, and much work in finding coke-resistant catalysts has been done[98]. As a result, a majority of research on methane reforming over Ni/Mo_2C has focused on Dry Methane Reforming (Reaction 5)[86–88,99], which is notorious for causing coking in Ni-based catalysts. Partial Oxidation (Reaction 6)[100] and Water-Gas Shift (Reaction 7)[101] reactions have also been studied, but to a lesser degree, and, to our knowledge, Steam Methane Reforming (Reaction 8) has not been previously studied at all on Ni/Mo_2C.

Dry Methane Reforming: $CO_2 + CH_4 \rightarrow 2CO + 2H_2$ (5)

Partial Oxidation: $\frac{1}{2}O_2 + CH_4 \rightarrow CO + 2H_2$ (6)

Water-Gas Shift Reaction: $H_2O + CO \rightarrow H_2 + CO_2$ (7)

Steam Methane Reforming: $H_2O + CH_4 \rightarrow CO + 3H_2$ (8)

Dry Methane Reforming is attractive in situations where the methane feed is rich in CO_2, as can be the case with natural gas or biogas, or a cheap source of CO_2 is available, such as a waste CO_2 stream. One issue with Dry Methane Reforming is that the synthesis gas ("Syn Gas": H_2 + CO) ratio produced is 1:1 H_2:CO. However, one of the most common ratios of Syn Gas used in industry is ~2:1 H_2:CO, typically used in industry to make most hydrocarbons, such as methanol, via the Fischer-Tropsch reaction[2,94,102,103]. In order to achieve the desired H_2:CO ratio, steam can be added as a

reactant in order to simultaneously perform the dry reforming and steam reforming reaction, a process known as bireforming. However, bireforming is not as widely used due to the easy formation of carbon on the Ni-based catalysts at the high temperatures (up to 960°C) required for high conversion, as covered in a review by Mortensen and Dybkjaer[104]. One potential benefit of bireforming, however, is that the H_2:CO ratio can be adjusted based on the reactant mixture, allowing a range of Syn Gas ratios to be produced in one reactor. Since capital costs tend to be the most significant costs typically associated with a methane reforming process[3,4], finding a versatile methane reforming process that utilizes one reactor is highly desirable.

In this study, we demonstrate that Ni/Mo_2C can catalyze the dry methane reforming reaction, the steam methane reforming reaction, and bireforming reaction at 950°C. In addition, by varying the ratio of CO_2:H_2O that is used to reform CH_4, we can tune the resulting H_2:CO ratio of the Syn Gas product. Additionally, we document an unusual catalyst behavior in this reaction. All reactions exhibit high conversion for a certain period of time (100-300 minutes) followed by a rapid (less than 10 minutes) drop in conversion. During the period of high conversion, the catalyst exhibits no signs of coking, oxidation or other indications of any degree of deactivation. Yet, immediately after the sharp drop in conversion, the catalyst shows a significant degree of Mo_2C oxidation to MoO_2 as well as a noticeable change in the Ni phase. Further exposure to the reaction conditions after deactivation showed increases in the degree of oxidation of the catalyst as well as no rebound in catalytic activity. Most strikingly, we find no evidence of coking in this reaction, either when the catalyst is active or deactivated. This is especially significant considering that the reaction conditions used (high temperature of 950°C and excess CH_4) are favorable for coke formation on Ni-based catalysts[105].

3.2: EXPERIMENTAL

3.2.1: Catalyst Synthesis

The Ni/Mo_2C catalyst was synthesized in two distinct steps: synthesis of $NiMoO_4/MoO_3$, and carburization of $Ni/MoO_4/MoO_3$ to Ni/Mo_2C. $NiMoO_4/MoO_3$ was synthesized similar to the process described by Shi et al.[87]. $Ni(NO_3)_2 \cdot 6H_2O$ (Alfa Aesar, 99.9985%, metals basis) and $(NH_4)_6Mo_7O_{24} \cdot 4H_2O$ (Sigma Aldrich, 99.98%, metals basis) in quantities to make a molar ratio of 3:10 Ni:Mo were dissolved in 18MΩ Deionized (DI) H_2O. The solution was stirred and heated to 80°C for 4 hours, allowing ~80% of the H_2O to vaporize off in the process. The resulting slurry was then vacuum filtered, and the solid was dried at 120°C for 12 hours. The dried solid was then calcined in air by ramping to 550°C at 5°C/min, holding at 550°C for 4 hours, and letting cool overnight. The resulting solid, determined to be $NiMoO_4/MoO_3$, was then stored.

The catalysts were synthesized and subjected to reaction conditions by first loading 0.4g of the $NiMoO_4/MoO_3$ on top of acid-washed quartz wool in a vertical 7mm ID quartz tube reactor, heated by a furnace (Applied Test Systems Model 3210). Up to 4 gases, controlled by electronic mass flow controllers, could be flowed through the reactor simultaneously. Steam (H_2O) was introduced into the system by means of a syringe pump and heated tubing immediately upstream from the quartz tube reactor. The $NiMoO_4/MoO_3$ was carburized to Ni/Mo_2C in 10 standard cubic centimeters per minute (SCCM) of flowing CH_4 and 40 SCCM H_2 by ramping from 300°C to 700°C at 1°C/min, and then holding at 700°C for 2 hours. The synthesis was stopped by turning off the furnace and flowing 50 SCCM of pure nitrogen overnight.

3.2.2 Bireforming Reaction Runs

For reaction run samples, the catalyst was kept in the quartz tube reactor under nitrogen without exposure to atmosphere and the reaction was performed the day after the synthesis. The catalyst was heated to 950°C at 10°C/min while flowing 36 SCCM N_2. Once the reactor reached 950°C, a mixture of 48 SCCM CH_4, 36 SCCM N_2 and 36 SCCM combined H_2O and CO_2 (amounts of each varied based on experiment) was flowed to begin the reaction run. This corresponds to 120 SCCM total flow of reactants and inert, consisting of 40% CH_4, 30% N_2, and 30% combined H_2O and CO_2. A reaction run was stopped by halting flow of all species except nitrogen. The reactor's furnace was turned off, and 36 SCCM N_2 flowed through reactor while the system cooled. The samples were removed from the reactor the following day, and ground with a mortar and pestle before post-reaction characterization. Most carbide studies indicate a need to "passivate" samples in a low-oxygen environment prior to exposure to atmosphere to prevent "deep oxidation." However, duplicates of NiMo-AsSyn and NiMo-30/0-AtDeact were each performed, but given a passivation treatment of 14 hours of 100SCCM 0.5% O_2/99.5% Ar at room temperature prior to removal from the reactor. The post-reaction characterization results were identical to those made without the passivation step, indicating that, at least for this study, passivation was not necessary.

Conversion data during the reaction was determined via injection of a continuously replenished sample loop every 10 minutes into a HP 5890 gas chromatograph (GC) using a Carboxene 1000 packed GC column and a thermal conductivity detector (TCD). Standardization injections were performed before each reaction run by performing GC injections of a stream of CH_4, N_2, and CO_2 with flowrates the same as the reaction run for that day. N_2 was utilized as an internal standard, and a comparison of the CH_4:N_2 and CO_2:N_2 peak area ratios of each injection to that found in

the standardization injections was used to calculate CH_4 conversion (X_{CH4}) and CO_2 conversion (X_{CO2}), respectively. Calibration curves of H_2 and CO, in conjunction with the N_2 internal standard, were used to determine the effluent flowrates of H_2 and CO. The 95% confidence interval of each measurement was determined to be no more than ±1.1%, and this uncertainty was propagated through the calculations of conversion, H_2:CO ratios, and H_2 and CO yields. Although this is discussed in more detail in section 3.1, all reaction runs at some point exhibited a sharp drop in CH_4 conversion (typically from $X_{CH4} > 50\%$ to $X_{CH4} < 10\%$) between two consecutive GC injections, which was used to designate the point of catalyst deactivation. Carbon balances were performed for each data point using the equation:

$$\%\, Difference = \frac{(CH_{4,out}+CO_{2,out}+CO_{out})-(CH_{4,in}+CO_{2,in})}{(CH_{4,in}+CO_{2,in})}.$$

All data points fell within ±10%, and more than 80% of our data points fell within ±5%.

"Snapshots" of the catalyst at various timepoints in the reaction were taken so that catalyst characterization via X-Ray Diffraction (XRD), Thermogravimetric Analysis (TGA), and electron microscopy could provide insight into the catalyst before and after deactivation. Each sample was created by allowing the reaction run to progress to the timepoint desired, then stopping the reaction as described above. For the "as synthesized" ("AsSyn") timepoint sample, the catalyst was removed from the reactor the day after synthesis without any further heating or exposure to reaction conditions. The "heated to 950°C" ("950C") timepoint sample was heated to 950°C in 36 SCCM flowing N_2, then cooled overnight in 36 SCCM flowing N_2. The "mid-reaction" ("MidRxn") timepoint samples were exposed to reaction conditions for 100 minutes before the reaction run was stopped. The "at deactivation" ("AtDeact") timepoint samples were stopped 10 minutes after the first Gas Chromatography (GC) injection that showed signs of deactivation was taken. Similarly, the reaction runs for the "1 hour after deactivation" ("1hrDeact")

timepoint samples were stopped 1 hour after the first GC injection to show signs of deactivation.

The format for sample names throughout this manuscript is: "NiMo-" (or "Mo_2C-" for pure Mo_2C samples without Ni) %CO_2/%H_2O – Timepoint. For example, "NiMo-20/10-AtDeact" refers to Ni/Mo_2C subjected to 120 SCCM total flow of reactants, composed of 40% CH_4, 30% N_2, 20% CO_2, and 10% H_2O, until deactivation was detected from the GC and the reaction was stopped. "MidRxn" and "1hrDeact" timepoints were taken only for 3 conditions: 0% CO_2, 30% H_2O; 15% CO_2, 15% H_2O; and 30% CO_2, 0% H_2O. Mo_2C samples were handled identically to Ni/Mo_2C samples, except that commercial MoO_3 (Acros Organics, 99+%), was used as the oxide precursor due to the inability to form MoO_3 using the same process as was used to synthesize $NiMoO_4$/MoO_3. Due to lack of reactivity, the only Mo_2C samples are "Mo_2C-AsSyn" and "1hrDeact" for 3 conditions: 0% CO_2, 30% H_2O; 15% CO_2, 15% H_2O; and 30% CO_2, 0% H_2O. Table 1 summarizes the various samples with their reaction conditions and analytical results.

3.2.3 Catalyst Characterization

BET surface area analysis was performed using a Quantachrome Instruments NOVA 2000 high-speed surface area BET analyzer at a temperature of 77 K. The data was analyzed by Quantachrome Autosorb1 software, using multipoint BET analysis from P/P_0 0.1 to 0.3 and achieving a minimum correlation coefficient of 0.995 and a C value greater than 20. Due to the small sample sizes used in the reaction tests, surface area analysis could not be reported for the specific samples discussed in this study. However, a larger sample equivalent to "NiMo-950C" was created in a 2" tube furnace using the same flowing gases and temperature program as used to create the NiMo-950C sample.

20 SCCM CH_4 and 80 SCCM H_2 were flowed through the tube furnace while the temperature was ramped from 300°C to 700°C at 1°C/min, held at 700°C for 2 hours while the CH_4/H_2 mixture flowed, then allowed to cool overnight while 100 SCCM N_2 flowed. The next day, the sample was ramped from 25°C to 950°C at 10°C/min, then allowed to cool overnight, all while 100 SCCM N_2 flowed through the tube furnace. The sample was removed the following day and not subjected to grinding with a mortar and pestle before BET analysis in order to more closely measure the surface area seen by the reaction.

XRD analysis was performed using a Bruker D8, using a KFL Cu 2K X-ray source operated at 40kV and 40mA and utilizing a Lynx Eye detector. Quantitative Rietveld analysis was performed with TOPAZ 4.2 software, and used a refined MoO_2 structure (spacegroup: P121/c1; lattice parameters: *a:* 5.5397198 Å, *b:* 4.8527199 Å, *c:* 5.6234565 Å, *β:* 119.6132°) and a refined Mo_2C structure (spacegroup: pbcn; lattice parameters: *a:* 4.7346397 Å, *b:* 6.0146343 Å, *c:* 5.2192023 Å). Ni phase was not included in fit. All analysis obtained a goodness of fit (*G*) of 2 or less.

A field emission JEOL 2010F high resolution transmission electron microscope (HRTEM) operated at 200 kV was used to obtain TEM and high angle annular dark field-scanning transmission electron microscopy (HAADF-STEM) images and conduct analysis on the nanometer scale. The TEM is equipped with an Oxford energy dispersive spectroscopy (EDS) instrument with a SiLi detector for elemental analysis. The transmission electron microscopy (TEM) grids were prepared by sonicating a small amount of catalyst sample in toluene. A few drops of the suspended catalyst were placed on lacey carbon coated copper grids. The TEM grid was then placed in a vacuum oven and heated to 100 °C overnight to remove excess solvent.

Thermo-gravimetric analysis was performed using a Mettler TGA/DSC 1. Air was used as the ambient gas, and the sample was ramped from 25°C to 1000°C at 10°C/min.

SEM and EDS analysis were performed on a JOEL JSM-6490LV SEM in high vacuum mode, unless otherwise noted. For stand-alone SEM images, the sample was coated with gold to improve sample conductivity for higher magnification imaging. All SEM images were taken using the SEI detector, 20kV accelerating voltage, 15mm working distance, and 30nm spot size. No coating was used when performing EDS analysis. All EDS analysis was taken using 20kV accelerating voltage, 11mm working distance, and 50nm spot size. 64 scans were averaged together for the EDS maps of Mo, Ni, C, and O.

It should be noted that these analytical techniques were performed on most samples, leading to a significant amount of data to report. In the main text of this manuscript, a representative set of conditions are presented for each analytical technique, and similar figures for the remaining conditions are reported in the Supplemental Information. In most cases, the data reported in the Supplemental Information follows the same trends as the representative data reported in the main body of the manuscript, and any differences are noted.

3.3: Results and Discussion

Below is a table of all samples referenced in this manuscript along with select analytical results for easy comparison. For this table, it should be noted that all average H_2:CO ratios have a maximum 95% confidence interval of ±2% (±0.08). Values for TGA and XRD analysis are reported to illustrate trends across timepoints, and are not necessarily meant to represent absolute, quantitative values.

Identifiers		Oxidant Mix		Reaction Run Results			TGA	XRD Phases	
Sample Name	**Timepoint**	**%CO_2**	**%H_2O**	**Deactivation Time (min)**	**Total Run Time (min)**	**Average H_2:CO***	**Max Wt %**	**%Mo_2C**	**%MoO_2**
NiMo-AsSyn	As Synthesized	N/A	N/A	N/A	N/A	N/A	129%	100%	0%
NiMo-950C	Heated to 950C	N/A	N/A	N/A	N/A	N/A	130%	100%	0.%
NiMo-0/30-MidRxn	100 min Reaction	0	30	N/A	100	2.9(8)	132%	93%	7%
NiMo-15/15-MidRxn	100 min Reaction	15	15	N/A	100	1.5(7)	137%	99%	1%
NiMo-30/0-MidRxn	100 min Reaction	30	0	N/A	103	0.9(5)	136%	100%	0%
NiMo-0/30-AtDeact	At Deactivation	0	30	110	118	3.0(0)	124%	31%	69%
NiMo-5/25-AtDeact	At Deactivation	5	25	190	200	2.3(8)	129%	55%	45%
NiMo-10/20-AtDeact	At Deactivation	10	20	100	110	1.8(9)	126%	45%	55%
NiMo-15/15-AtDeact	At Deactivation	15	15	230	243	1.5(7)	127%	48%	52%
NiMo-20/10-AtDeact	At Deactivation	20	10	220	230	1.3(0)	127%	46%	54%
NiMo-25/5-AtDeact	At Deactivation	25	5	290	300	1.1(1)	128%	53%	47%
NiMo-30/0-AtDeact	At Deactivation	30	0	190	198	0.9(1)	126%	48%	52%
NiMo-0/30-1hrDeact	1hr Deactivated	0	30	100	160	3.0(0)	122%	28%	72%
NiMo-15/15-1hrDeact	1hr Deactivated	15	15	360	440	1.6(7)	120%	23%	77%
NiMo-30/0-1hrDeact	1hr Deactivated	30	0	270	330	0.9(6)	122%	28%	72%
Mo2C-AsSyn	As Synthesized	N/A	N/A	N/A	N/A	N/A	131%	100%	0%
Mo2C-0/30-1hrDeact	1hr Deactivated	0	30	0	60	N/A	119%	20%	80%
Mo2C-15/15-1hrDeact	1hr Deactivated	15	15	0	60	N/A	126%	51%	49%
Mo2C-30/0-1hrDeact	1hr Deactivated	30	0	0	60	N/A	122%	35%	65%

Table 3.1: Ni/Mo_2C and Mo_2C samples with their respective oxidant mixtures, time to deactivation, total time exposed to reaction conditions, average H_2:CO ratio during period of high conversion, maximum weight % during Air-TGA, and %Mo_2C and MoO_2 as determined by Quantitative Rietveld Analysis of XRD spectra.

3.3.1: Bireforming Reaction Runs

Figure 3.1 depicts the CH_4 conversion, X_{CH4}, (Figure 3.1a), CO_2 conversion, X_{CO2}, (Figure 3.1b) and H_2:CO ratio (Figure 3.1c) versus reaction time for the various ratios of CO_2:H_2O oxidants. H_2O conversion could not be reported, as we could not effectively measure H_2O in the product stream with our setup. All conditions exhibit a similar reaction progression: each run reaches $X_{CH4} > 70\%$ and $X_{CO2} \approx 100\%$ within the first 30 minutes of reaction, close to the maximum possible CH_4 and CO_2 conversions of 75% and 100%, respectively, due to excess CH_4. All runs then show a gradual decrease in X_{CH4} and X_{CO2} to no less than 45% and 65%, respectively, until exhibiting a rapid decrease in X_{CH4} and X_{CO2} to <10% and < 20%, respectively, within 10-20 minutes. This sudden decrease in conversion is considered to be an indication of the catalyst deactivation point. Designating this phenomenon as the point of deactivation is supported by the fact that no signs of reaction recovery were seen in the hour after deactivation for our "1hrDeact" samples.

As can be seen in Figure 3.1, the time required for the catalyst to deactivate ranged from 100 to 300 minutes, and does not seem to follow any discernable pattern with respect to CO_2:H_2O ratios. Several replicates of some conditions were performed and we found that no set of conditions had a consistent time required for catalyst deactivation. In fact, each condition showed a range of times between 100 and 300 minutes, similar to the range seen between the conditions seen in Figure 3.1. This suggests that the time to catalyst deactivation is likely due to some other phenomenon or catalyst property, and may not be affected significantly by the H_2O:CO_2 ratio.

Figure 3.1c demonstrates that the average H_2:CO ratio for pure steam reforming (0% CO_2, 30% H_2O; black curve) is 3.0 while the catalyst is active, exactly as expected for steam reforming. The pure dry reforming (30% CO_2, 0% H_2O; purple curve) results in

a H_2:CO ratio of 0.91 while the catalyst is active, slightly less than the expected value of 1.0 for dry reforming. For reaction conditions containing a mixture of H_2O and CO_2, the subsequent H_2:CO ratios decrease from 2.38 to 1.11 as less H_2O and more CO_2 is used in the oxidant mixture, as can be seen in Table 1. In fact, the H_2:CO ratios for all conditions are close (<0.12 difference) to the values expected, assuming complete conversion of H_2O and CO_2. However, the H_2:CO ratios are all slightly less than expected. This is likely due to the Water Gas Shift Reaction (WGSR, $H_2O + CO \rightarrow H_2 + CO_2$), which has a K_{eq} of 0.68 at 950°C[106], favoring H_2O + CO, but could also indicate some degree of oxidation of carbon in the catalyst to produce CO.

The absolute molar yields of H_2 and CO per mole of CH_4 consumed were calculated and are plotted in Figures B1a and B1b, respectively. The values for each run closely match what would be expected from each set of conditions, indicating that the methane reforming reactions are the dominant reactions in this system. Additionally, after deactivation, increases in H_2 molar yield and decreases in CO molar yield are seen with H_2O rich conditions, while the opposite (decreases in H_2 molar yields and increases in CO molar yields) is seen with CO_2 rich conditions. This phenomenon is mirrored in the H_2:CO ratio, plotted in Figure 3.1c, where the H_2:CO ratio increases in H_2O-rich conditions and decreases in CO_2-rich conditions after catalyst deactivation. This is consistent with contributions from the Water Gas Shift Reaction due to an increase in H_2O and/or CO_2 with deactivation. However, it is likely that the oxidants also oxidize the catalyst after deactivation, as indicated by increases in both H_2 and CO yield in the first data point after deactivation for many of the conditions.

Using BET surface area analysis, Ni/Mo_2C heated to 950°C was determined to have a specific surface area of 5.9 m^2/g. This is less than the 9 – 35 m^2/g range seen in other Ni/Mo_2C catalysts reported by Shi et al.[87] and Cheng and Huang[86]. Based on the

reactant flowrates, Ni/Mo_2C catalyst mass of 0.3g, and a methane conversion of 50%-75% while active, the areal reaction rate of this system is calculated to be 2.3×10^{-5} – 3.5×10^{-5} (moles CH_4 reacted)$m^{-2}sec^{-1}$. However, since the active sites of the catalyst are unknown in this system, it is difficult to compare to more traditional catalysts, where activity is most commonly described in terms of turnover frequency (TOF).

Samples of Mo_2C without Ni were also subjected to the three major reaction conditions (0% CO_2/30% H_2O, 15% CO_2/15% H_2O, and 30% CO_2/0% H_2O), and the CH_4 conversion data is shown in Figure B2. As can be seen in Figure B2, all of the Mo_2C catalysts show very little activity for methane reforming (<5% X_{CH4}), especially when compared to the corresponding Ni/Mo_2C catalysts. The steam reforming run appeared to show higher initial activity (as high as 25% X_{CH4}), but that may be caused by experimental error due to excess H_2O that can occur at the beginning of a reaction run from priming the syringe pump and heated steam lines. All reaction runs were allowed to run for 1 hour to confirm the persistently low activity.

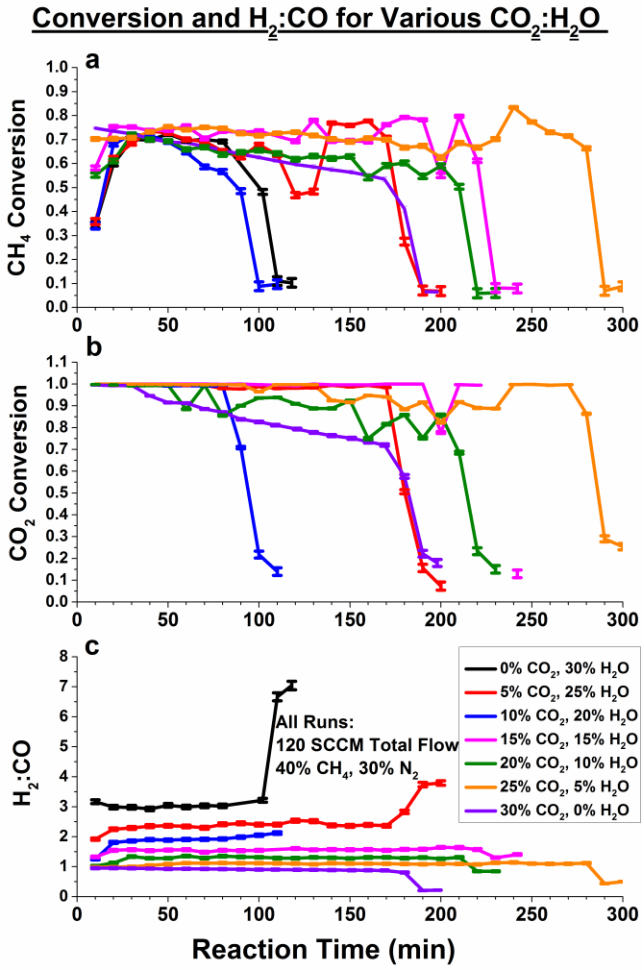

Figure 3.1: CH_4 Conversion (a), CO_2 Conversion (b), and H_2:CO production ratio (c) for various amounts of CO_2 and H_2O oxidants. Error bars represent the 95% confidence interval for each measurement.

3.3.2 XRD Analysis

Figure 3.2 depicts the XRD spectra for the Ni/Mo_2C catalyst at different timepoints during a representative dry reforming reaction run (40% CH_4, 30% N_2, 30% CO_2 and 0% H_2O). From bottom to top in Figure 3.2, the spectra represent: 1) NiMo-AsSyn; 2) NiMo-950C; 3) NiMo-30/0-MidRxn; 4) NiMo-30/0-AtDeact; and 5) NiMo-30/0-1hrDeact. Similar progressions are shown for pure steam reforming (0% CO_2, 30% H_2O) and 50/50 dry/steam reforming (15% CO_2, 15% H_2O) in Figures B3 and B4,

respectively, and follow the same trends as Figure 3.2. XRD of the catalyst oxide precursor confirming it to be composed of $NiMoO_4/MoO_3$ can be found in Figure B5.

Carburization of the $NiMoO_4/MoO_3$ precursor causes the MoO_3 phase to carburize to Mo_2C, as seen in Figure 3.2. However, after carburization, the Ni is no longer in a $NiMoO_4$ phase. Instead, the Ni appears to be part of a Ni^0-rich phase with some Mo incorporated into it, as will be discussed in more detail below. With heating to 950°C, the Ni-rich phase and Mo_2C phases both stay chemically unchanged, but appear to sinter into larger crystallites, indicated by the sharper XRD peaks compared to "NiMo-AsSyn". Quantitative Rietveld analysis suggests the crystallite size increases from ~40nm to ~150nm with heating to 950°C. 100 minutes into the dry reforming reaction run, the Ni-rich phase and the Mo_2C phase are both still present and unchanged compared to "NiMo-950C". Most surprisingly, though, is a lack of peaks corresponding to MoO_2 or graphite, which would indicate deactivation due to oxidation or coking, respectively. However, the catalyst immediately after deactivation shows clear peaks corresponding to MoO_2. Running reaction conditions for 1 hour after deactivation results in more oxidation, as seen by the increase in the main MoO_2 peak at $2\theta=26.0°$ relative to the main Mo_2C peak at $2\theta=39.3°$ compared to the spectra for "NiMo-30/0-AtDeact". Figure B6, which displays the XRD spectra for the Ni/Mo_2C catalyst "at deactivation" for the remaining oxidant mixtures, demonstrates that this behavior is common to all tested mixtures of CO_2 and H_2O. It is unclear, however, if the oxidation of the catalyst itself is responsible for catalyst deactivation or is merely a byproduct of exposure to a more oxidizing reactant stream once deactivation occurs.

XRD spectra of the Mo_2C catalysts are shown in Figure B7. Similar to "Ni/Mo_2C-AsSyn", "Mo_2C-AsSyn" showed broad Mo_2C features, indicative of small crystallite size (on the order of ~20nm, according to Quantitative Rietveld Analysis), but no MoO_2

features. All three of the deactivated catalysts exhibited peaks for both Mo_2C and MoO_2. In addition, the Mo_2C peaks in the deactivated catalysts were sharper than for "Mo_2C-AsSyn", indicating sintering of Mo_2C into larger crystallites during heating to 950°C in N_2 and one hour of reaction conditions.

Quantitative Rietveld analysis was performed on the XRD spectra for every sample, and the normalized $\%MoO_2$ and $\%Mo_2C$ are reported in Table 1. The Rietveld analysis confirms what a qualitative inspection of the XRD spectra suggests: the $\%MoO_2$ relative to $\%Mo_2C$ increases with prolonged exposure to the reaction conditions after deactivation. The lack of a MoO_2 feature through the reaction, the sudden appearance of MoO_2 at deactivation, and the growth of the MoO_2 feature with continued exposure to reaction conditions after deactivation show definitively that the onset of oxidation occurs at deactivation and the catalyst continues to oxidize after deactivation. The fact that MoO_2 accounts for ~50% of the catalyst immediately after deactivation for all reaction conditions indicates a high degree of oxidation within a short span, mirroring the rapid decline in conversion.

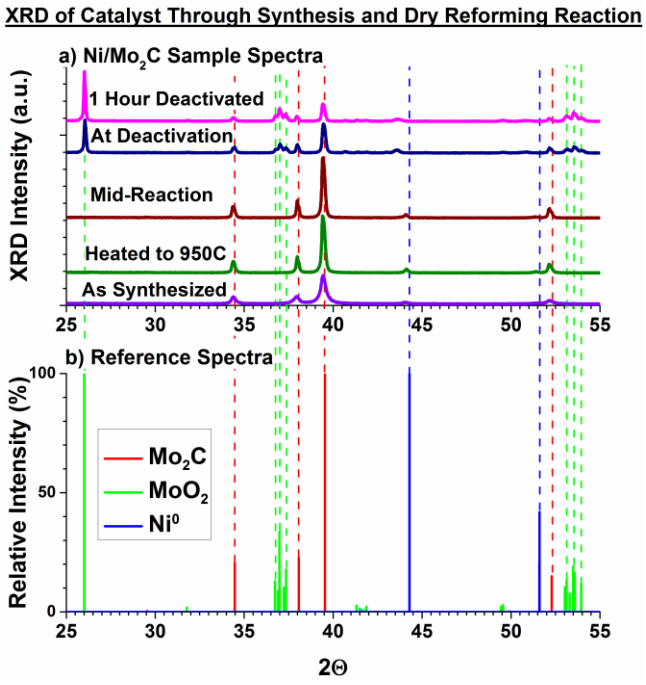

Figure 3.2: a) XRD of catalyst at various timepoints during synthesis and dry reforming reaction; b) Reference spectra with dashed lines extending into 2a for ease of phase identification.

The Nickel-containing phase also undergoes a transformation during synthesis and after deactivation, as can be seen in Figure 3.3, a close-up of the Ni-region in XRD for the dry reforming reaction progression spectra shown in Figure 3.2. Similar close-ups for the steam reforming reaction, 50/50 dry/steam reaction, and all of the "at deactivation" samples can be seen in Figures B8, B9, and B10, respectively. As discussed above, and seen in Figure B5, the Ni in the catalyst precursor seems to be present as part of a $NiMoO_4$ phase. After synthesis and through the first 100 minutes of the reaction, peaks appear in the XRD pattern at $2\theta=44.2°$ and $2\theta=51.4°$, in between the expected positions for Ni^0 and $Mo_{0.09}Ni_{0.91}$. Since Mo can incorporate into the Ni phase up to ~10% Mo[107], this Ni-rich phase is likely pure Ni^0 with up to 9% Mo incorporated into it.

After deactivation, however, the Ni-rich peaks shift lower, to 2θ=43.0°, 2θ=43.6° and 2θ=50.8°. The features at 2θ=43.0° and 2θ=43.6° appear to be at least two distinct peaks, which can be seen more clearly in Figure B10. The most likely match to these peaks is a mixture of NiO, which has a major peak at 2θ=43.1°, $MoNi_4$, which has a major peak at ~43.5° and minor peaks at 2θ=50.4° (larger) and 51.2° (smaller), and $Mo_{1.08}Ni_{2.92}$, which has a major peak at 43.0° and a minor peak at 50.1°. However, none of the minor peaks of the $MoNi_x$ phases line up well with the small, broad peak at 50.8°. The one other major peak for NiO, at 2θ=37.1°, would be obscured by MoO_2 features at the same angle, and cannot be seen. In addition, a peak at 2θ=40.6° in the deactivated catalyst is consistent with Mo^0, possibly formed during the oxidation of Mo_2C to MoO_2 or the oxidation of $Mo_{0.09}Ni_{0.91}$ to NiO. The slight shift to higher 2θ relative to the reference spectra may be indicative of some Ni incorporation into the Mo phase. Overall, these results suggest that, during catalyst deactivation, some of the Ni is oxidized, while other Ni regions incorporated more Mo, and some Ni possibly incorporated into a Mo phase created during deactivation. Interestingly, the Mo_2C samples do not have the same Mo^0 feature in their spectra, indicating that the presence of Ni may be involved in the formation of the Mo^0 phase during deactivation. Similar to the oxidation of Mo_2C to MoO_2, it is unclear whether the changes in the Ni phase are responsible for catalyst deactivation, or merely a byproduct of exposure to a more oxidizing reactant stream after catalyst deactivation.

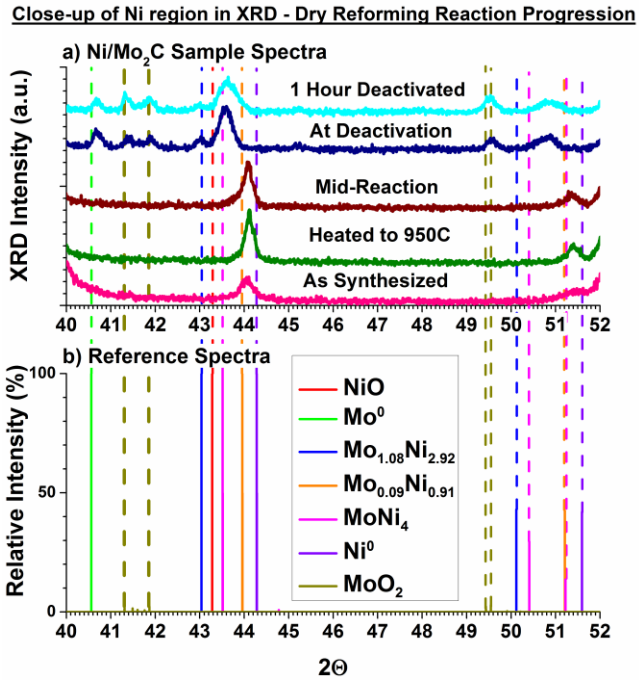

Figure 3.3: a) Close-up of Ni-region in XRD of catalyst at various timepoints during synthesis and dry reforming reaction; b) Reference spectra with dashed lines extending into 3a for ease of phase identification.

3.3.3: TEM

Figure 3.4 displays high magnification TEM images of the Ni/Mo_2C at four points in the mixed methane reforming reaction process: immediately after synthesis (4a), 100 minutes into the reaction ("mid-reaction"; 4b), at deactivation (4c), and 1 hour after deactivation (4d). Graphitic layers of carbon surrounding the bulk material can be seen for the as-synthesized and mid-reaction catalyst sample (Figure 3.4a and 3.4b). The spacing between the graphitic layers was measured to be 3.4Å using the Gatan Digital Micrograph program, which is consistent with the distance between the planes of graphitic layers. However, once the catalyst deactivates, these carbon layers are no longer found, as shown in Figures 3.4c and 3.4d. This suggests that the catalyst does not coke with deactivation, but rather excess carbon in the catalyst is actually consumed during

this reaction, despite operating at conditions that would normally cause coking in Ni-based catalysts.

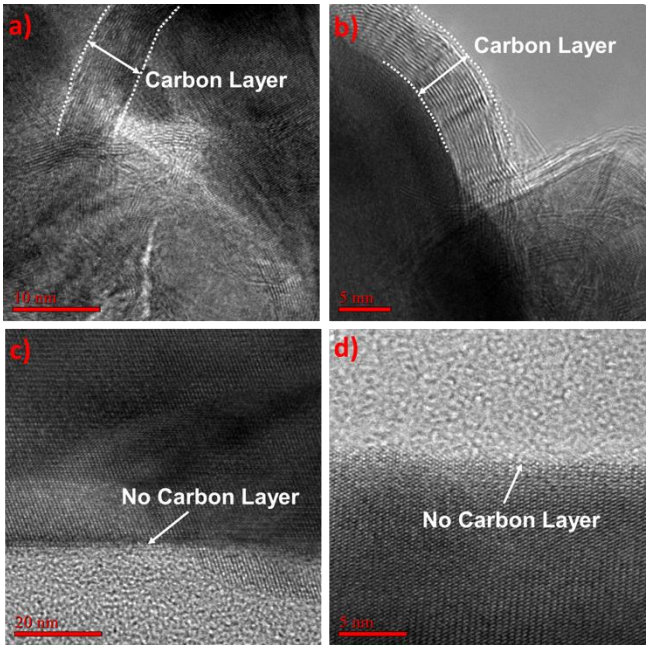

Figure 3.4: HRTEM images showing the disappearance of the graphitic layers on Ni/Mo_2C particles over the course of the 50/50 Dry/Steam reforming reaction: a) NiMo-AsSyn, b) NiMo-15/15-MidRxn, c) NiMo-15/15-AtDeact, d) NiMo-15/15-1hrDeact.

Figure 3.5 displays an HAADF-STEM image of the lacey carbon support of the "NiMo-15/15-AtDeact" sample. Small nanoparticles 1-10nm in size can be seen on the carbon support film as bright white dots, indicating the particles are composed of elements with high atomic mass. An image of these small particles alongside of a larger particle can be seen in Figure B11. This phenomenon is seen with the "at deactivation" and "1 hour deactivated" catalyst samples but is not present in the "as-synthesized" and "mid-reaction" catalyst samples. When conducting EDS on the carbon film of the TEM grid (Figure B12), we see very little to no molybdenum or nickel signal at their major

characteristic energies of 2.3 keV and 7.4 keV, respectively, for the as-synthesized and mid-reaction samples (Figures B12a and B12b). However, molybdenum and nickel peaks are readily seen on the carbon support film in the at-deactivation (Figure B12c) and 1 hour deactivated (Figure B12d) samples. This suggests that the shedding of these small nanoparticles likely coincides with catalyst deactivation and are rich in nickel and molybdenum.

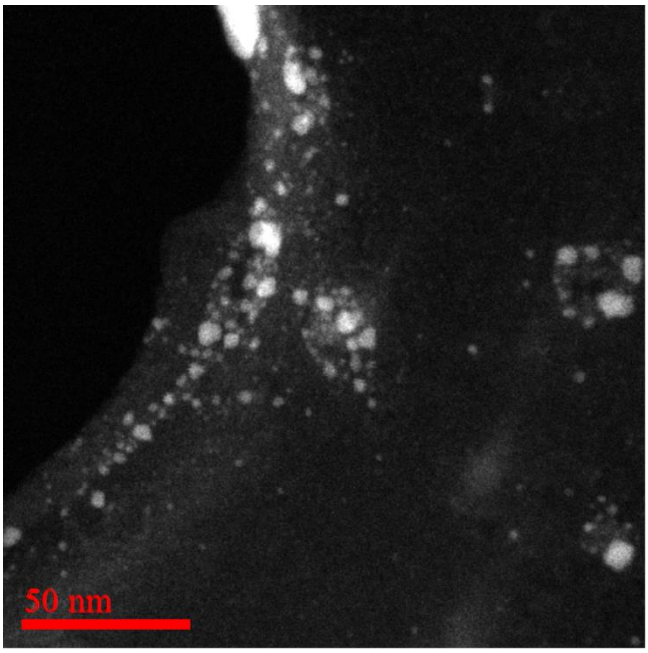

Figure 3.5: HAADF-STEM of NiMo-15/15-AtDeact. The small particles ranging from 1 to 10nm in size observed on the TEM grid carbon film appear as white dots. EDS indicates that they are likely composed of Ni and Mo.

3.3.4 TGA Analysis

Figure 3.6 shows the weight % (Figure 3.6a) and mass-normalized heat flow (Figure 3.6b) versus temperature for the Air-TGA analysis of the Ni/Mo_2C catalyst at various timepoints in the pure dry reforming (30% CO_2, 0% H_2O) reaction. Similar Air-TGA plots of the Ni/Mo_2C catalyst for pure steam reforming (0% CO_2, 30% H_2O) and

the 15% CO_2/15% H_2O condition, are shown in Figures B13 and B14, respectively. Air-TGA plots of the Ni/Mo_2C catalyst "at deactivation" for the remaining reaction conditions (5/25, 10/20, 20/10, and 25/5 of CO_2/H_2O) are shown in Figure B15. All conditions show similar behavior to the Air-TGA plots about to be discussed. Additionally, Air-TGA plots of commercial MoO_3, commercial Mo_2C, synthesized Mo_2C, and synthesized Mo_2C subjected to 1 hour of 15% CO_2/15% H_2O reaction conditions are shown in Figure B16 for comparison to the Ni/Mo_2C samples.

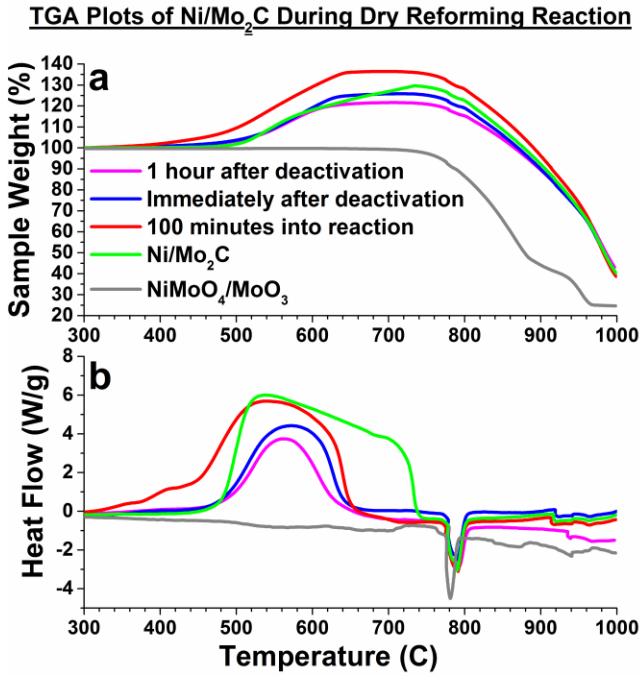

Figure 3.6: Air-TGA plots of sample weight percent (a) and heat flow (b) for Ni/Mo_2C at various timepoints during the dry reforming reaction.

In Figure 3.6, the plot of $NiMoO_4/MoO_3$ (gray) shows no change in weight % until ~790°C, where there is also a large negative spike in heat flow, as seen in Figure 3.6b. The negative spike in heat flow at 790°C, indicative of an endothermic process, is most likely the transition of a MoO_3 solid phase to the liquid phase.[108] The decline in

weight % above 790°C for MoO_3 is most likely due to the subsequent greater incorporation of oxygen to the point that the Mo/O system can exist in the gas phase and is slowly evaporated off.[108] These interpretations are further confirmed by the fact that pure MoO_3 exhibits the same behavior, as can be seen in Figure B16. However, in the case of pure MoO_3, the weight % eventually reaches zero by 980°C, while the $NiMoO_4/MoO_3$ decreased to only ~24% by 1000°C. This indicates that some or all of the Ni phase(s) in the $NiMoO_4/MoO_3$ sample do not evaporate off.

The Ni/Mo_2C samples from different reaction timepoints all exhibit a common behavior: no change in weight % until ~400-500°C, when each sample increases in weight % to some maximum weight %, then followed by a decline in weight % starting at ~790°C and continuing until the end of the analysis at 1000°C. The increase in weight % for each sample coincides with a large positive amount of heat flow, indicative of an exothermic process. This suggests that the Mo_2C in the Ni/Mo_2C samples is oxidizing to MoO_3 in the region. This assertion is supported by a few pieces of evidence. First, this same behavior is characteristic of pure Mo_2C samples, as can be seen in Figure B16. Second, the maximum weight % of commercial Mo_2C is 140%, almost exactly the theoretical increase in weight % of 141% expected by the Mo_2C to MoO_3 transformation. Finally, both the Mo_2C and Ni/Mo_2C samples exhibit the same endothermic spike at 790°C and decline in weight % starting at 790°C as seen in the MoO_3 and $NiMoO_4/MoO_3$ samples.

A closer inspection of the maximum weight % of the Ni/Mo_2C samples provides an insight into the catalyst at different timepoints in the reaction. The maximum weight percent measured for “NiMo-AsSyn,” “NiMo-30/0-MidRxn,” “NiMo-30/0-AtDeact,” and “NiMo-30/0-1hrDeact” samples are 130%, 136%, 126% and 121%, respectively. This trend is consistent across conditions, as can be seen in Table 1: The “MidRxn”

samples have the highest maximum weight %, followed by the "AsSyn" and "950C" samples, the "AtDeact" samples, and finally the "1hrDeact" samples.

The theoretical maximum weight % for pure Ni/Mo_2C samples, assuming complete oxidation to Ni/MoO_3, is 135%. There are two likely explanations for a sample that attains a maximum weight % less than 135%. First, there could be interstitial carbon that contributes mass initially, but is combusted to gaseous CO_2 during TGA. Since none of the curves exhibit a weight % less than 100% below 800°C, this combustion likely occurs at the same time as Mo_2C oxidation (400°C – 750°C). This is likely the case for NiMo-AsSyn, since HRTEM clearly shows a carbon layer in the as-synthesized catalyst (Figure 3.4), and no oxide features are seen in the XRD. Additionally, NiMo-AsSyn exhibits the largest amount of exothermic heat released of all the samples, which would be consistent with some combustion.

The second explanation for a maximum weight % less than 135% would be that some of the Mo_2C has oxidized to MoO_2, since oxidation from MoO_2 to MoO_3 results in less weight gain than oxidation from Mo_2C to MoO_3. This is likely the case for the "AtDeact" and "1hrDeact" samples. This is supported by the clear presence of MoO_2 in the XRD spectra for the samples at these two timepoints. In addition, "1hrDeact" samples show smaller maximum weight % values than the "AtDeact" samples, consistent with a greater degree of MoO_2 compared to Mo_2C, as suggested by the Quantitative Rietveld XRD Analysis trends. The "1hrDeact" samples have the lowest amount of exothermic heat released, and the "AtDeact" samples have the second-to-lowest amount of exothermic heat released, consistent with partially oxidized samples instead of samples with excess carbon.

The maximum weight % of the "MidRxn" samples are all very close the theoretical maximum of 135%. These results suggest that the carbon layers seen in

HRTEM images of the catalyst mid-reaction are likely not as prevalent as the carbon layers seen in the as-synthesized catalyst images. In addition, these results indicate that little, if any, oxidation of the catalyst has occurred, consistent with the Quantitative Rietveld XRD Analysis.

Overall, these TGA results give support to the proposed catalyst life progression. $NiMoO_4/MoO_3$ is carburized to form Ni/Mo_2C with significant interstitial carbon layers. When exposed to reaction conditions, a significant amount of the carbon layers are oxidized off, but the catalyst remains Ni/Mo_2C with little to no oxidation to MoO_2. Once deactivation occurs, however, a significant amount of Mo_2C oxidizes to MoO_2, and more Mo_2C oxidizes to MoO_2 as the catalyst is further exposed to reaction conditions after deactivation occurs. It is possible that the carbon layers are crucial to catalyst stability and, after all the excess carbon is oxidized off during the reaction, rapid catalyst deactivation occurs. Finally, these TGA results provide a clear indication that no coking of this Ni-based catalyst occurs when subjected to reaction conditions or with deactivation.

3.3.5 SEM-EDX

Figure 3.7 shows a set of SEM images of the Ni/Mo_2C catalyst exhibiting the morphological changes that occur between different timepoints in the reaction. In Figure 3.7a, the 1,000x image shows that the synthesized catalyst seems to be composed of particulates on the order of 1 to 20 microns in size. Upon closer inspection of the particulates at 100,000x, many features ~100nm or less in size are clearly evident. The catalyst heated to 950°C, Figure 3.7b, as well as the catalyst 100 minutes into the reaction, Figure 3.7c, show particulates of similar size as compared to the as-synthesized catalyst in the 1,000x images. However, in the 100,000x images, the features smaller than

100nm seem less prevalent in 7b and 7c than in 7a, indicating a degree of sintering during the heating and reaction processes.

The deactivated catalyst, both immediately after deactivation, Figure 3.7d, and 1 hour after deactivation, Figure 3.7e, exhibits a significant morphological change compared to the active catalyst. The particulates of the deactivated catalyst appear to be larger overall, with some particles almost 100 microns in size. In addition, the sub-100nm features seen in the active catalyst are not seen in the deactivated catalyst. Instead, there appears to be an agglomeration of several ~200-500nm sized regions. Quantitative Rietveld Analysis determined the crystallite sizes of Mo_2C and MoO_2 in the at-deactivation and 1 hour after deactivation samples to generally be between 300nm and 800nm, suggesting that these regions may be individual crystallites. Figure B17, which displays TEM images of NiMo-AsSyn, NiMo-15/15-MidRxn, NiMo-15/15-AtDeact, NiMo-15/15-1hrDeact, confirms these observations. These trends are consistent across all of the reaction conditions, as can be seen in Figures B18-B36, which depict SEM images of all the samples listed in Table 1.

Most striking in these images is the lack of any carbon filaments, indicative of "whiskering," in the catalyst at any point during the reaction process. Whiskering is a common and dangerous problem for Ni-based catalysts, especially under conditions where carbon formation is typically seen, such as the high temperatures and excess methane conditions used in this study. While an SEM image of a small portion of catalyst sample cannot be used to make any definitive claims about the rest of the sample, the lack of any evidence of whiskering in any images taken, combined with the XRD and TGA results gives strong support to the claim that whiskering does not occur, even under conditions favorable for coking to occur.

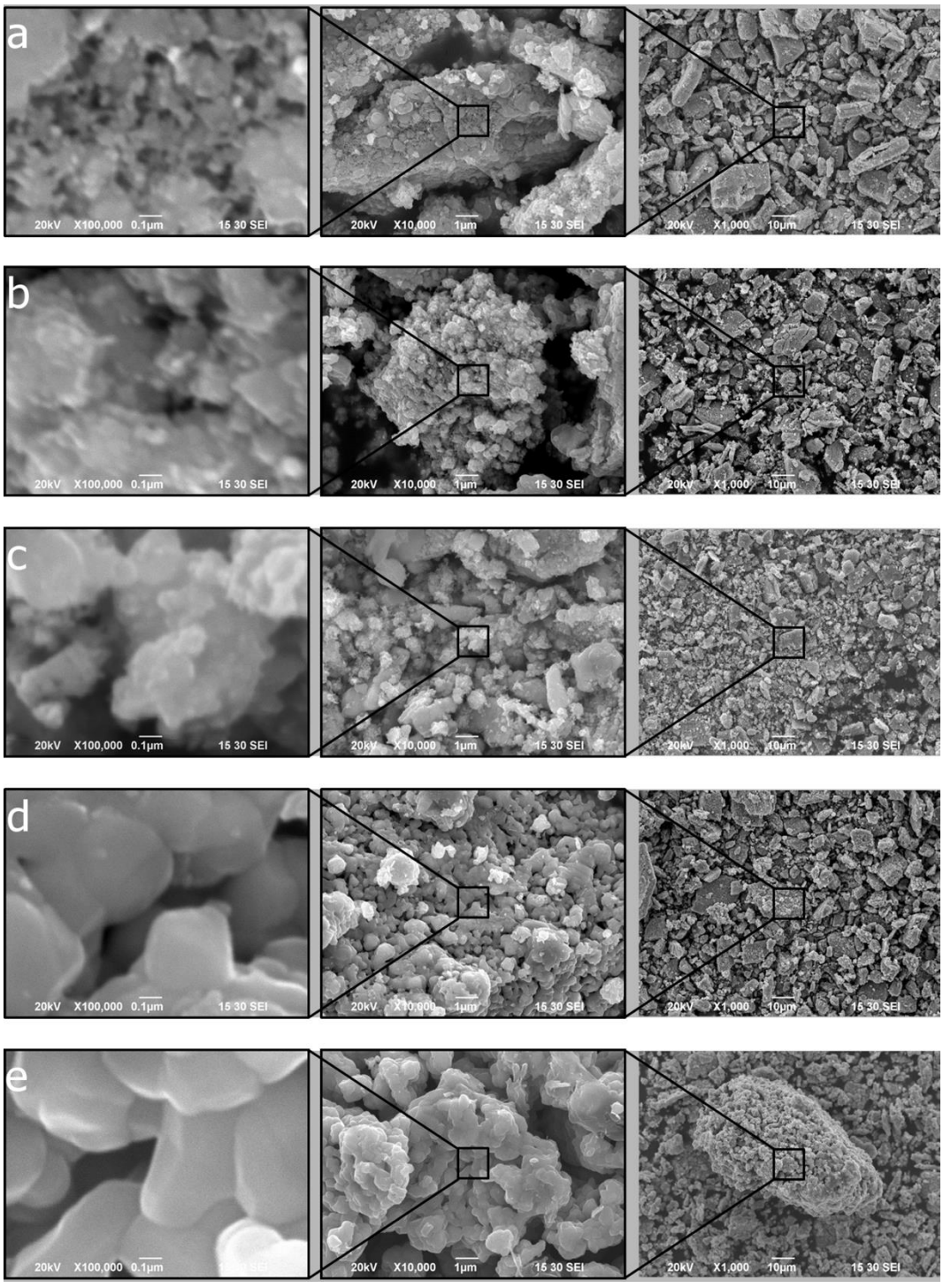

Figure 3.7: SEM images at 100,000x (left images), 10,000x (middle images), and 1,000x (right images) for a) NiMo-AsSyn, b) NiMo-950C, c) NiMo-15/15-MidRxn, d) NiMo-15/15-AtDeact, e) NiMo-15/15-1hrDeact.

Figure 3.8 depicts an SEM image (a) with EDX mapping of Mo (b), Ni (c), O (d) and C (e) for NiMo-30/0-MidRxn at 10,000X magnification. Similar SEM/EDX images at magnifications of 2,000x and 10,000x of NiMo-AsSyn, NiMo-0/30-MidRxn, NiMo-15/15-MidRxn, NiMo-30/0-MidRxn, NiMo-0/30-AtDeact, NiMo-15/15-AtDeact, NiMo-30/0- AtDeact, NiMo-0/30-1hrDeact, NiMo-15/15-1hr Deact, and NiMo-30/0-1hr Deact are shown in Figures B37-B56. Notice that many of the regions of high Ni concentration, indicated by bright yellow spots, have corresponding low concentrations of Mo, indicated by dark regions, as can be seen by comparing Figure 3.8b and Figure 3.8c. This suggests that the Ni is often present as a Ni-rich phase, on the order of a few microns in size, with little or no Mo incorporated in it, consistent with the XRD results. However, there are several regions of high Ni content that also exhibit some degree of Mo across all timepoints in the reaction. Similarly, the EDX picked up lower levels of Ni in each sample in regions not part of a large, distinct Ni-rich area. These phenomena can be caused by subsurface or nearby Mo or Ni, due to the ~micron-sized penetration depth of the EDX method. However, in the case of Ni, it is also possible that there are lots of very small crystallites of Ni distributed within the catalyst, as suggested by the TEM results.

The most striking aspect of this set of EDX images is the relative similarity of the element distribution, specifically the Ni regions, within the catalyst at all timepoints in the reaction run. All of the samples seem to show several distinct regions of high Ni concentration, with the sizes of these regions estimated at ~1-3μm. In addition, no major changes in the micron-scale Ni regions' size or distribution can be seen as the reaction progressed from "as-synthesized" to "mid-reaction" to "at deactivation" to "1 hour after deactivation." The mapping of O and C does not show any definitive trends or obvious regions of high O or C concentration within the catalyst. It is unknown whether this is due to relatively uniform distribution of C and O within the Ni/Mo_2C/MoO_2 material, or

whether it is due to ambient hydrocarbons and surface oxides. It is worth noting that while there does appear to be carbon present in most of the regions where Ni is also present, there does not appear to be a higher concentration of carbon near the Ni regions. This, along with the XRD, TGA, and SEM results, indicates that there is no evidence of coking or whiskering near the Ni regions, as would be expected for a Ni-based catalyst operating under the conditions used in this study.

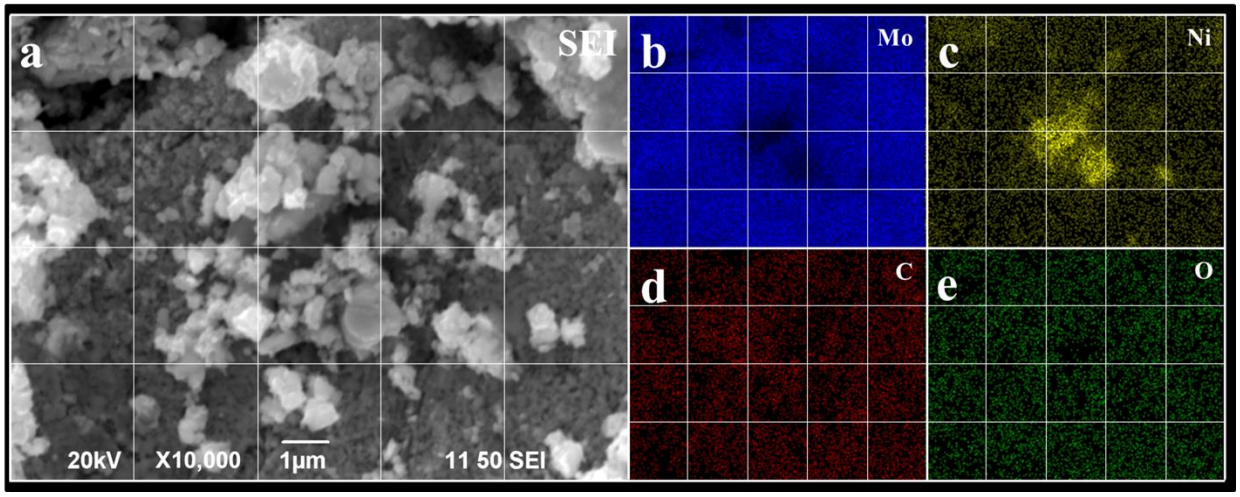

Figure 3.8: EDX mapping of NiMo-30/0-MidRxn at 10,000x. a) SEI; b) Mo; c) Ni; d) C; e) O. Image has been slightly brightened and white gridlines added for ease of visual inspection.

3.4 CONCLUSIONS

The Ni/Mo_2C catalyst is able to catalyze both the dry methane reforming and steam methane reforming reactions at 950°C. In addition, Ni/Mo_2C can catalyze the bireforming reaction by running CH_4, N_2, CO_2, and H_2O together. The H_2:CO ratios formed from different ratios of CO_2:H_2O follows the trend expected: the H_2:CO ratio increases from ~0.9 to ~3 as the oxidant mix goes from consisting entirely of CO_2 to consisting of a mixture of CO_2 and H_2O to consisting entirely of H_2O. This conclusively

demonstrates the ability to tune the H_2:CO ratio for methane reforming by co-running the dry reforming and steam reforming reactions over Ni/Mo_2C. In every reaction condition tested, the catalyst exhibited a similar reaction progression: very high initial activity that slowly declines over a period of 1-5 hours, then a rapid decline in conversion to less than 10% within 10 minutes which indicates catalyst deactivation.

Despite running the reaction at high temperature and with excess methane, this catalyst does not show any signs of coking or whiskering during the reaction or after deactivation, as would be expected for a Ni-based catalyst. Instead, the catalyst appears to deactivate via oxidation of the Mo_2C to MoO_2, as is more typical of Mo_2C based catalysts. In addition, with deactivation, the Ni phase appears to change as well, likely oxidizing somewhat and/or incorporating Mo into the Ni^0 phase. Future studies to determine the reaction and deactivation mechanisms would provide crucial insights into how to most effectively utilize this coke-resistant Ni-based methane reforming catalyst.

Chapter 4: Apparatus for Efficient Utilization of Isotopically Labeled Gases in Pulse Transient Studies of Heterogeneously Catalyzed Gas Phase Reactions*

4.1: INTRODUCTION

Understanding the chemical reaction kinetics of a heterogeneously catalyzed system is vital for being able to design a safe, efficient, and controllable chemical system. Traditional chemical kinetic analysis tends to require performing multiple steady-state experiments of a system across a range of temperatures, compositions, and other parameters.[109] In addition to being time- and resource- intensive, these techniques often are unable to distinguish kinetic parameters from mass transfer and other effects.[110] In contrast, transient techniques are often able to elucidate specific kinetic parameters with relatively few experiments, making them extremely useful methods for probing the reaction kinetics and other properties of chemical reaction systems.[111] One of the most powerful transient techniques is Steady State Isotopic Transient Kinetic Analysis (SSITKA), first developed by Happel,[112–114] Bennet,[115] and Biloen.[116]

In brief, the SSITKA technique involves bringing a catalytic reaction to steady state, then instantaneously switching one reactant with an isotopically labeled version of that same reactant. Assuming negligible kinetic isotope effects, the steady state reaction and associated kinetics are undisturbed by this switch to the isotopically labeled reactant. However, the presence and concentration of the isotopically labeled atom(s) in the reactant(s) and product(s) in the effluent can be monitored as a function of time using a mass spectrometer. Depending on the catalytic system, several valuable characteristics of the catalytic reaction can then be determined, such as mechanistic pathway insights, the

*This work has been submitted to *Reaction Chemistry and Engineering*: The author of this dissertation was responsible for designing and assembling apparatus, performing the SSITKA experiments and analyzing the data.

presence of multiple reaction steps in series or parallel, concentration of active surface intermediates, and turnover frequency (TOF). Shannon and Goodwin produced a detailed review of the SSITKA technique in 1995,[10] and Ledesma et al have produced an updated review covering the advancements from 1995 to 2014.[11] These reviews provide a comprehensive explanation of the SSITKA technique, as well as the deeper concepts, mathematics, and reaction system requirements needed for full interpretation of transient experimental results. While this manuscript will review some of the basic concepts as they relate to the data gathered using the described apparatus, readers are encouraged to consult these reviews for a more complete understanding of the SSITKA technique.

Despite the valuable mechanistic and kinetic information that can be acquired, SSITKA studies are not as widely used as they could be. Part of this is likely due to the high costs of isotopically labeled gases. Deuterium labeled gases are often some of the cheapest, but 1 liter (at STP) of deuterium labeled methane still costs ~$120 (as of publication date). More expensive gases, such as ^{13}C or ^{18}O labeled species often cost $250 or more for 1 liter at STP. This is on the order of 10,000x more than the non-isotopically labeled version of these reactants. In addition, the most common apparatus used to introduce the isotopically labeled gas underutilize much of it.

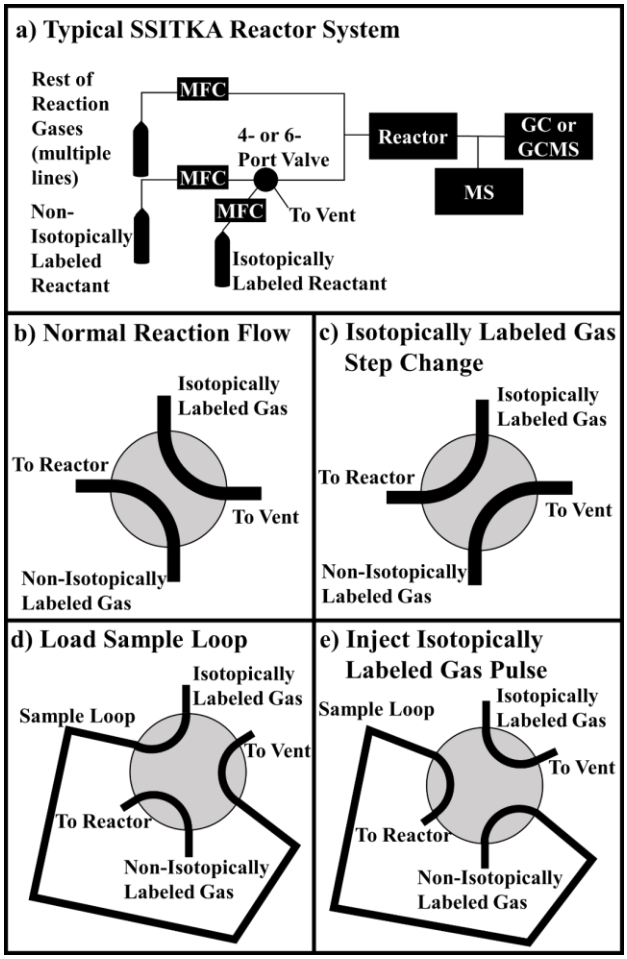

Figure 4.1: Typical reactor setup and valve schematics used in SSITKA experiments; a) Simplified reactor setup; b) 4-port valve position prior to step change to isotopically labeled reactant; c) 4-port position after step change to isotopically labeled reactant; d) 6-port valve position during loading of pulse of isotopically labeled reactant; e) 6-port valve position during injection of pulse of isotopically labeled reactant.

A typical SSITKA reaction system is displayed in Figure 4.1a, as well as the flow patterns of a 4-port valve (Figure 4.1b and 4.1c, used for step-change experiments) and a 6-port valve (Figure 4.1d and 4.1e, used for pulse experiments). A mass flow controller (MFC) flows the non-isotopically labeled reactant on one side of the valve, while a separate MFC flows the isotopically labeled version on the other side of the valve. A

backpressure regulator is often used to match the pressure in the isotopically labeled reactant stream to the reactor pressure, before the stream is vented to atmosphere. The 4- or 6-port valve is then turned, causing the isotopically labeled reactant to flow into the system as a step change or as a pulse replacing the non-isotopically labeled reactant. These system designs waste isotopically labeled gas by venting some of the gas prior to the switch. In addition, once the pressure in the bottle of isotopically labeled gas reaches the pressure used in the experiment, the residual gas left in the bottle and tubing cannot be easily recovered and used. Since the lecture bottles commonly used for these gases are not pressurized very high (typically less than 30psig for 1L at STP), the unrecoverable residual gas in the bottle can represent a significant portion of the total gas (~30% or so).

In this paper, we describe a novel apparatus for introducing pulses of isotopically labeled gases into a flow reactor system. This novel design eliminates the wasteful venting to atmosphere and allows the full contents of the gas bottle to be accessed. We estimate that a well-designed Pulse Injection Apparatus can utilize 90% of the isotopically labeled gas for experiments. The apparatus utilizes a 5-port valve, a sample loop, a vacuum pump, and a novel "bellows pump" component to introduce pulses of an isotopically labeled reactant to the reactor. In addition, the apparatus removes the requirement of using a mass flow controller for the isotopically labeled gas, reducing some capital expense. This apparatus can also be built relatively inexpensively, and installed onto a new or existing transient experiment system.

This apparatus has been previously used to study the dissociation mechanism of methane over a Mo_2C catalyst.[15] Earlier studies had used a $^{13}CH_4$ experiment to assert that carbon exchange occurred between methane and the Mo_2C catalyst above 550°C.[82] However, by performing $^{13}CH_4$ and CD_4 pulse experiments at several temperatures, it was demonstrated that carbon exchange did, in fact, not occur, and that methane likely

adsorbed on Mo_2C via a single C-H bond dissociation/recombination mechanism. Finally, while we primarily describe use of this apparatus for SSITKA experiments, it likely can be used or modified for use in many different types of transient pulse experiments.

4.2: Description of Apparatus and System

4.2.1: Reactor System and Apparatus Overview

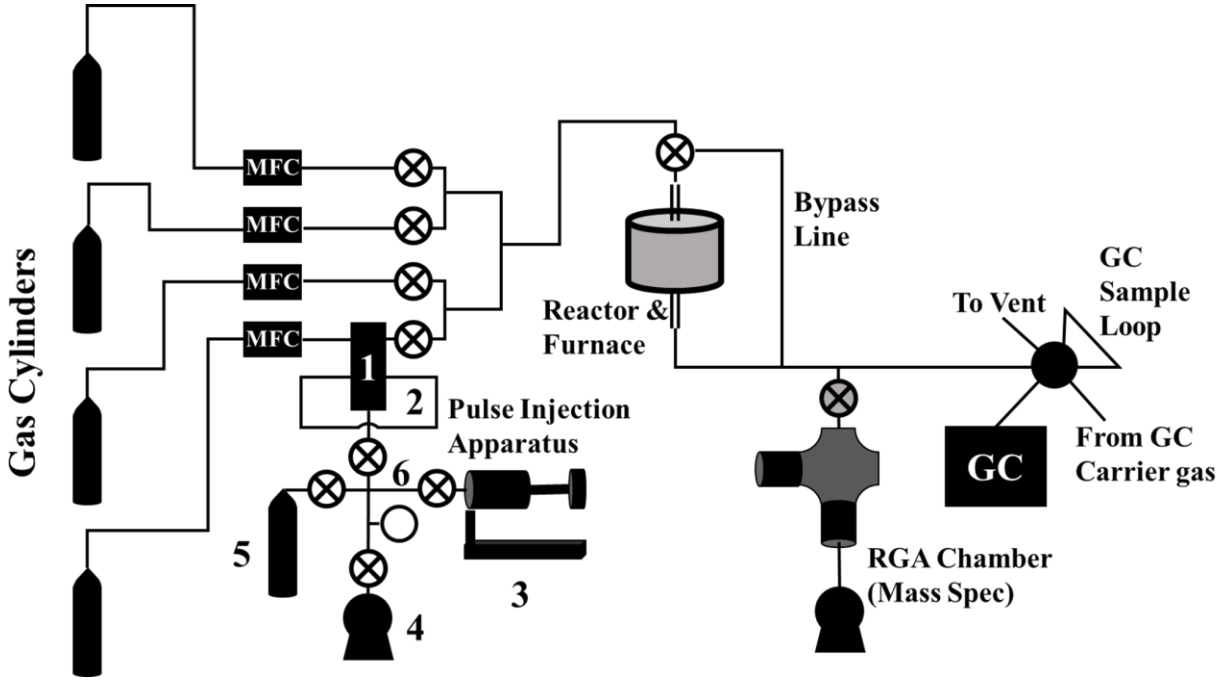

Figure 4.2: Diagram of our reactor system, including the Pulse Injection Apparatus, the components of which are labeled with numbers.

A diagram of our reactor system, including the Pulse Injection Apparatus, is shown in Figure 4.2. From left to right, our reaction system consists of:

- The reactant gas cylinders, the bottom of which contains the non-isotopically labeled reactant, typically mixed with a small amount of inert tracer gas, such as Ar or He
- Mass Flow Controllers for controlling the flow of the reactant gases (labeled “MFC”),
- The Pulse Injection Apparatus, described in more detail below

- A reactor, which, in our system, consisted of a vertical quartz reactor tube heated by an external furnace,

- An in-line Mass Spectrometer. In our system, this consists of a 6-way cross UHV chamber, an Extorr XT100 Residual Gas Analyzer (RGA) equipped with a quadrupole mass spectrometer, a leak valve connected inline for continuous sampling of the effluent stream, a turbomolecular pumped backed by a mechanical vacuum pump, and an ion gauge for measuring chamber pressure

- A gas chromatograph for quantitatively measuring the chemical composition of the product stream.

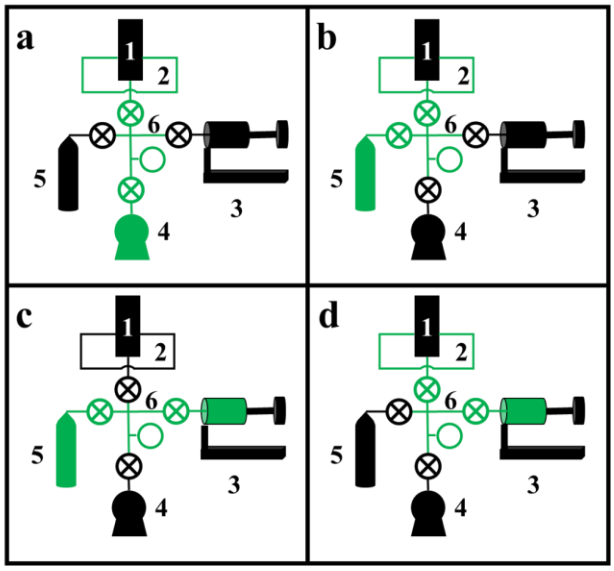

Figure 4.3: Common component connections used in the operation of the Pulse Injection Apparatus. Green indicates opened valves and connected components; a) Vacuuming out sample loop in preparation for loading of isotopically labeled gas; b) Loading sample loop with isotopically labeled gas from gas cylinder; c) Extracting isotopically labeled gas from cylinder with bellows pump; d) Adjusting pressure in sample loop using bellows pump.

The apparatus consists of 6 basic components, labeled with numbers in Figure 4.3: 1) A two-position, five-port valve, 2) a sample loop connected to the 5-port valve, 3) the "bellows pump," which can be expanded and contracted to move gas between components and adjust pressure, 4) a vacuum pump, 5) the isotopically labeled gas cylinder, and 6) the valve manifold. Although each component will be described in more detail below, Figure 4.3 depicts the 4 basic steps for loading the sample loop with the isotopically labeled gas. In each diagram, the green lines indicate open valves and connected components. In Figure 4.3a, the vacuum pump is connected to the sample loop to evacuate the sample loop. In Figure 4.3b, the isotopically labeled gas cylinder is connected to the sample loop to fill it with isotopically labeled gas. In Figure 4.3c, the bellows pump is connected to the isotopically labeled gas cylinder and expanded to extract gas from the cylinder, if needed. Finally, in Figure 4.3d, the bellows pump is connected to the sample loop, and is expanded or contracted to adjust the pressure in the sample loop to match that in the reactant stream. To inject the pulse, the switch on the 5- or 6- port valve is flipped, diverting the reactant stream to the sample loop and causing the non-isotopically labeled reactant gas to push a pulse of isotopically labeled reactant gas through the reactor system.

4.2.2: 5-port valve

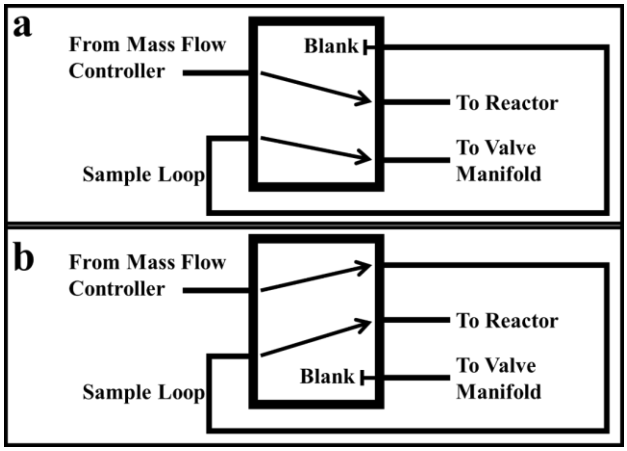

Figure 4.4: Basic flow schematic of 5-port valve used in the Pulse Injection Apparatus; a) "Load" position, where isotopically labeled gas is loaded into sample loop; b) "Inject" position, where pulse of isotopically labeled reactant is injected into reaction system.

The 5-port valve operates similarly to a common 6-port GC injection valve. In fact, a 6-port GC valve with one port capped (the port that would otherwise lead to vent) could easily substitute for the 5-port valve we employ. The flow patterns of the 5-port valve in the "Load" and "Inject" positions are depicted in Figures 4.4a and 4.4b, respectively. In the "Load" position, the non-isotopically labeled reactant flows directly in and out of the valve. Meanwhile, the sample loop is connected through the 5-port valve to the valve manifold on one end, and a blank or cap on the other. In the "Load" position, the sample loop can be vacuumed out and charged with the appropriate pressure of isotopically labeled gas without affecting the reactant gas stream. In the "Inject" position, the non-isotopically labeled reactant flowrate is diverted to the sample loop, before continuing on to the reactor, pushing the pulse of isotopically labeled reactant through the reactor system. In this position, the piping from the valve manifold is connected to a blank or plug. Once the pulse has worked its way through the reactor system, the 5-port valve can be switched back to the "Load" position with no effect on the ongoing

experiment, and another pulse of isotopically labeled gas can be loaded into the sample loop.

The 5-port valve we used in designing this system is a Sizto Tech Corporation (www.STCValve.com) Manual Hand Valve (model # MPV522), though any valve with good leak properties under vacuum and functionally similar flow patterns as Figures 4.3a and 4.3b is adequate for this process. Short Male NPT (MNPT) to Female VCR (FVCR) connections were installed onto each port. These connections allowed easier installation onto the existing reactor system tubing. In addition, these allowed greater versatility in using and changing sample loops.

4.2.3: Sample Loop(s)

As indicated before, the 5-port valve was fitted with short MNPT to FVCR connections. Sample loop(s) are fabricated by fitting a Male VCR (MVCR) connection onto each end of a length of tubing, then coiling and shaping the tubing so the MVCR connections can be connected to the proper FVCR connections on the 5-port valve, and so the tubing fits in its allocated physical space. The volume of a sample loop can be determined by multiplying the length by the internal cross-sectional area of the tubing. The exposure time of the isotopically labeled pulse to the reaction system can be determined by dividing the sample loop volume by the reactant flowrate. In addition, multiple sample loops can be fabricated, providing a range of sample loop sizes that can easily be exchanged on the 5-port valve. While the valve is in the “Load” position, the sample loop can be removed and exchanged during a reaction run without disturbing the ongoing experiment.

4.2.4: Bellows Pump

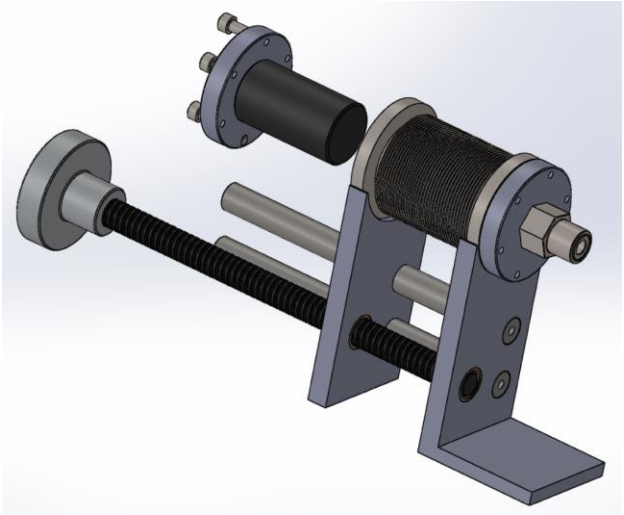

Figure 4.5: Exploded diagram of Bellows Pump component.

A key component of the Pulse Injection Apparatus described in this paper is the "bellows pump." An exploded diagram of the bellows pump can be seen in Figure 4.5. In addition, a 3-D PDF diagram and SolidWorks file are downloadable in the Supplementary Information. A compressible/expandable edge welded bellows with ConFlat (CF) connections is attached to a metal plate on each end. The plates are connected to each other by two rods and bushings, as well as a worm gear with a hand crank. Thus, by turning the hand crank, the bellows is expanded or compressed, increasing or decreasing the volume inside the bellows pump, respectively. When the bellows pump is connected to the sample loop via the valve manifold, expanding or compressing the bellows pump allows the pressure in the sample loop to be adjusted. In addition, by expanding the bellows pump while connected to the isotopically labeled gas cylinder, gas can be extracted from the cylinder, even at pressures less than atmospheric pressure. Then, the bellows pump can be compressed while connected to the sample loop, delivering the extracted gas to the sample loop at the desired pressure. An off-the-shelf

Ultra-High Vacuum linear translator, such as those sold by Kurt J. Lesker (www.lesker.com), could be modified to work as a bellows pump for those not interested in custom building a bellows pump.

A key feature of the bellows pump that increases gas transfer efficiency is the cylindrical plug attached to one flange of the bellows pump. The purpose of this plug is to occupy the empty space in the bellows pump when the bellows is completely compressed. The less empty space in the bellows pump and tubing there is, the more efficient the bellows pump will be. Our solid aluminum cylindrical plug is attached to the cap using a small threaded rod, and does not need to have an air-tight seal to the cap. In our design, we found that the stationary end of the bellows pump should be connected to the valve manifold tubing, while the cylindrical plug is attached to the flange on the moveable end. This allows a short piece of fixed, hard tubing to be used in the connection between the bellows pump and the valve manifold.

4.2.5: Vacuum Pump

The vacuum pump we used was a common rotary vane mechanical vacuum pump. A convectron gauge was installed near the inlet of the vacuum pump to monitor the pressure as well as allow leak-checking of the apparatus. In our apparatus, achieving a base pressure in the low 10^{-2} Torr range for each section indicated acceptably low leakage rate.

4.2.6: Isotopically Labeled Gas Cylinder

This section of the isotope sample loop apparatus is relatively simple. It typically consists of a lecture bottle of isotopically labeled gas, a CGA 170 regulator, and tubing to connect the regulator to the valve manifold. To improve gas recovery efficiency, the

length of tubing used between the regulator and valve manifold should be as short as possible.

4.2.7: Pressure Gauge(s)

In our diagrams, a pressure gauge is part of the valve manifold, depicted by the open circle in Figures 4.2 and 4.3. The primary use of this pressure gauge is to match the pressure in the sample loop with the pressure of the reactant in the reactor system. A mechanical gauge is generally preferable since convectron gauge readouts are affected by a gas' molecular weight. However, with proper calibration for each gas used, a convectron gauge would likely provide better accuracy. A compound gauge is used, since the system will be subject to both vacuum and pressures at or above atmospheric pressure regularly. While we only used one pressure gauge, attached to the valve manifold, in our initial construction, we recommend that other researchers also install a pressure gauge on the reactant gas line of the reactor system. This allows researchers to better match the pressure in the sample loop to the pressure in the reaction system. We found that there was benefit to having the pressure gauge on the valve manifold, as it allowed measurement of the pressure in the bellows pump section and isotopically labeled gas cylinder section.

4.2.8: Piping and valve manifold

The various sections of the apparatus are all connected to each other using a valve manifold, each separated from the manifold using a ball valve. The simplest and shortest setup would be a 4-way cross connected to 4 ball valves. A tee can be added in between the cross and one of the ball valves to accommodate the pressure gauge, if desired. It should be noted that longer tubing lengths in the valve manifold contribute to more waste

and less efficient gas transfer, as the gas in the manifold is lost when the manifold is used to connect the vacuum pump to the sample loop in between gas loadings.

4.2.9: Suggestions regarding vacuum

Working with vacuum requires constant attention to the possibility of leaks. Leaks are inevitable, even in well-sealed systems. As such, we have compiled some general rules for operating this system:

- Periodically leak-check the system. Leak-checking involves connecting a portion of the apparatus to the vacuum pump and monitoring the final base pressure, which should not change significantly day-to-day. Leak-checking the bellows pump leg and the isotopically labeled gas cylinder leg is often done after installing a new isotopically labeled gas cylinder onto the apparatus, since these lines must be vacuumed out anyways.
- Use tubing and connections designed to hold vacuum. Stainless steel tubing, ConFlat (CF) connections and VCR connections are preferred. NPT and Swagelok^{TM} type fittings may also be acceptable, but tend to leak more than CF and VCR fittings.
- The valve manifold and 5-port valve leg, including the sample loop, should be pumped out immediately prior to filling with isotopically labeled gas for a pulse experiment. Keeping the tubing below atmospheric pressure without active vacuum pumping allows air to leak in and possibly contaminate the isotopically labeled gas. The vacuum step should also be used as a leak check of the valve manifold, 5-port valve, and sample loop.
- The bellows pump leg and the isotope gas cylinder leg should be kept above atmospheric pressure except during sample loop loading. This ensures any

leakage is a small amount of isotopically labeled gas out to atmosphere, not air into the tubing. Allowing air to leak in can contaminate much/all of the isotopically labeled gas. If a leg has been below atmospheric pressure for a significant amount of time, it may be best to pump out that line instead of risk contaminating the rest of the isotopically labeled gas.

- Gas that would be otherwise lost (such as the isotopically labeled gas in the valve manifold) can be partially recovered by expanding the bellows to extract the gas.

4.2.10: Requirements for the rest of the system

Since our apparatus can be used by researchers just starting transient experiments, we would like to share some observations we have made that may be useful to others designing their own system. Researchers should consult previous literature for the design of reactors, catalyst beds, etc. that are most relevant to them.

When designing the system, one should minimize the possibility of pulse broadening by minimizing mass transfer effects through the rest of the system. The length of tubing from the Pulse Injection Apparatus to the reactor and then to the analytical instruments should be as short as possible. The smallest inner diameter tubing feasible for operation should also be used (we used ¼" tubing in our reactor). In addition, dead legs should be avoided or minimized.

Researchers also must choose the type of analytical instruments to use. The most common choice is using an on-line mass spectrometer and/or a gas chromatography/mass spectrometer (GCMS). Each has their benefits and downsides.

With an on-line mass spectrometer, the masses of interest are essentially monitored continuously (typically with a resolution of 1 second or less, depending on number of masses monitored, dwell time, and other factors). This resolution allows

phenomena to be observed that might not be detectable with the GCMS resolution. In addition, one is able to track the changes in the baseline for each mass, which can improve accuracy. However, there are several downsides. First, since all species are being detected by the mass spectrometer at once, careful consideration must be given to the fragmentation patterns of each species, including the isotopically labeled species. The National Institute of Standards and Technology provides the mass spectrometer fragmentation patterns of most common molecules.[117] This means that reactions involving only relatively simple species with minimal fragmentation overlap will be the easiest to interpret. This is especially true for C_{2+} species, which often tend to have significant overlap with each other. In addition, the inert tracer and inert carrier gas must be carefully chosen so there is zero-to-minimal overlap with each other or any other species. Finally, mass spectrometry is only semi-quantitative, so a second analytical technique, such as gas chromatography, must also be used to quantitatively determine conversion, selectivity, etc.

Using a gas chromatograph/mass spectrometer (GCMS) is the other analytical technique often used for transient studies. In general, multiple samples are collected in separate sample loops, then analyzed using the GCMS. The resolution achieved with this technique is limited by the number of samples taken and the length of time over which they were taken, and is unlikely to achieve comparable resolution to an online mass spectrometer. However, using a GCMS has several benefits. Since the GC separates components prior to analysis with the MS, fragmentation overlap between species is not as big of a concern. This allows more complex reactants and products to be studied, though their fragmentation patterns must still allow detection of the isotopically labeled atom in the species. Other techniques generally require the use of a GCMS, such as

methanation of C_{2+} species after separation by GC,[118–123] which is useful for studying Fischer-Tropsch reactions.[124,125]

4.3: Data Obtained From Pulse Experiments

The data obtained from these pulse experiments can be treated as with any other pulse or transient methods. The reviews by Shannon and Goodwin[10] and Ledesma et al.[11] provide extensive explanations of the various analyses that can be made, along with the assumptions and mathematics required. While most of these techniques are described for step functions, they can apply to pulse functions as well. In fact, if the length of the pulse is long enough for the isotopically labeled species to saturate the system, these pulse functions can represent two step functions in the same experiment. One step introduces the isotopically labeled species to the system, and one step reintroduces the non-isotopically labeled species back into the system. Here, we will present some preliminary data we have acquired from our Pulse Injection Apparatus, along with the most common analysis performed in SSITKA studies.

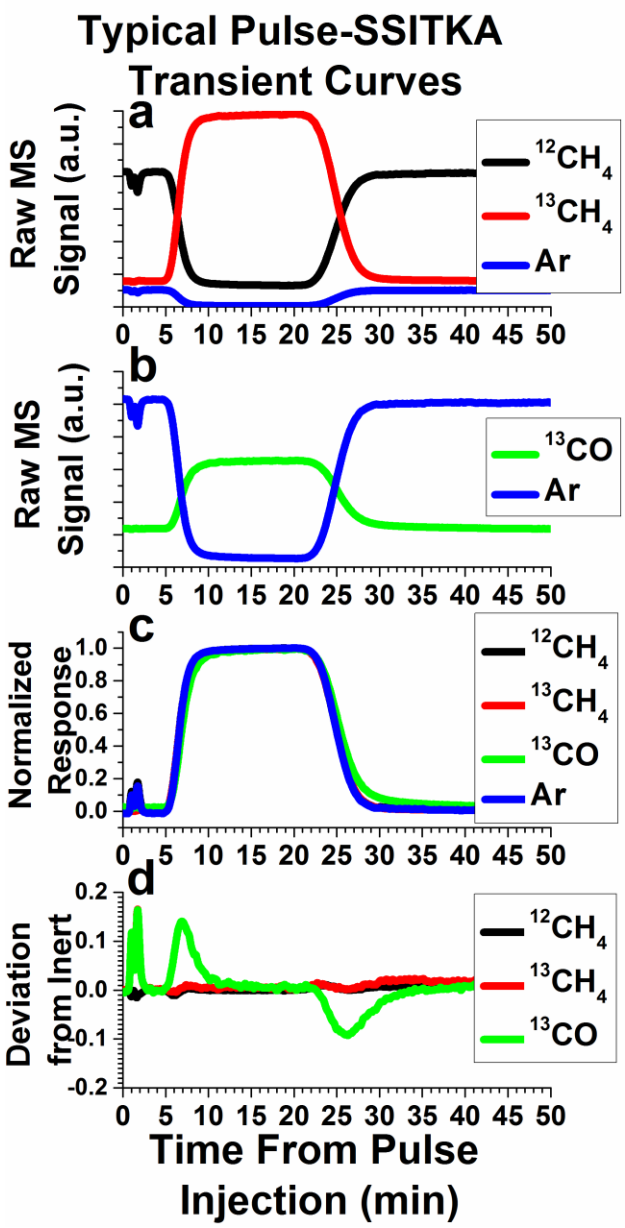

Figure 4.6: Sample SSITKA experiment data and analysis from a $^{13}CH_4$ pulse during dry methane reforming reaction ($CH_4 + CO_2 \rightarrow 2CO + 2H_2$); a) Mass spectrometer signal of $^{12}CH_4$ (m/z = 15, black), $^{13}CH_4$ (m/z = 17, red), and the Ar inert tracer (m/z = 40, blue); b) Mass spectrometer signal of ^{13}CO (m/z = 29, green) and the Ar inert tracer (m/z = 40, blue); c) Mass spectrometer signals from (a) and (b) normalized to span from 0 to 1 to 0 during the pulse; d) Difference curve for $^{12}CH_4$, $^{13}CH_4$, and ^{13}CO, created by subtracting each curve in (c) from the Ar inert tracer curve in (c).

Figure 4.6 depicts the results and analysis of a Pulse-SSITKA experiment performed to probe a dry methane reforming reaction ($CH_4 + CO_2 \rightarrow 2CO + 2H_2$) over a Mo_2C catalyst. This data is presented for demonstration purposes only, in order to provide the reader with an idea of the type of data and analysis gained from this apparatus and experiments performed on it. In this experiment, a pulse of isotopically labeled reactant, $^{13}CH_4$, replaced the non-isotopically labeled reactant, $^{12}CH_4$, and the resulting isotopically labeled product, ^{13}CO, was monitored. The non-isotopically labeled reactant ($^{12}CH_4$) contains 5% Ar, used as an inert tracer. Addition of an inert tracer gas is a common method used in SSITKA experiments for determining the gas phase holdup of the reactor system, essentially the mass transport function of the pulse without influence from any reaction. In Figure 4.6a, the raw mass spectrometry signals of $^{12}CH_4$, $^{13}CH_4$, and Ar are depicted. Note that the pulse is characterized by the disappearance of the inert tracer and $^{12}CH_4$, and a corresponding increase in $^{13}CH_4$, as would be expected. Figure 4.6b depicts the mass spectrometer signal of the Ar inert tracer as well as ^{13}CO, which shows an increase during the pulse, as would be expected.

Figure 4.6c depicts one of the most common first analysis performed on a SSITKA experiment. The mass spectrometry signals for each species are normalized, and some are inverted (in this case, Ar and $^{12}CH_4$), so that all of the MS signals to span from 0 to 1 during the time period of the transient pulse experiment. As stated earlier, the normalized curve of the Ar inert tracer's mass essentially represents the mass transport function of the isotopically labeled pulse. The normalized curves of both $^{12}CH_4$ and $^{13}CH_4$ line up with the inert tracer curve, indicating that the reactant does not experience any significant delay compared with the gas phase holdup of the system. However, the ^{13}C atom in the $^{13}CH_4$ takes some time making its way through the mechanistic steps of the reaction before emerging from the catalyst into the gas stream as isotopically labeled

product. This causes a delay in the emergence of the ^{13}CO compared with the mass transport function of the pulse. As a result, the normalized curve of ^{13}CO will exhibit a deviation from the normalized Ar inert tracer curve, as can be seen in Figure 4.6c.

One key parameter often determined is the mean surface residence time of the isotopically labeled atom (^{13}C) on the catalyst surface. Physically, this is the average time the isotopically labeled atom spends on the catalyst's surface, a function of both reaction rates and the number of active surface intermediates that the isotopically labeled atom can reside in. Graphically, this is represented by the space between the normalized inert tracer curve and the isotopically labeled product curve. The simplest way to determine the mean surface residence time is to subtract the normalized curve of a species of interest from the normalized inert tracer curve. This "residual" function for our sample data is plotted versus time in Figure 4.6d, and is calculated by subtracting the $^{12}CH_4$, $^{13}CH_4$, and ^{13}CO curves from the Ar curve in Figure 4.6c. Since both $^{12}CH_4$ and $^{13}CH_4$ did not deviate significantly from the inert tracer, their plots in Figure 4.6d do not exhibit any significant peaks. However, due to kinetic steps causing a deviation of the isotopically labeled product (^{13}CO) from the gas phase holdup, two peaks can be easily seen for ^{13}CO in Figure 4.6d. Integrating the area under the peaks produced by this analysis is the area between the inert and isotopically labeled product curve, providing the mean surface residence time. This is true no matter the complexity of the system, reaction pathway, or reaction order. Other methods, such as fitting exponential decay curves or more complex modeling can also be used, but must be tailored to match a postulated reaction pathway.[10,11] Note that, in Figure 4.6c, deviations of ^{13}CO from the Ar inert curve are seen both at the beginning and the end of the pulse. In Figure 4.6d, this results in two peaks of approximately equal size, with the first positive and the second negative. As a result, two kinetic measurements of the reaction system can be made.

However, the measurement from the introduction of the pulse (first peak) is likely more accurate, due to less broadening via mass transfer effects.

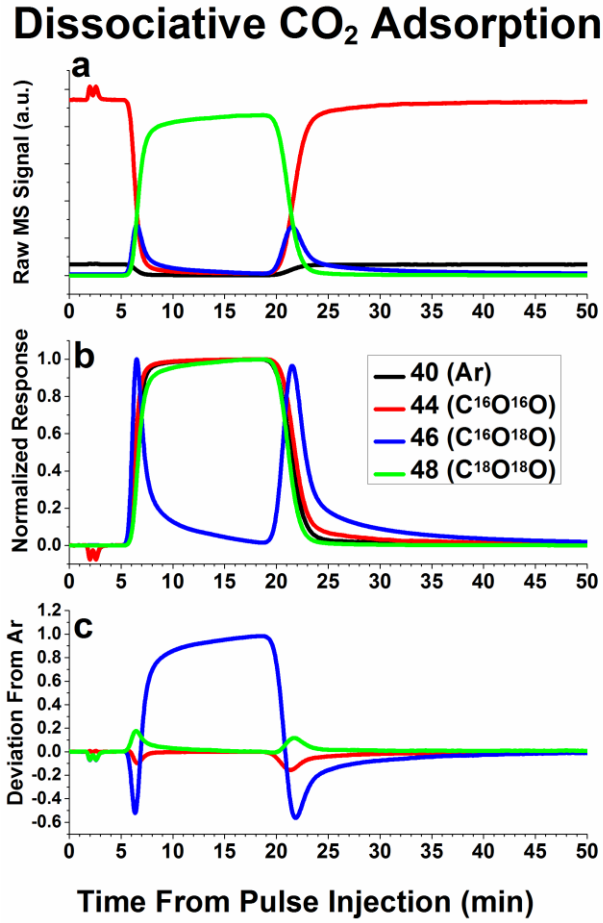

Figure 4.7: SSITKA data and analysis of a pulse of $C^{18}O_2$ replacing $C^{16}O_2$ in a reaction system involving rapid dissociation/recombination of CO_2. Species monitored are: Ar inert tracer (m/z = 40, black), $C^{16}O_2$ (m/z = 44, red), $C^{16}O^{18}O$ (m/z = 46, blue), and $C^{18}O_2$ (m/z = 48, green); a) Raw mass spectrometer signal; b) Normalized curves, where Ar (m/z = 40, black) and $C^{16}O_2$ (m/z = 44, red) have been inverted in addition to normalizing; c) Deviation of the $C^{16}O_2$ (red), $C^{16}O^{18}O$ (blue), and $C^{18}O_2$ (green) from the Ar inert tracer, calculated by subtracting the respective CO_2 normalized curves in (b) from the normalized Ar inert tracer curve in (b).

The review by Shannon and Goodwin[10] provides several qualitative observations one can make about the reaction mechanisms based on the shape of the isotopically

labeled product curves. One special case we found easily distinguishable in the pulse experiments inherent to our system was that of rapid dissociation/recombination of a molecule containing 2 isotopically labeled atoms. Figure 4.7 depicts an example of this phenomenon using $C^{16}O_2/C^{18}O_2$, but we have also seen this phenomenon with H_2/D_2 and CH_4/CD_4[15]. Since the pulse function is not a perfect rectangle, due to diffusion and other broadening effects, there is a period of time where both $C^{16}O_2$ and $C^{18}O_2$ are in the reactant stream at the same time. For a reaction system that involves rapid dissociation and recombination of CO_2, $C^{16}O^{18}O$ will be formed during these periods of overlap, as can be seen as peaks of $C^{16}O^{18}O$ in Figure 4.7a. Since both $C^{16}O_2$ and $C^{18}O_2$ are being consumed to create $C^{16}O^{18}O$, during the switch from $C^{16}O_2$ to $C^{18}O_2$, the $C^{16}O_2$ seems to disappear faster than the Ar inert tracer, while the $C^{18}O_2$ appears to emerge slower than the Ar inert tracer disappears, as can be seen in Figure 4.7b. At the end of the pulse, during the switch back from $C^{18}O_2$ to $C^{16}O_2$, a similar behavior is seen: the $C^{18}O_2$ seems to disappear faster than the Ar tracer reappears, while the $C^{16}O_2$ seems to reappear slower than the Ar tracer. This results in the distinctive phenomenon of both peaks of $C^{16}O_2$ in the residual plots curve being negative and both $C^{18}O_2$ peaks being positive, as can be seen in Figure 4.7c. As a result, the mean residence time of the species involved cannot be measured simply by integrating the area under the peaks in the residual plots curve, but must be calculated using the gas phase holdup function (ie Ar inert tracer function) as well as the dissociation and recombination probabilities. However, one can gain insights into dissociation mechanisms via this technique, as was done previously by Brush et al., who used this technique to determine the dissociation mechanism of CH_4 over Mo_2C.[15] Peaks of CH_3D and CD_3H were present during these "overlap" periods, but not CH_2D_2, indicating that the dissociation mechanism involved dissociation of a single C-H bond, not multiple C-H bonds, as had been previously suggested. Similar reaction mechanism

insights could be gained by using reactants with multiple isotopically labeled atoms, and monitoring the relative emergence and disappearance of products containing zero, one, two, etc. of the isotopically labeled atoms.

4.4: CONCLUSIONS

Transient studies are extremely powerful tools for probing the mechanisms and kinetics of reaction systems. However, the high cost of isotopically labeled gases combined with the relatively few experiments each bottle provides makes these experiments quite expensive.

We have designed and fabricated a new apparatus for introducing isotopically labeled gases into a flow reactor system for the purpose of performing transient kinetic experiments. This apparatus is relatively easy and inexpensive to build, and can be installed onto new or existing systems. This apparatus allows significantly more efficient utilization of the isotopically labeled gas. Experimental studies that would normally have been prohibitively expensive due to the cost of the isotopically labeled gas are now more feasible with the use of this apparatus. In addition, pulse studies have some advantages over step studies. Pulse experiments inherently produce two measurements of the reaction transients and often can provide mechanistic insights that step experiments cannot. This apparatus could make isotopic transient studies and other pulse transient studies more accessible to more researchers, while potentially providing more mechanistic insight than currently used methods.

Chapter 5: Evidence of Methane Adsorption Over Mo_2C Involving Single C-H Bond Dissociation Instead of Facile Carbon Exchange*

5.1 INTRODUCTION

Transition metal carbides have been a focus of research since Levy and Boudart first demonstrated that tungsten carbide exhibited catalytic similarity to Pt.[61] Further, molybdenum carbide (Mo_2C) based catalysts have been an active area of research since Claridge et al. demonstrated the ability of Mo_2C to catalyze methane reforming reactions with high activity, comparable to 5% Ir/Al_2O_3 or 5% Rh/Al_2O_3.[72] Subsequent research has demonstrated Mo_2C as an active catalyst for Dry Methane Reforming,[69,74,79,84,85] Steam Methane Reforming,[72,81] Water Gas Shift,[70,81] and several other reactions.[65,77,94] Despite this interest, the mechanisms of reactions on Mo_2C based catalysts, and carbide catalysts in general, are still somewhat speculative. Claridge et al originally proposed two possible mechanisms for carbide catalysts.[72] One is the redox mechanism, involving formation of a carbon vacancy (denoted by "[]") by the oxidant, followed by carbon from methane decomposition filling the carbon vacancy:

(1) $CO_2 \rightarrow CO + O^*$

(2) $Mo\text{-}C\text{-}Mo_{(s)} + O^* \rightarrow Mo\text{-}[]\text{-}Mo + CO$

(3) $Mo\text{-}[]\text{-}Mo_{(s)} + O^* \rightarrow Mo\text{-}O\text{-}Mo$ (oxide, beginning of catalyst deactivation)

(4) $CH_4 \rightarrow C^* + 2H_2$

(5) $Mo\text{-}[]\text{-}Mo_{(s)} + C^* \rightarrow Mo\text{-}C\text{-}Mo$

*Where * denotes an absorbed surface species*

*This work was previously published: A. Brush, G. M. Mullen, R. Dupré, S. Kota and C. B. Mullins, *React. Chem. Eng.*, 2016, **1**, 667–674. The author of this dissertation was responsible for developing and conducting the SSITKA and ramp experiments and analyzing the data.

This mechanism implies active participation of the carbide carbon in the reaction, similar to a Mars-van Krevelen type mechanism. The suggestion that the carbon in the carbide may participate in the reaction makes some intuitive sense. Mo_2C is often synthesized from MoO_3 using temperature programmed reduction in hydrogen and methane, indicating that methane can decompose to form carbide carbon.[68,77,126] Additionally, most Mo_2C catalysts deactivate via oxidation to MoO_2, indicating that the oxidant (often CO_2 or H_2O) is able to react with a carbide carbon and remove it.[69,72,81,85] In addition, reaction (3) also provides a potential a first step for catalyst deactivation when an oxygen atom fills the vacancy instead of carbon.

The second mechanism is a more traditional noble metal type mechanism, not directly involving the carbide carbon in the reaction mechanism:

(6) $CH_4 \rightarrow C^* + 2H_2$

(7) $CO_2 \rightarrow CO + O^*$

(8) $O^* + C^* \rightarrow CO$

Claridge et al noted that both of these mechanisms are likely important, and subsequent theoretical calculations have given evidence for both types of reactions.[72] Medford et al performed DFT calculations of elementary syn-gas reactions over Mo_2C, and found that the binding energies for carbon species on Mo-terminated Mo_2C were very close to Ru, Ir, Rh, and Pd, noble metal catalysts Mo_2C is often compared to.[127] However, the binding energies for oxygen species on Mo_2C are different than the noble metals. Overall, the Medford et al study gives evidence that reactions on Mo_2C can proceed via a noble-metal type mechanism, but there may be selectivity differences due to the differences in oxygen bonding.[127] Tominaga and Nagai found that methane

dissociatively adsorbs as CH_3 + H on β-Mo_2C (001), with the CH_3 species stabilized in the 3-fold Mo site.[128] Liu and Rodriguez performed a thorough DFT study of the water gas shift reaction on molybdenum carbide. They compared the kinetics of the WGS reaction on a Cu surface to Mo-terminated α-Mo_2C (001), C-terminated α-Mo_2C (001), oxygenated Mo-terminated α-Mo_2C (001), and oxygenated C-terminated α-Mo_2C (001).[129] They found that the C-terminated Mo_2C can stabilize the oxygen species, and react to form a CO molecule. A similar finding that an absorbed oxygen atom (O*) can react with a carbide carbon to produce a carbon vacancy and desorb as CO on β-Mo_2C was recently published by Shi et al.[130]

In addition, a few isotopically labeled experiments have demonstrated that the carbide carbon can participate to some degree in various reactions. Shou and Davis performed a Steady State Isotopic Transient Kinetic Analysis (SSITKA) experiment, where they switched from ^{12}CO to ^{13}CO during a reaction of H_2 and CO to form CH_4 and C_{2+} products.[118] In addition to measured transient responses, they saw a persistent background of ^{12}C in the CH_4 and C_{2+} species, indicating some of the ^{12}C from the Mo_2C support was participating in the reaction even an hour after the switch to ^{13}CO. Xiao et al synthesized $Mo_2{}^{13}C$, then performed several pulses of $^{12}CH_4$ + O_2 and monitored the amounts of ^{12}C and ^{13}C in CO and CO_2 produced.[76] The first pulse showed that the majority of the carbon in the produced CO and CO_2 was ^{13}C. The subsequent pulses showed declining amounts of $^{13}CO/^{13}CO_2$ and increasing amounts of $^{12}CO/^{12}CO_2$. Finally, Naito et al flowed $^{13}CH_4$ and $^{13}CO_2$ over unsupported $Mo_2{}^{12}C$ and $Mo_2{}^{12}C$ supported on ZrO_2 to produce CO and H_2.[131] They found that almost 50% of the CO produced initially was ^{12}CO. Overall, these results show a definite participation of the carbide carbon from the Mo_2C in these reactions.

The most surprising result from an isotopic study was reported by LaMont et al.[82] They flowed pure $^{13}CH_4$ over $Mo_2{}^{12}C$ while ramping from 100°C to 800°C at 25°C per minute, taking samples at 5 points during the ramp and analyzing with a mass spectrometer. Their interpretation of their measurements indicated that, above 550°C, a large portion of the effluent methane was $^{12}CH_4$. Their data suggests that 50%-75% of the $^{13}CH_4$ underwent carbon exchange with the carbide carbon in Mo_2C to form $^{12}CH_4$. If true, this result suggests a rapid, facile decomposition and recombination of methane over the Mo_2C catalyst. The results from this study have been used to support the primacy of the redox mechanism for Dry Methane Reforming over Mo_2C,[84] and have been used to support the theory of active carbide carbon participation in methane reforming reactions.[94]

However, we question their interpretation of their reported results. Firstly, their results of $^{12}CH_4$ and $^{13}CH_4$ mole fractions in the effluent reported that the total methane mole fraction in the effluent was 220%, suspicious since, by definition, total mole fraction should be 100%, with any deviation from 100% likely due to experimental error. The evidence of significant carbon exchange between methane and Mo_2C was given by the reported results that the effluent contained ~50% mole fraction $^{13}CH_4$ and ~150% mole fraction $^{12}CH_4$ at temperatures higher than 550°C. Secondly, only masses 16 and 17 were monitored to detect $^{12}CH_4$ and $^{13}CH_4$, respectively. However, the CH_3 fragment (mass 15 for $^{12}CH_3$, mass 16 for $^{13}CH_3$) is a major fragment of methane, giving a signal ~80% of the parent mass signal.[117] This means that the mass 16 signal would not change much between a stream of pure $^{12}CH_4$ and a stream of pure $^{13}CH_4$, complicating efforts to use mass 16 quantitatively for this experiment. While the researchers reported performing calibration curves, the fact that their calculated total mole fraction is 220% suggests experimental error significantly affected their quantitative measurements.

In an attempt to further explore the possibility of carbon exchange between pure methane and Mo_2C, as well as gain some kinetic and mechanistic insights into it, we performed several pulse Steady State Isotopic Transient Kinetic Analysis (SSITKA) experiments with $^{13}CH_4$ and CD_4 over Mo_2C. The SSITKA technique was used due to its ability to measure various kinetic and mechanistic properties of a catalytic system, including number of active surface species, turnover frequency (TOF), and qualitative insights into the reaction mechanism.[10,11] Using the same amount of Alfa Aesar Mo_2C and the same flowrates as LaMont et al, but continuously monitoring additional masses, we find no evidence of carbon exchange between the $^{13}CH_4$ and the Mo_2C, even at 800°C. Our experiments with CD_4 corroborated this result, but also gave evidence for a small degree of methane dissociation and recombination involving a single C-H bond, seen primarily at 800°C (and likely higher temperatures). Additionally, experiments using temperature ramping similar to the LaMont et al. study confirm the lack of carbon exchange, even at 800°C. These results are not consistent with a model involving facile carbon exchange between pure CH_4 and Mo_2C at temperatures exceeding 550°C. Instead, it appears that dissociative methane adsorption involves only one C-H bond, and does not occur to a significant degree even at 800°C. However, these results are not inconsistent with the previously proposed redox mechanism, where the carbide carbon can participate in reactions involving oxidants over Mo_2C. The isotopically labeled studies performed by Shou and Davis,[118] Xiao et al,[76] and Naito et al[131] have given evidence of this phenomenon for the CO hydrogenation, methane partial oxidation, and methane dry reforming reactions, respectively.

5.2: EXPERIMENTAL

The reactor and apparatus for delivering the pulses of isotopically labeled gas have been described in more detail in a separate publication,[14] and a basic schematic of the reactor system can be seen in Figure 5.1. Briefly, a straight quartz tube reactor (7 mm ID) with a restriction in the middle was packed with 0.03g of quartz wool, and 1g of commercial Mo_2C (Alfa Aesar, 99.5% [metals basis], 325 mesh, Lot # C03W025) was placed on top of the quartz wool. The vertical quartz tube reactor was heated by an external furnace (Applied Test Systems, Series 3210 Furnace) controlled by a proportional-integral-derivative (PID) controller. Four gas cylinders feed reactants into the system via electronic mass flow controllers (MFC). The four streams combine into one stream, leading to the quartz reactor tube. In this study, only 3 streams were used: one for 95% CH_4/5% Ar, one for H_2, and one for an inert gas (He or N_2).

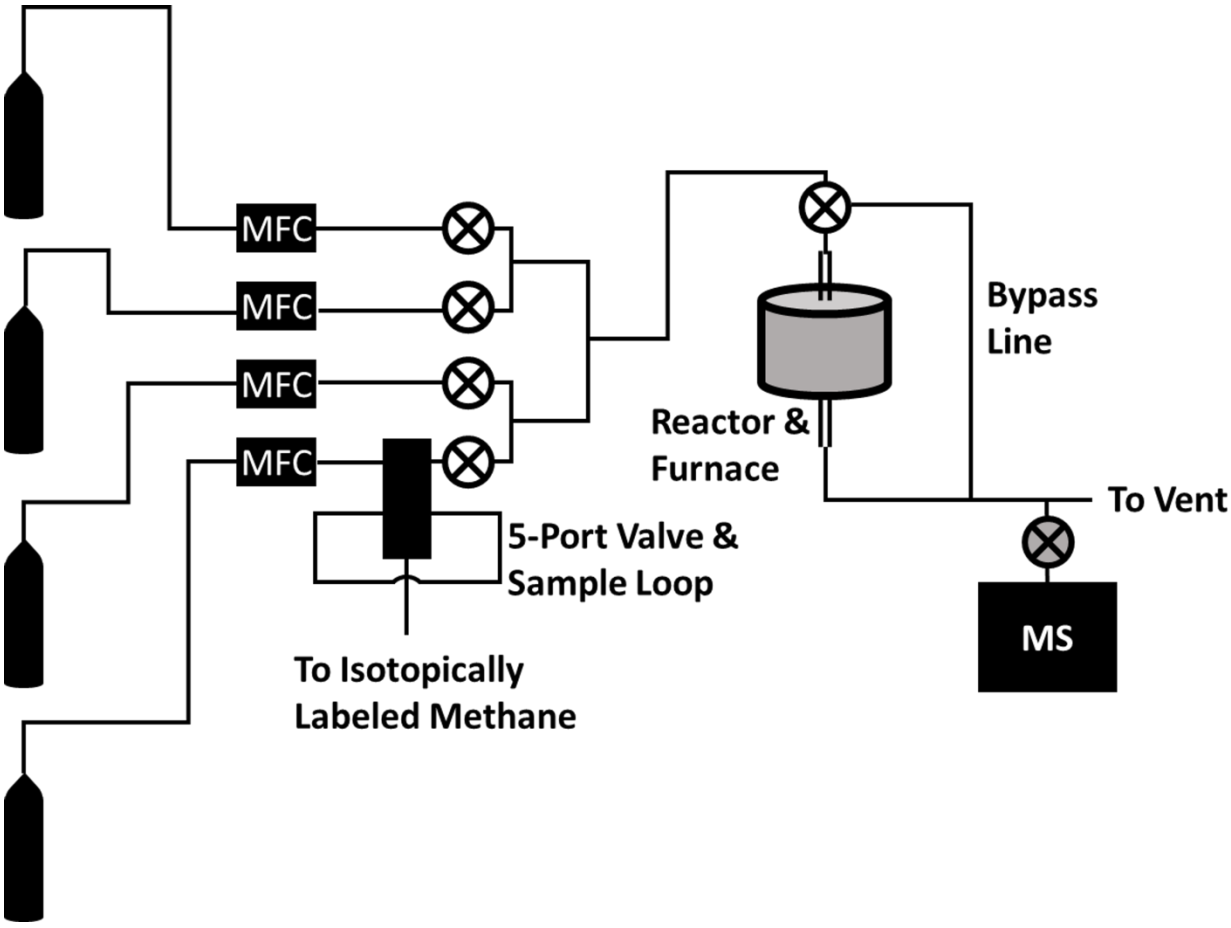

Figure 5.1: Basic schematic of the reactor used. From left to right, gas cylinders containing the reactants connect to mass flow controllers ("MFC") which regulate flow of each reactant. The bottom most gas line represents the methane reactant, which passes through a 5-port valve with a sample loop of isotopically labeled methane. All of the gas lines are then fed to the reactor, and the effluent is analyzed with an on-line mass spectrometer.

Isotopically labeled methane was introduced to the system via a 5-port valve with a 50mL sample loop filled with the isotopically labeled methane. When the 5-port valve switch was flipped, the methane/argon stream was diverted first to the sample loop before being fed to the reactor, similar to the operation of a common GC 6-port valve. This causes a pulse of isotopically labeled methane ($^{13}CH_4$ or CD_4) to be delivered to the reactor, pushed by the diverted 95% CH_4/5% Ar stream. A flow diagram of the 5-port

valve and isotope sample loop used to deliver the pulse of isotopically labeled methane can be seen in Figure C1. The resulting effluent was continuously analyzed with an on-line mass spectrometer. Our on-line mass spectrometer consisted of a 6-way ultra-high vacuum (UHV) cross connecting together an Extorr brand XT100 Residual Gas Analyzer equipped with a quadrupole mass spectrometer operating with an electron bombardment energy of 70eV, a turbomolecular pump backed by a mechanical pump, an ion-gauge, and finally a leak valve connected on-line to the reactor effluent stream for continuous sampling. The dwell time for each mass measured by the Residual Gas Analyzer was 21ms, and each mass was measured approximately once every 1.6 seconds.

95% CH_4/5% Ar was used instead of pure methane in order to use Ar as an inert tracer for the transient studies. In SSITKA experiments and other transient studies, a small amount of inert gas is often incorporated into the non-isotopically labeled reactant in order to determine the gas phase hold-up of the system. This essentially gives the mass transport function of the isotopic pulse through the reactor system without any influence from reaction kinetics. For the isotopically labeled atom(s) in the pulse, any entrance into a kinetic pathway, such as a reaction or dissociative adsorption, causes a time delay in emergence from the reactor compared with the gas phase holdup function. This delay can be detected by normalizing and, if necessary, inverting the mass spectrometer curves so that all curves span from 0 to 1 to 0 during the pulse. The time-delays indicative of entrance into a kinetic pathway manifest as deviations of the reactant and product pulse functions from the inert pulse function. Although much more information about the catalytic system can be extracted from comparing these pulse functions,[10,11] for the purposes of this study it is sufficient to understand that deviation of a species' pulse function from the inert pulse function indicates the presence of a kinetic pathway. In our results, we will present both the mass spectrometer data (smoothed using a 5-point FFT

smoothing function in Origin 9.1 software and scaled using the inert tracer's baseline) as well as these normalized curves.

For the SSITKA experiments, the Mo_2C was heated to 600°C at 10°C/min under 50 standard cubic centimeters per minute (SCCM) flowing inert gas (He for $^{13}CH_4$ experiments, N_2 for CD_4 experiments). The catalyst was subjected to a reductive pretreatment by holding at 600°C for 3 hours under 50 SCCM flowing H_2. We used this pretreatment, since we found the 1 hour H_2 at 600°C pretreatment used by LaMont et al[82] to be insufficient for removing oxygen and adversely affected our results, as will be discussed in more detail below. After the reductive pretreatment, the catalyst was flushed with inert for one hour while cooling to 200°C. 5.5 SCCM of 95% CH_4/5% Ar was then flowed through the system until the system appeared to reach steady state, as determined by the mass spectrometer signals. 5.5 SCCM of 95% CH_4/5% Ar was used in order to be similar to the 5.2 SCCM $^{13}CH_4$ flowrate used by LaMont et al.[82] Once at steady state, a pulse of 50mL $^{13}CH_4$ or CD_4 was injected into the stream, corresponding to a pulse of approximately 9 minutes, and the responses were monitored with the mass spectrometer. One hour after the pulse injection, the reactor was heated to 600°C at 10°C/min, still while flowing 95% CH_4/5% Ar, and allowed to reach steady state. Once at steady state, a 50mL pulse of $^{13}CH_4$ or CD_4 was injected into the stream. Similarly, one hour after the injection at 600°C, the reactor was heated to 800°C at 10°C/min, and allowed to reach steady state before injecting a 50mL pulse of $^{13}CH_4$ or CD_4. One hour after the pulse injection, the reactor was cooled in a stream of inert. A control experiment was performed for each isotopically labeled methane species by injecting a pulse while flowing 5.5 SCCM of 95% CH_4/5% Ar through the catalyst at room temperature.

A second set of experiments was performed in order to more closely resemble LaMont et al's experiment, where the Mo_2C was pretreated with 1 hour of H_2, cooled to

~100°C, then heated to 800°C at 25°C/min while flowing 5.3 SCCM $^{13}CH_4$. In our experiments, the Mo_2C was heated to 600°C in 50 SCCM inert, subjected to a 3 hour, 50 SCCM H_2 pretreatment, then cooled to 200°C in 50 SCCM inert, similar to the SSITKA experiments. Once at 200°C, 18 SCCM inert (He for $^{13}CH_4$ experiments, N_2 for CD_4 experiments) and 2 SCCM 95% CH_4/5% Ar was flowed over the Mo_2C until steady state was achieved. Then, a 50mL pulse of $^{13}CH_4$ or CD_4 was injected, and the temperature was ramped from 200°C to 800°C at 25°C/min, corresponding to a pulse of approximately 25 minutes. Our flowrates and ramp timing were chosen so that the entirety of the ramp occurred during the pulse of isotopically labeled methane.

Finally, the commercial Mo_2C was characterized by XRD and BET. XRD was performed with a Rigatu R-Axis SPIDER with a Cu X-ray source operating at 40kV and 40mA, and rotating the sample at 10 degrees/sec for 10 minutes. BET surface area analysis was performed using a Quantachrome Instruments NOVA 2000 high-speed surface area BET analyzer at a temperature of 77 K. The data was analyzed by Quantachrome Autosorb1 software, using multipoint BET analysis from $P/P_0 = 0.1$ to 0.3 and achieving a correlation coefficient of 0.9999 and a C value of 43.

5.3: Results and Discussion

5.3.1: Catalyst Characterization

The XRD spectrum of the Alfa Aesar commercial Mo_2C is shown in Figure C2 along with the reference spectra for Mo_2C. This spectrum confirms the sample identity to be Mo_2C without any measurable crystalline oxide phase. In addition, the specific surface area of the commercial Mo_2C was measured to be 0.336 m^2/g. Both of these are in agreement with the LaMont et al.[82] study, which found their catalyst to be pure Mo_2C, with a specific surface area of 0.36 m^2/g.

5.3.2: Pulse SSITKA Experiments

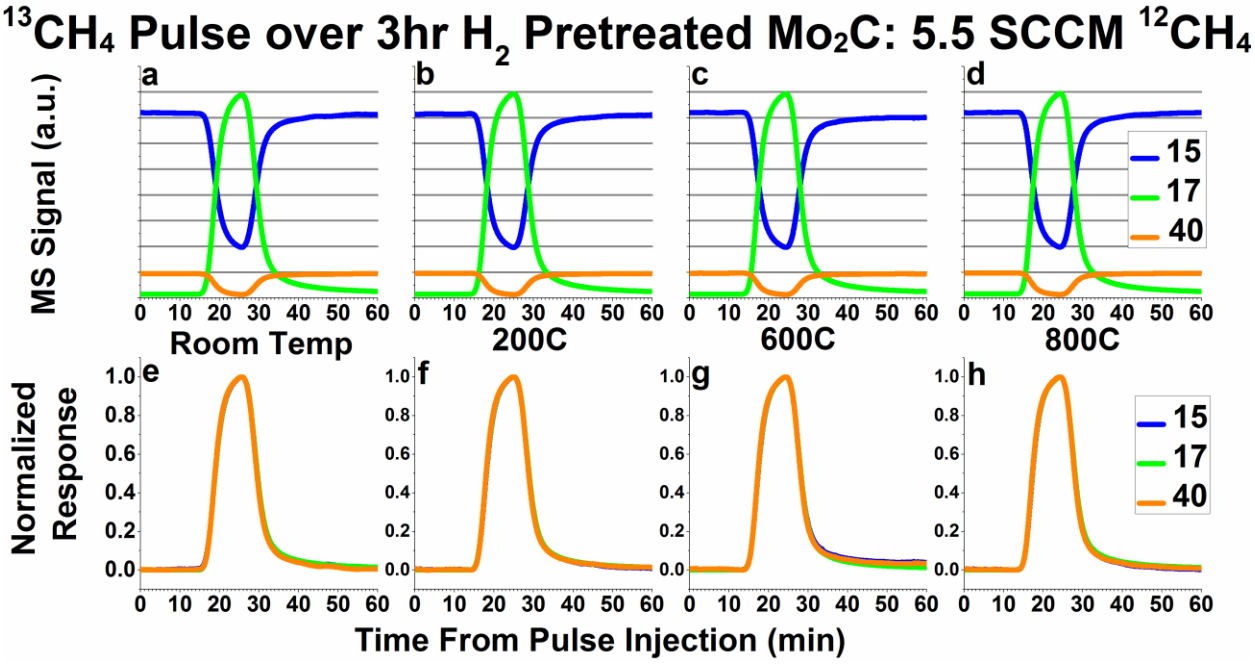

Figure 5.2: Raw mass spectrometry signals (a-d) and normalized responses (e-h) of masses 15 (representing $^{12}CH_4$), 17 (representing $^{13}CH_4$), and 40 (representing Ar inert tracer) for $^{13}CH_4$ pulses while flowing 5.5 SCCM 95% CH_4/5% Ar over Mo_2C at room temperature (a & e), 200°C (b & f), 600°C (c & g), and 800°C (d & h). In Figures 5.2e-5.2h, mass 15 has been inverted in addition to normalized, in order to overlay the pulse response functions. Pretreatment was 50 SCCM flowing H_2 at 600°C for 3 hours.

In order to probe the possibility of carbon exchange between CH_4 and Mo_2C, we first performed 50mL $^{13}CH_4$ pulses while flowing 5.5 SCCM 95% CH_4/5% Ar over Mo_2C. Figure 5.2 shows the mass spectrometry signals (Figures 5.2a-5.2d), and normalized transient responses (Figures 5.2e-5.2h) for these pulses as performed at room temperature, 200°C, 600°C, and 800°C, respectively. Figures 5.2a-5.2d depict the mass spectrometry signals for masses 15, 17, and 40 for all four conditions tested (Room Temperature, 200°C, 600°C, and 800°C). Mass 40 corresponds to the Ar tracer and mass

17 corresponds to $^{13}CH_4$. Mass 15 was chosen as the best representative for $^{12}CH_4$, since it is a major fragment of $^{12}CH_4$ (i.e. $^{12}CH_3$, ~80% of parent mass signal) but a much smaller fragment of $^{13}CH_4$ (i.e. $^{13}CH_2$, ~23% of parent mass signal), corresponding to the most significant change in signal during the $^{13}CH_4$ pulse.[117] If carbon exchange is occurring between methane and Mo_2C, the $^{13}CH_4$ (represented by mass 17) signal should reach a lower maximum and the $^{12}CH_4$ (represented by mass 15) signal should reach a higher minimum than is observed at room temperature, due to ^{13}C incorporation into the bulk and formation of $^{12}CH_4$ from the Mo_2C. However, as can be seen in Figures 5.2a-5.2d, the relative magnitude of all masses are extremely consistent across all temperatures, even at 600°C and 800°C, where carbon exchange has been postulated to occur.[82] While this does not disprove the possibility of a very small degree of carbon exchange between methane and Mo_2C, it casts serious doubt on the assertion that a significant amount of methane in the stream undergoes carbon exchange with Mo_2C, and certainly not the 50%-75% as suggested previously.[82]

In order to probe for any measurable kinetic steps for carbon exchange, the normalized transient response curves of masses 15, 17, and 40 during the $^{13}CH_4$ pulses at the four temperatures (Room Temperature, 200°C, 600°C, and 800°C) are plotted in Figures 5.2e-5.2h. In these plots, the curves of masses 15 and 17 line up almost perfectly behind the Ar inert tracer curve. The lack of any noticeable deviations from the inert tracer during the pulse experiments suggest that there is no kinetic step, giving more evidence against carbon exchange occurring between methane and the molybdenum carbide. While Figures 5.2e-5.2h depict only masses 15 and 17, we monitored all possible methane fragments (masses 12-17). As can be seen in Figures C3e-C3h, the pattern seen with masses 15 and 17 is consistent with all the mass fragments measured.

Figures C3a-C3d depict the same plots as Figures 5.2a-5.2d, but with the addition of mass 16 to demonstrate that the mass 16 curve does not decrease very much during the $^{13}CH_4$ pulse. In addition, the normalized response curves in Figures C3e-SCh show that the baseline for mass 16 does not appear as steady as the rest of the masses monitored. This somewhat unstable baseline, combined with the small change in signal for mass 16 during the pulse, demonstrates the potential risk in using mass 16 to quantify $^{12}CH_4$ versus $^{13}CH_4$.

In order to further study the possible dissociation and recombination mechanism of methane over Mo_2C, the same transient experiments discussed above involving $^{13}CH_4$ were performed with CD_4. Carbon exchange between methane and the carbide support would inherently require full dissociation of the four carbon-hydrogen/deuterium bonds, and then combination of four hydrogen/deuterium atoms with a carbon atom from the support. If this mechanism is correct, one would expect to see a mixture of CH_4 (16), CH_3D (17), CH_2D_2 (18), CHD_3 (19), and CD_4 (20), with the distribution determined by the relative coverages of H and D atoms and the results of any kinetic isotope effect. We would expect a mixture of CH_3D (17), CD_2H_2 (18), and CH_3D (19) even if the dissociation/recombination mechanism involved the breaking and reforming of 2 or more carbon-hydrogen/deuterium bonds on the methane. Alternatively, if only one methane-hydrogen/deuterium bond was broken and reformed in the mechanism, only CH_4 (16), CH_3D (17), CHD_3 (19), and CD_4 (20) should appear in any significant amount.

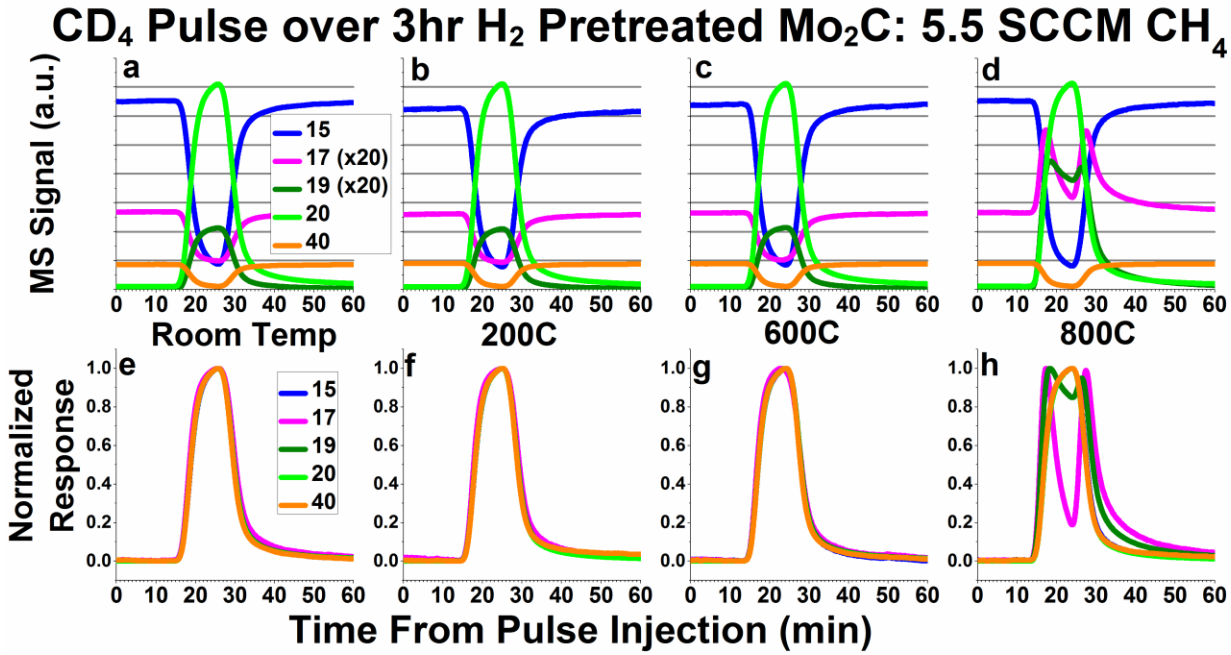

Figure 5.3: Mass Spectrometry signals (a-d) and normalized responses (e-h) of masses 15 (representative of CH_4), 17 (CH_3D), 19 (CD_3H), 20 (CD_4) and 40 (Ar inert tracer) for CD_4 pulses while flowing 5.5 SCCM 95% CH_4/5% Ar over Mo_2C in the bypass (a & e), at 200°C (b & f), at 600°C (c & g), and at 800°C (d & h). In Figures 5.3a-5.3d, masses 17 and 19 have been multiplied by 20 in order to display them on the same plot as masses 15, 20, and 40. In Figures 5.3e-5.3g, masses 15 and 17 have been inverted in addition to normalized in order to overlay the pulse response functions. In Figure 5.2h, only masses 15 has been inverted.

Figure 5.3a-5.3d shows the raw signals of 15, 17, 19, 20, and 40 during the CD_4 pulse experiements at room temperature, 200°C, 600°C, and 800°C, respectively. Mass 15, corresponding primarily to a CH_3 fragment, represents CH_4, since mass 16 is a major fragment of CD_4. Mass 17 represents CH_3D, mass 19 represents CD_3H, mass 20 represents CD_4, and mass 40 represents the inert Ar tracer. In Figures 5.3a-5.3d, the signals for masses 17 and 19 have all been multiplied 20x in order to depict them on the same plot as masses 20 and 40. In the room temperature plot (Figure 5.3a), we can see an

increase in 19 during the pulse, since there are some CD_3H impurities in the CD_4. Similarly, we see a decrease in mass 17 during the pulse, since there is some naturally occurring CH_3D and $^{13}CH_4$ in the CH_4 reactant. As can be seen in Figures 5.3b and 5.3c, the plots for 200°C and 600°C appear similar to room temperature, giving no indication of methane dissociation and recombination. However, at 800°C, we see the appearance of peaks in mass 17 and mass 19. The presence of these peaks in mass 17 (CH_3D) and 19 (CD_3H) indicate the presence of a small amount of dissociative methane adsorption accompanied by recombinative desorption. This dissociation is small enough that there is no noticeable difference in the mass 15 (representing CH_4) and mass 20 (representing CD_4) signals between the pulse performed at 800°C (Figure 5.3d), and the rest of the temperatures (Figures 5.3a-5.3c).

As mentioned above, the mechanism involving carbon exchange between methane and Mo_2C would inherently produce CD_2H_2, which has a mass of 18, in addition to CH_3D and CD_3H. However, mass 18 is a major fragment of CD_4, requiring a signal subtraction of 0.78*(mass 20 signal) in order to properly interpret the data. Plots similar to Figure 5.3a-5.3d, but including the corrected mass 18 signal, can be found in Figure C4a-C4d. This correction is not perfect, however, as can be seen in the room temperature plot, where mass 18 should theoretically be 0 in the whole plot. While there are features in mass 18 at 800°C that appear similar to the peaks in masses 17 and 19 at 800°C (Figure C4d), it is unclear whether this actually corresponds to the CD_2H_2 species. The features could be a result of imperfect signal subtraction, similar to the effect seen in the 200°C plot. Since 18 would represent the CD_3 fragment of CD_3H, it is also possible that some or all of the features in the mass 18 signal could be attributed to CD_3H fragmentation. Even if the entire signal for mass 18 in Figure C4d was attributable to CD_2H_2, the peaks in mass 18 are less than the ones in mass 17 or mass 19. This suggests

that, if any CH_2D_2 is produced, it is significantly less than the CH_3D and CD_3H produced at 800°C.

The normalized response curves for masses 15, 17, 19, 20 and 40 are depicted in Figures 5.3e-5.3h. Similar plots containing all masses monitored (masses 12-20 and 40) can be seen in Figure C4e-C4h. In the Room Temperature, 200°C, and 600°C plots, no noticeable deviations from the Ar tracer (mass 40) can be seen. However, at 800°C (Figure 5.3h), the peaks in mass 17 and 19 are clearly detectable. From these plots, we can see that the peaks in mass 17 and 19 occur when both CH_4 and CD_4 are in the stream, suggesting that this dissociation/recombination mechanism occurs relatively rapidly. Overall, the results from these CD_4 pulse experiments do not provide evidence for significant and complete methane dissociation and recombination, as would be required for carbon exchange between methane and Mo_2C. Further, the fact that the small degree of methane dissociative adsorption that can be detected at 800°C results primarily in CH_3D and CD_3H species indicates that this dissociative adsorption involves the breaking and reforming of just one carbon-hydrogen/deuterium bond.

5.3.3: Ramp Experiments

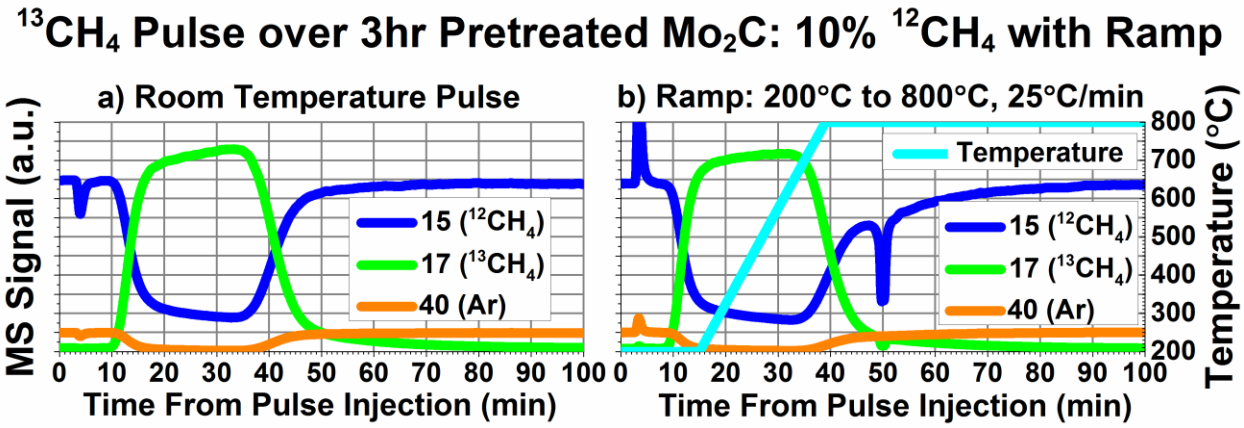

Figure 5.4: Raw mass spectrometry curves of masses 15 (representing $^{12}CH_4$), 17 (representing $^{13}CH_4$), and 40 (representing Ar inert tracer for $^{13}CH_4$ pulses delivered while flowing 18 SCCM He, and 2 SCCM 95% CH_4/5% Ar after 3 hours of H_2 pretreatment at 600°C. a) Pulse performed at room temperature; b) Pulse performed while ramping from 200°C to 800°C at 25°C/min, as indicated by the cyan temperature curve overlaid on the mass spectrometer curves.

In order to more closely match the experimental conditions (i.e. exposure time and temperature profile) used in the LaMont et al. study, pulse experiments were performed while flowing 18 SCCM inert and 2 SCCM 95% CH_4/5% Ar and ramping from 200°C to 800°C at 25°C/min. Figure 5.4 depicts the results of $^{13}CH_4$ pulses at room temperature (Figure 5.4a), and while ramping from 200°C to 800°C at 25°C/min (Figure 5.4b). Figure 5.4 compares mass 15 (best mass for $^{12}CH_4$), 17 ($^{13}CH_4$), and 40 (the inert Ar tracer). It should be noted that the spikes seen in the curves around minute 4 are due to imperfect matching of the pressure of the 95% CH_4/5% Ar reactant stream and the pressure in the sample loop filled with isotopically labeled methane, causing a temporary spike of extra methane or extra inert. Based on these results and other, unpublished results, we have not found this spike to affect our results. During the ramp, the curves for

$^{13}CH_4$ and $^{12}CH_4$ appear identical to the room temperature pulse curves. If significant and facile carbon exchange occurred at temperatures above 550°C, there should have been a significant decrease in the mass 17 and significant increase in the mass 15 curves around the middle of the pulse function. Even at 800°C, no signs of carbon exchange can be seen.

There is an interesting feature of note at minute 50 in Figure 5.4b, where there is a significant decrease in both mass 17 and 15. Since carbon exchange would result in one of these masses increasing and the other decreasing, this feature is likely the result of some degree of oxidation of the methane. Figure C5 depicts more masses measured during the same experiment described in Figure 5.4. As can be seen in Figure C5d, the decrease in mass 15 and 17 is accompanied by increases in 28, 29, and a small amount of 18. This is indicative of some kind of oxygenated species being reduced by the methane. During our study, we found evidence of a couple different types of oxygenated species present in the Mo_2C. The first type belongs to oxygen that can be removed with the 600°C H_2 pretreatment. As stated earlier, we found a one hour pretreatment to be insufficient for removing this type of oxygen species. Figure C6 depicts the same ramp experiment as seen in Figure 5.4, but with only 1 hour of hydrogen pretreatment, showing a significant decrease in masses 17 and 15 during the ramp, accompanied by increases in masses 28, 29, and 18. Since we do not see an increase in mass 15 corresponding to the decrease in 17, as well as seeing features for CO and H_2O, this phenomena is likely due to methane consumption, not carbon exchange between the methane and Mo_2C. This finding is supported by the additional H_2O that is removed from the Mo_2C during the second and third hour of the H_2 pretreatment, as can be seen in Figure C7.

The spikes seen at minute 50 seem to represent a different type of oxygenated species than that removed by the H_2 pretreatment. We see consumption of methane in the

SSITKA studies as well, during the ramp to 600°C and hold at 600°C until steady state was achieved, as can be seen in Figure C8. Since this species is reduced at 600°C with methane, but was not reduced during the H_2 pretreatment at 600°C, this species likely requires methane for reduction. We see a smaller, similar phenomenon during the ramp to 800°C, as can be seen in Figure C9, but we cannot say whether or not this species required methane for reduction, or if a H_2 pretreatment at a higher temperature would remove it. A SSITKA experiment, identical to that described in Figure 5.2 was also performed with only 1 hour of H_2 pretreatment at 600°C, and we found no difference in the results, as can be seen in Figure C10.

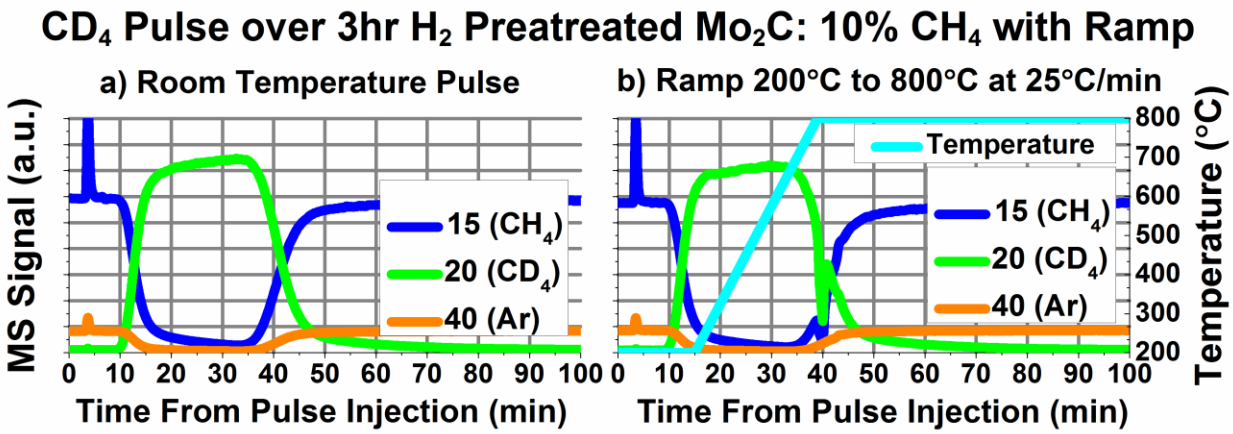

Figure 5.5: Raw mass spectrometry curves of masses 15 (representing CH_4), 20 (representing CD_4), and 40 (representing Ar inert tracer) for CD_4 pulses delivered while flowing 18 SCCM He, and 2 SCCM 95% CH_4/5% Ar after 3 hours of H_2 pretreatment at 600°C. a) Pulse performed at room temperature; b) Pulse performed while ramping from 200°C to 800°C at 25°C/min, as indicated by the cyan temperature curve overlaid on the mass spectrometer curves.

We performed a similar ramping experiment with a CD_4 pulse, and the results are depicted in Figure 5.5. The ramping pulse (Figure 5.5b) generally appears similar to the

room temperature pulse (Figure 5.5a), giving no indication of significant methane dissociation during the temperature ramp. There seems to be a slight dip in mass 20 at minute 22, which is likely due to the same oxidation phenomenon seen in the $^{13}CH_4$ experiments. Figure C11 depicts more of the masses measured during the pulse experiment depicted in Figure 5.5. As can be seen in Figure C11d, the dip in mass 20 is accompanied by a peak in 44, likely indicative of the reduction of some oxygenated species. In addition, there may be a slight decrease in 20 starting at minute 30, accompanied by slight increases in masses 17, 19, and 44, before a spike of methane consumption at minute 40. In this experiment, it is difficult to determine whether the increases in masses 17 and 19 are due to H_2O and HDO production or dissociative methane adsorption to form CH_3D and CD_3H. What is clear, however, is that we do not see evidence of significant, complete, methane dissociation and recombination, as would be required for methane-carbide carbon exchange, especially not on the order of 50%-75%, as has been previously claimed.[82]

5.4: CONCLUSIONS

Both the SSITKA and ramping $^{13}CH_4$ exchange studies do not exhibit significant carbon exchange between methane and the Mo_2C carbide carbon, in contradiction to previous literature reports suggesting 50%-75% of the methane stream undergoes carbon exchange at temperatures above 550°C with the conditions used in this study.[82] Further, no kinetic step could be measured at any condition or temperature tested using the SSITKA technique. This suggests that carbon exchange between a stream of methane and Mo_2C, if any does occur, is extremely small and undetectable with these experiments.

In addition, the CD_4 exchange experiments seem to suggest a different methane adsorption mechanism. The appearance of mass 17 (CH_3D) and 19 (CD_3H) peaks at

800°C in the SSITKA studies, indicates that methane likely does dissociate on Mo_2C at 800°C. However, since little to no amount of mass 18 could be attributed to CD_2H_2, our results suggest that methane adsorption involves the cleavage of only one carbon-hydrogen/deuterium bond to form CH_3 or CD_3 and H or D on the surface. In addition, the extremely small amount of CD_3H and CH_3D formed from the recombination suggests that this dissociation/recombination mechanism is still relatively minor, even at 800°C. This implies that reactions involving methane over Mo_2C require additional species, such as oxidants, to involve the carbide carbon and complete the redox mechanism.

Chapter 6: Conclusions

6.1: Methanol O-H Bond Dissociation and Structure on Au(111)

In Chapter 2, we explored the surface structure of a methane derivative, methanol, on Au(111) in the presence of coadsorbed hydrogen adatoms. The presence of these hydrogen adatoms induced a change in the methanol monolayer, causing a set of surface structures to exist with various surface stabilities. By using combinations of MeOH, MeOD, H_2, and D_2, the origins of the hydrogens/deuterium atoms in the hydrogen and methanol molecules could be determined. Based on these isotopic studies, we were able to determine that methanol O-H bond dissociation and hydrogen exchange with surface hydrogen adatoms occurs at low temperatures (< 120K), since exchange products were found in the methanol multilayers. In addition, the results allowed us to speculate on a reasonable exchange and desorption mechanism for MeOH/H/Au(111).

6.2: Methane Reactions over Molybdenum Carbide Catalysts

Carbide catalysts, particularly molybdenum carbide catalysts, represent an intriguing class of catalysts. While they have demonstrated reactivities similar to noble metal catalysts, their mechanisms appear to operate very differently than traditional catalysts composed of a metal on a metal oxide support. With regard to methane reforming reactions, molybdenum carbide based catalysts seem to balance competing oxidizing and reducing reactions. For methane reforming reactions as well as Fischer-Tropsch reactions, the carbon in molybdenum carbide catalysts even appears to directly participate in the reaction.

In Chapter 3, we demonstrated that Ni/Mo_2C catalysts are able to simultaneously catalyze the Dry Methane Reforming reaction and the Steam Methane Reforming reaction in the same reactor. This process allows a range of syn-gas ratios, 0.9:1 - 3.0:1

H_2:CO, to be produced by tuning the oxidant mixture (CO_2 and H_2O) in the reactant feed stream, potentially reducing significant capital costs if this scheme was used industrially. In addition, the deactivation mechanism observed was intriguing. Notably, the catalyst did not exhibit any evidence of coking, despite running under conditions favorable to coking. Coking is a potentially dangerous phenomenon and responsible for most catalyst deactivation in methane reforming reactions. Conversely, the Ni/Mo_2C catalyst did not show any signs of deactivation until a single, rapid deactivation event that oxidized the Ni/Mo_2C catalyst.

One of the more surprising assertions made in the literature regarding molybdenum carbide was that pure methane could undergo significant, facile carbon exchange with the carbon in the Mo_2C catalyst at temperatures above 550°C. Using the apparatus described in Chapter 4, we were able to challenge and correct this misconception, as described in Chapter 5. By replacing $^{12}CH_4$ with pulses of $^{13}CH_4$ at various temperatures, we were able to demonstrate that significant, facile carbon exchange did not occur between methane and Mo_2C. Further, we were able to offer a different dissociation mechanism for methane on Mo_2C, which involved a single C-H bond dissociation at temperatures above 800°C.

6.3: Experiments Using Isotopically Labeled species

As illustrated in Chapters 2 and 5, using isotopically labeled species can give valuable mechanistic insight into catalytic reactions. In addition, various valuable kinetic measurements can be made using the Steady State Isotopic Transient Kinetic Analysis (SSITKA) technique when studying classical catalytic systems. However, the typical methods for performing SSITKA experiments underutilize much of the valuable isotopically labeled gases required. In Chapter 4, we described an apparatus that

improves the gas use efficiency for SSITKA and other pulse-transient experiments. The benefit of this apparatus is apparent in Chapter 5, where we were able to perform ramp experiments similar to the literature study we were trying to replicate, as well as several additional constant-temperature SSITKA experiments. These additional experiments enabled by the Pulse Injection Apparatus allowed a more definitive characterization of the catalytic system, providing the required evidence to give an updated view of methane dissociation over Mo_2C. This apparatus may be used by future researchers to improve the efficiency, accuracy, and precision of these valuable experiments.

6.4: Suggestions for Future Studies

One area that can be immediately pursued based on our work is further study of methane reforming reactions on molybdenum carbide based catalysts. As determined in Chapter 3, molybdenum carbide based catalysts seem to operate differently from the more typical metal/metal oxide type catalysts, bestowing benefits like coke-resistance during methane reforming reactions as well as stability at high reaction temperatures. Nickel has proved to be a particularly promising metal to incorporate into Mo_2C to improve the activity for methane reforming reactions and stability for the catalyst overall. One valuable question still left unanswered for Ni/Mo_2C is the role that the Ni and Mo_2C portions of the catalyst perform. Do they operate relatively independently, with Ni primarily catalyzing the methane dissociation step, and Mo_2C primarily catalyzing the oxidation step? Or, do they change the structure or electronics of the material, and operate in a more cooperative mechanism? These are valuable next questions to answer with future studies.

Secondly, the mechanisms and kinetics of methane reforming reactions over molybdenum carbide based catalysts are still poorly understood. The Pulse Injection

Apparatus described in Chapter 4 would be a valuable tool for gaining these insights. Some preliminary data from SSITKA experiments of the dry methane reforming reaction over Mo_2C have demonstrated an ability to measure a kinetic step in methane reacting to form CO. In addition, these preliminary experiments have also suggested that ^{13}C from a $^{13}CH_4$ pulse can end up as $^{13}CO_2$, giving some insight into the reaction mechanisms. A thorough study using SSITKA pulse experiments may be able to give a more complete mechanistic picture of methane reforming reactions over Mo_2C, including some measurements of the kinetic step timescales. Further, molybdenum carbide based catalysts, such as the Ni/Mo_2C described in Chapter 3, could also be studied, potentially giving insight into the mechanistic reasons for the deactivation and reactivity differences to Mo_2C.

More broadly, the design of the Pulse Injection Apparatus represents a significant improvement to valuable SSITKA experiments. For both the Mullins lab and other researchers who utilize this apparatus, SSITKA experiments will be less expensive, opening up possibilities for new or more extensive investigations into catalytic reactions. For example, researchers may find it feasible to perform the same SSITKA pulse experiment at multiple reaction temperatures. The kinetic measurements made at each of these conditions could provide insight into the rate constants of particular elementary reactions, competing mechanistic pathways, or other kinetic aspects of the reaction system. Another possibility could be performing the same SSITKA experiment over a range of catalysts, such as with different particle sizes or other treatments. These experiments could elucidate where the active reactive species occur, and ways to optimize a catalyst for the most desired outcome.

Mechanistic insights into catalytic reactions have proved valuable for the continuing development and optimization of catalysts and conditions. With the rise of

methane as an energy and chemical feedstock source, understanding the reactions involved in transporting and converting methane can lead to efficiency improvements in the catalytic reactions responsible for these conversions. More broadly, understanding the mechanisms and kinetics involved in catalytic reactions allow better design of catalysts, leading to more efficiency in the production of the everyday chemicals we as humans use. These efficiency improvements lead to a lower footprint our species has on the planet and brings us closer to a truly sustainable existence. Understanding and improving catalysts will be a crucial aspect in attaining these goals.

Appendix A: Supporting Information for Methanol O-H Bond Dissociation on H-Precovered Gold Originating from a Structure with a Wide Range of Surface Stability

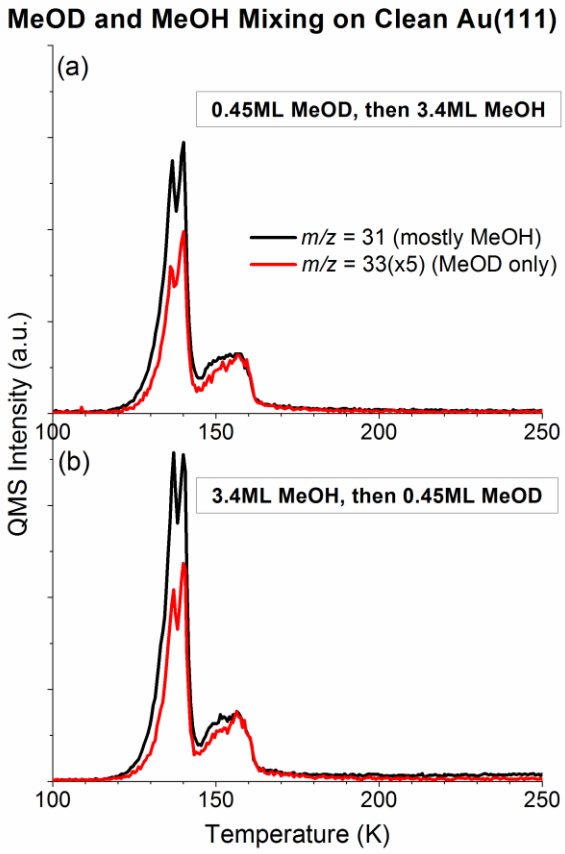

Figure A1: QMS spectra of m/z = 31, a mass fragment of both MeOH and MeOD, and m/z = 33, a mass fragment of MeOD only, for MeOD and MeOH coadsorbed on clean Au(111) surface. a) 0.45ML MeOD deposited on clean Au(111), followed by 3.4ML MeOH. b) 3.4ML MeOH deposited on clean Au(111), followed by 0.45ML MeOD.

In Figure A1a, 0.45ML MeOD is deposited on clean Au(111), followed by 3.4ML deposition of MeOH. The *m/z* = 33, indicative of MeOD only, mimics the shape of *m/z* =

31, a mass fragment of both MeOH and MeOD, indicating MeOD has thoroughly mixed with the MeOH. Had no mixing occurred, the *m/z* = 33 spectra should have only displayed a monolayer feature, at 155 K, and no multilayer features, at 136 K and 139 K. Similarly, in Figure A1b, 3.4ML MeOH is deposited on clean Au(111), followed by 0.45ML MeOD. The *m/z* = 33 spectra also mimics the *m/z* = 31 spectra, indicating thorough mixing. Had no mixing occurred, the *m/z* = 33 spectra should have only displayed a multilayer feature, at 136 K and/or 139 K, and no monolayer feature, at 155 K.

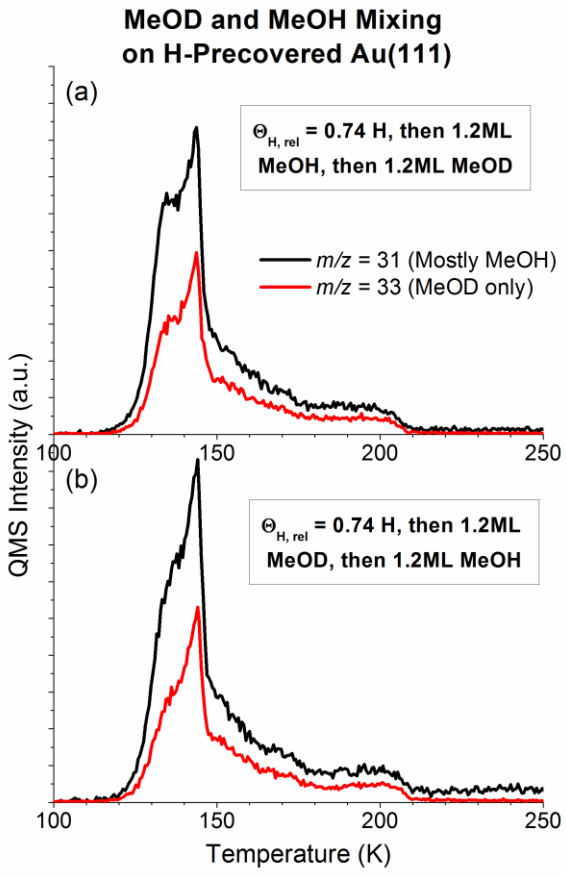

Figure A2: QMS spectra of *m/z* = 31, a mass fragment of both MeOH and MeOD, and *m/z* = 33, a mass fragment of MeOD only, for 1.2ML MeOD and 1.2ML MeOH coadsorbed on $\Theta_{H,rel}$ = 0.74 H-precovered Au(111) surface. a) MeOH deposited on H-precovered Au(111) surface, followed by MeOD deposition. b) MeOD deposited on H-precovered Au(111) surface, followed by MeOH deposition.

Figure A2 displays the *m/z* = 31, mass fragment for both MeOH and MeOD, and *m/z* = 33, mass fragment for MeOD only, for 1.2ML MeOD coadsorbed with 1.2ML MeOH on an 0.74ML H-precovered surface. In Figure A2a, MeOH is deposited before MeOD, and in Figure A2b, MeOD is deposited before MeOH. The *m/z* = 31 and *m/z* = 33

spectra match for both deposition orders, indicating thorough mixing of MeOD and MeOH on an H-precovered surface.

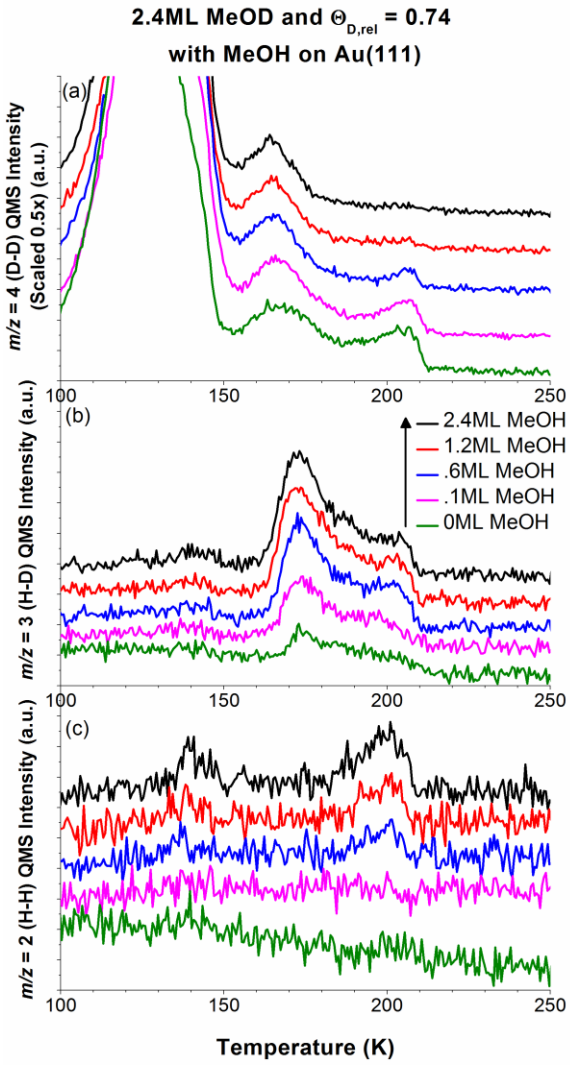

Figure A3: 2.4ML deuterated methanol (MeOD) coadsorbed with various amounts of MeOH on $\Theta_{D,rel}$ = 0.74 D-precovered surface to test MeOH's inhibiting effect on MeOD's ability to hydrogen exchange. MeOD:MeOH ratios given by legend. a) *m/z* = 4, indicative of D-D desorption b) *m/z* = 3, indicative of H-D desorption, c) *m/z* = 2, indicative of H-D desorption

Figure A3 demonstrates the inhibiting effect MeOH has on the ability of MeOD to hydrogen exchange on a deuterium covered surface. This data indicates that this phenomenon is due to a difference between MeOH and MeOD, and is independent of whether MeOH and MeOD are coadsorbed with H or D.

The remaining figures demonstrate that ethanol and hydrogen exhibit phenomena similar to that displayed by methanol and hydrogen on Au(111). Figures C4-C11 correspond to Figures 2.1-2.6, C1, and C2, respectively. Please refer to the main article for descriptions of these comparisons.

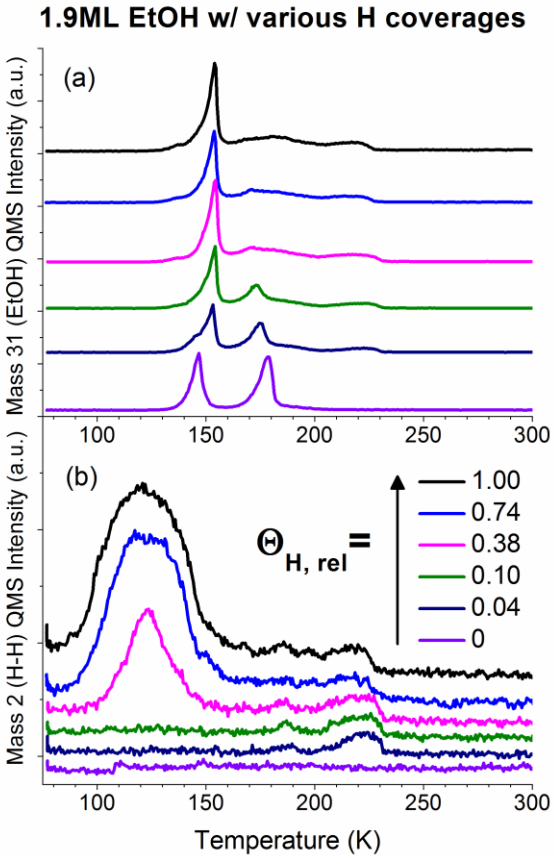

Figure A4: QMS spectra of EtOH/H/Au(111). 1.9 monolayers of ethanol were coadsorbed with various coverages of hydrogen, as indicated by the legend. a) *m*/z = 31, indicative of ethanol; b) *m*/z = 2, indicative of hydrogen. All species were adsorbed at 77 K. The heating rate was 1 K/s.

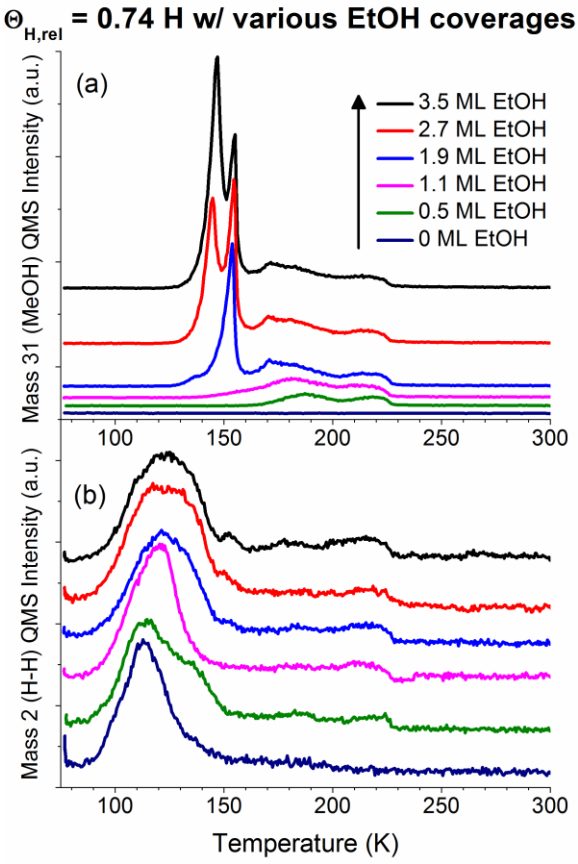

Figure A5: QMS spectra of EtOH/H/Au(111). $\Theta_{H,rel}$ = 0.74 of hydrogen was coadsorbed with various coverages of ethanol, as indicated by the legend. a) *m*/z = 31, indicative of ethanol; b) *m*/z = 2, indicative of hydrogen. All species were adsorbed at 77 K. The heating rate was 1 K/s.

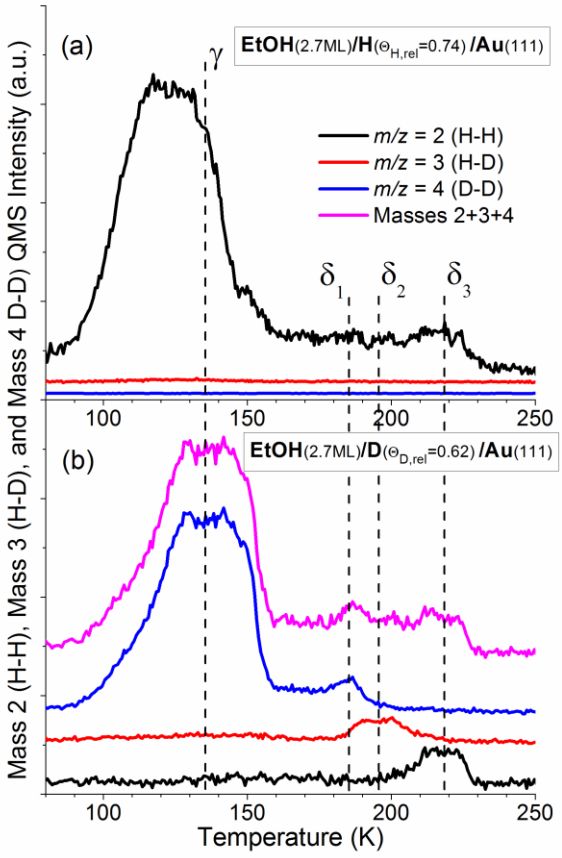

Figure A6: QMS spectra of *m/z* = 2, *m/z* = 3, and *m/z* = 4 for ethanol (EtOH) coadsorbed with hydrogen (H) or deuterium (D). "Masses 2+3+4" is the composite spectra of adding the signal of *m/z* = 2, 3, and 4 together from 3b. a) 2.7 monolayer of EtOH coadsorbed with $\Theta_{H,rel} = 0.74$ of hydrogen (H); b) 2.7 monolayers of EtOH coadsorbed with $\Theta_{D,rel} = 0.62$ of deuterium (D). All species were adsorbed at 77 K. The heating rate was 1 K/s.

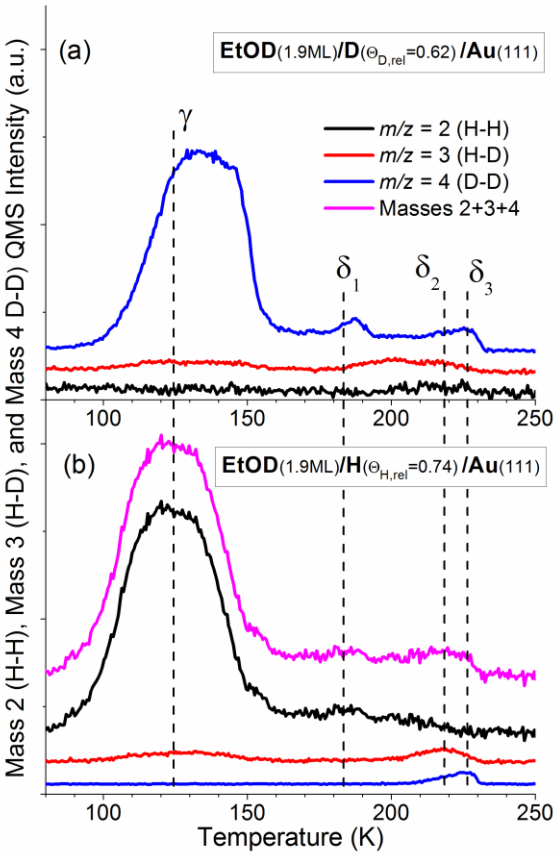

Figure A7: QMS spectra of *m/z* = 2, *m/z* = 3, and *m/z* = 4 for EtOD coadsorbed with deuterium (D) or hydrogen (H). "Masses 2+3+4" is the composite spectra of adding the signals of *m/z* = 2, 3, and 4 together from 4b. a) 1.9 monolayer of deuterated ethanol (CH_3CH_2OD) coadsorbed with $\Theta_{D,rel} = 0.62$ of deuterium; b) 1.9 monolayers of ethanol coadsorbed with $\Theta_{H,rel} = 0.74$ of hydrogen. All species were adsorbed at 77 K. The heating rate was 1 K/s.

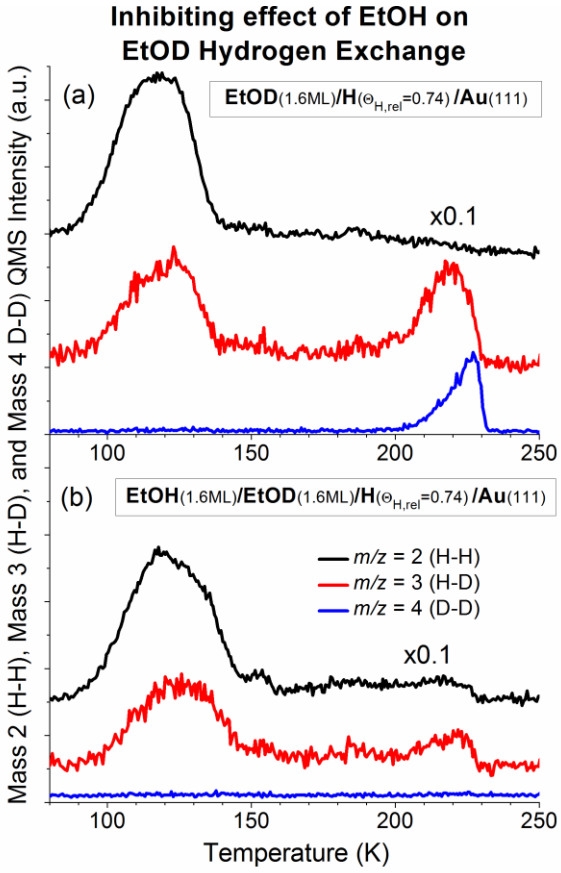

Figure A8: QMS spectra of *m/z* = 2 (*0.1), *m/z* = 3, and *m/z* = 4. a) 1.6 monolayers EtOD on $\Theta_{H,rel}$ = 0.74 hydrogen pre-covered Au(111); b) 1.6 monolayers of EtOD (first reactant adsorbed) coadsorbed with 1.6 monolayers of EtOH (second reactant adsorbed) on $\Theta_{H,rel}$ = 0.74 hydrogen pre-covered Au(111). All species were adsorbed at 77 K. The heating rate was 1 K/s.

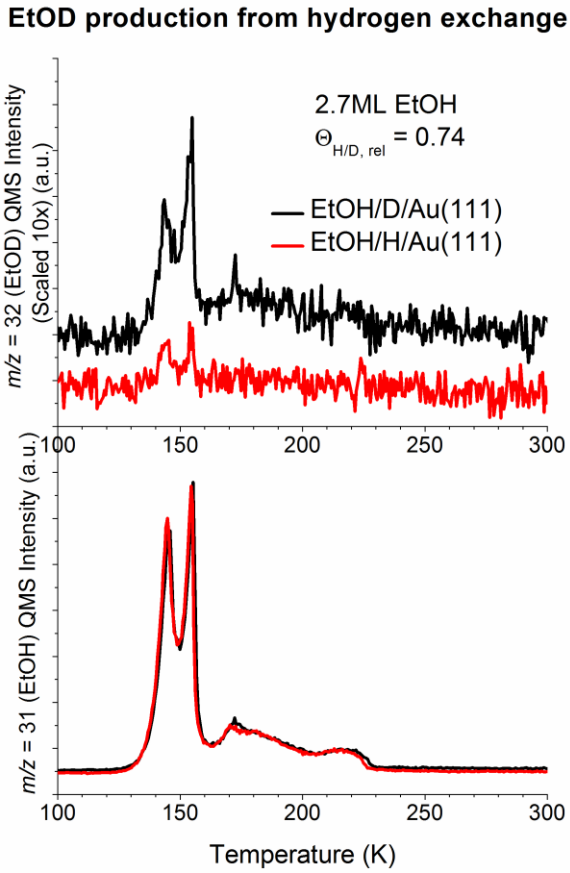

Figure A9: QMS spectra of EtOH (2.7 monolayers)/D ($\Theta_{D,rel}$ = 0.6)/Au(111) (black) and EtOH (2.7 monolayers)/H ($\Theta_{H,rel}$ = 0.74)/Au(111) (red). a) *m/z* = 32, scaled 10x relative to (b), indicative of EtOD. b) *m/z* = 31, indicative of EtOH. All species were adsorbed at 77 K. The heating rate was 1 K/s.

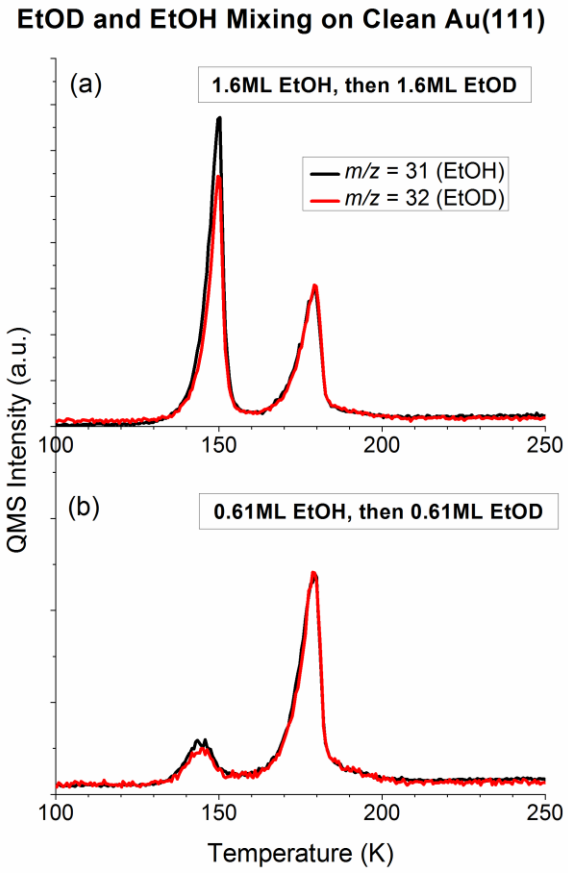

Figure A10: QMS spectra of m/z = 31 and m/z = 32 of EtOH coadsorbed with EtOD on clean Au(111) a) 1.6 monolayers of EtOH, followed by 1.6 monolayers of deuterated ethanol (CH_3CH_2OD) b) 0.61 monolayer of EtOH, followed by 0.61 monolayers of deuterated ethanol (CH_3CH_2OD). All species were adsorbed at 77 K. The heating rate was 1 K/s.

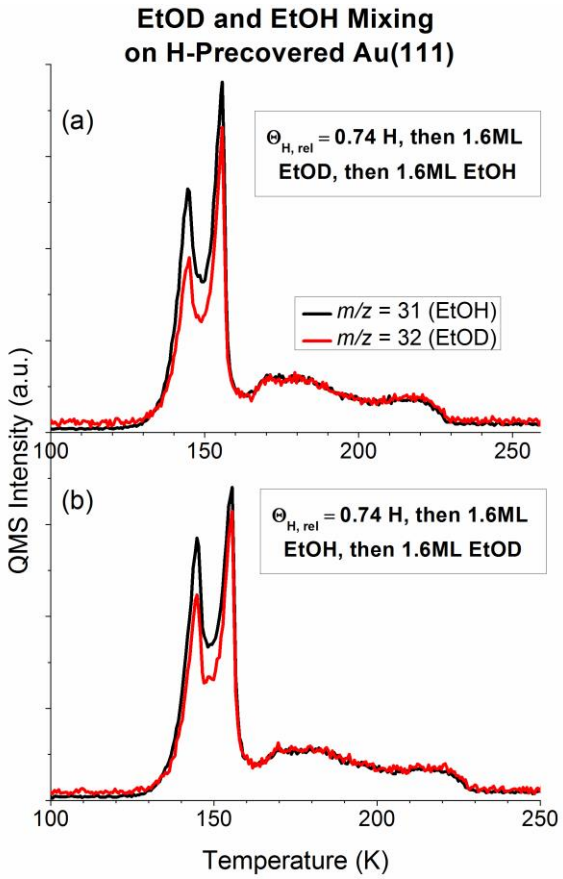

Figure A11: 1.6 monolayers of ethanol coadsorbed with 1.6 monolayers of deuterated ethanol (CH_3CH_2OD) on $\Theta_{H,rel}$ = 0.74 hydrogen pre-covered Au(111) a) EtOD dosed first, then EtOH b) EtOH dosed first, then EtOD. All species were adsorbed at 77 K. The heating rate was 1 K/s.

In Figure A10a, EtOD is present in the monolayer feature, which should be entirely EtOH if no mixing occurs. Similarly, in Figure A10b, EtOH is present in the second layer, which should be entirely EtOD if no mixing occurs. In Figure A11, both plots appear close to identical, despite different adsorption order, indicating close to complete mixing.

Appendix B: Supporting Information for Tunable Syn Gas Ratio via Bireforming Over Coke-Resistant Ni/Mo_2C Catalyst

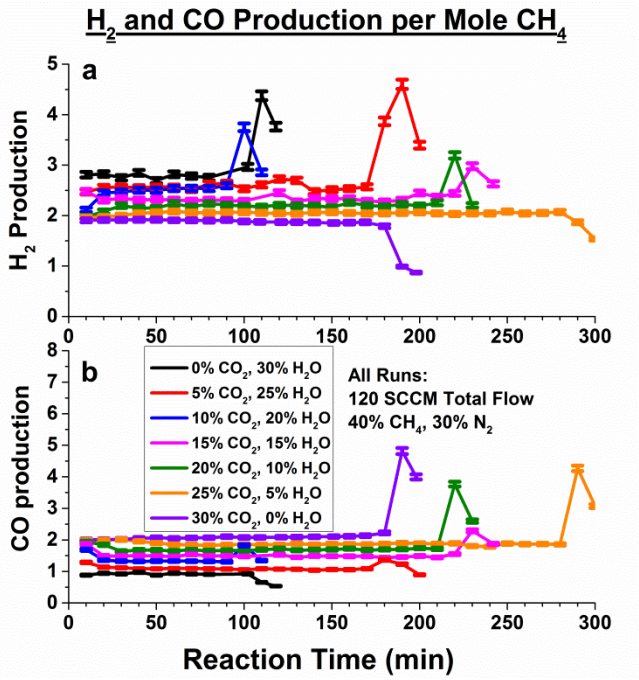

Figure B1: a) Moles of H_2 produced per mole CH_4 reacted; b) Moles CO produced per mole CH_4 reacted. Error bars represent the 95% confidence interval for each measurement.

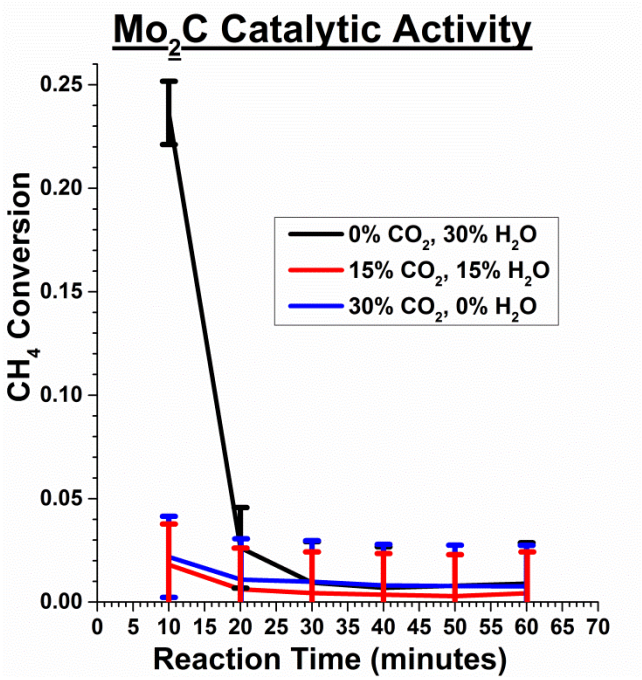

Figure B2: Methane conversion for reforming reaction tests over Mo_2C, demonstrating low catalytic activity compared to Ni/Mo_2C. Error bars represent the 95% confidence interval for each measurement.

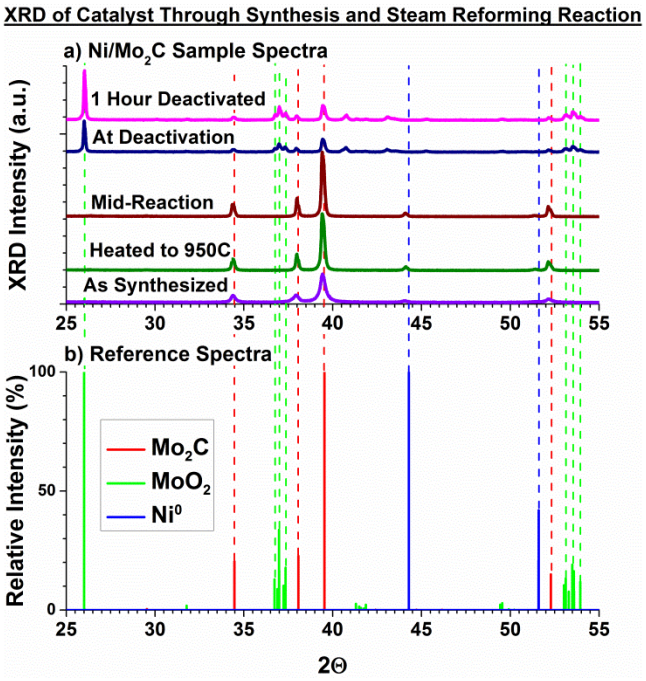

Figure B3: a) XRD of catalyst at various timepoints during synthesis and steam reforming reaction; b) Reference spectra with dashed lines extending into B3a for ease of phase identification.

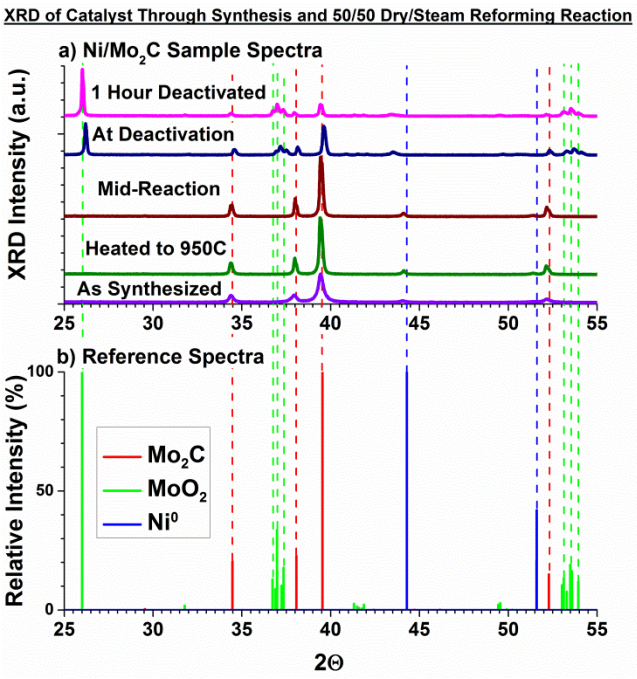

Figure B4: a) XRD of catalyst at various timepoints during synthesis and 15% CO_2/15% H_2O reforming reaction; b) Reference spectra with dashed lines extending into B4a for ease of phase identification.

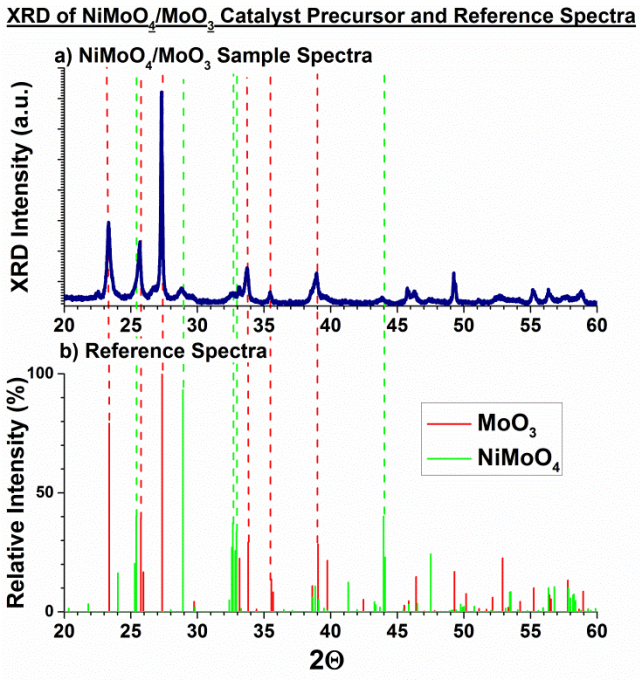

Figure B5: a) XRD of $NiMoO_4/MoO_3$ catalyst precursor; b) Reference spectra of MoO_3 and $NiMoO_4$. Dashed lines included for major peaks for ease of phase identification.

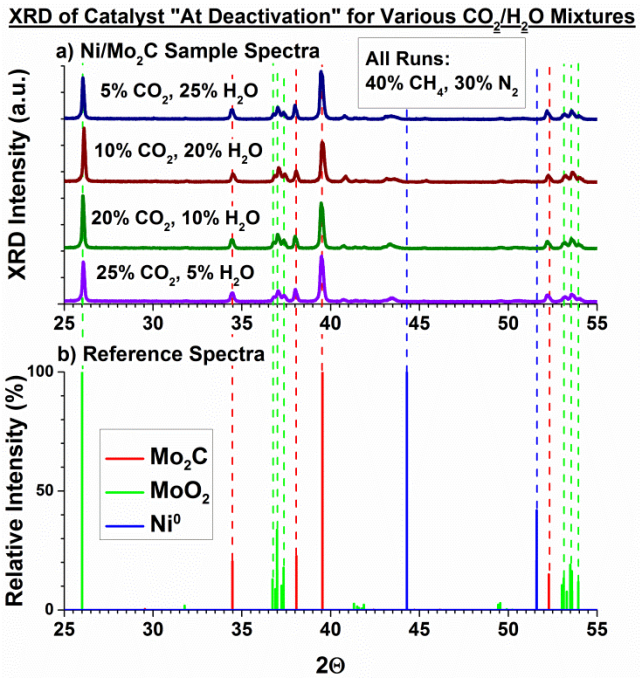

Figure B6: a) XRD of "at deactivation" timepoint samples for various ratios of CO_2:H_2O; b) Reference spectra with dashed lines extending into B6a for ease of phase identification.

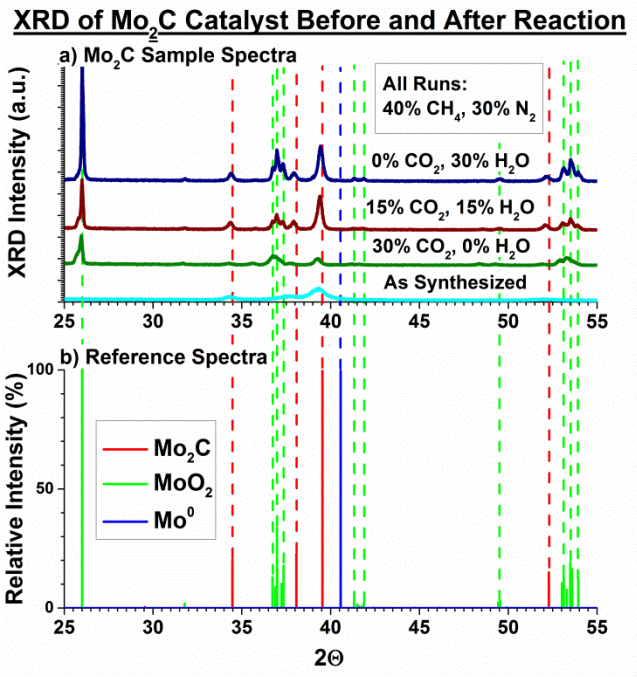

Figure B7: a) XRD of Mo_2C catalyst "as synthesized" and after 1 hour exposure to various dry and steam reforming reaction conditions; b) Reference spectra with dashed lines extending into B7a for ease of phase identification.

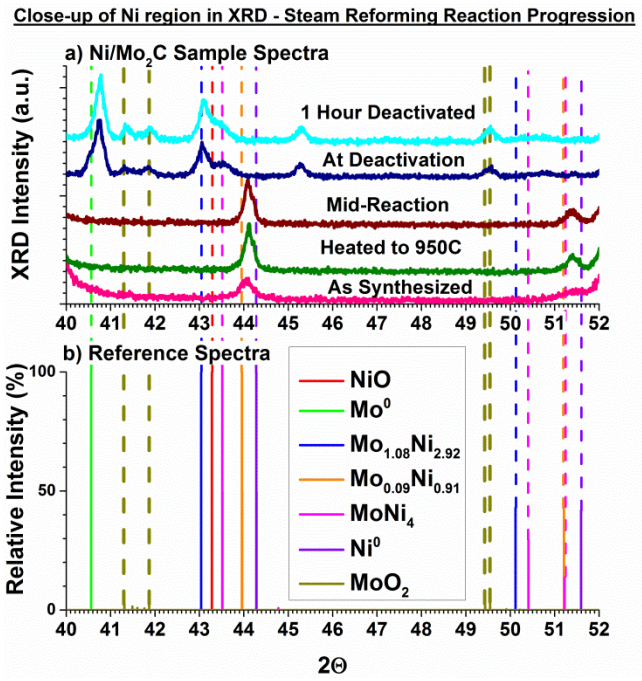

Figure B8: a) Close-up of Ni-region in XRD of catalyst at various timepoints during synthesis and steam reforming reaction; b) Reference spectra with dashed lines extending into B8a for ease of phase identification.

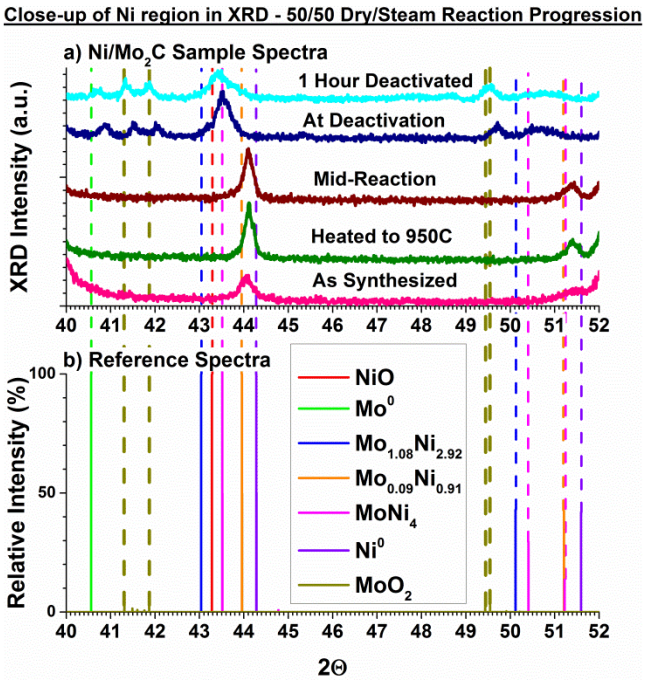

Figure B9: a) Close-up of Ni-region in XRD of catalyst at various timepoints during synthesis and 15% CO_2/15% H_2O reforming reaction; b) Reference spectra with dashed lines extending into B9a for ease of phase identification.

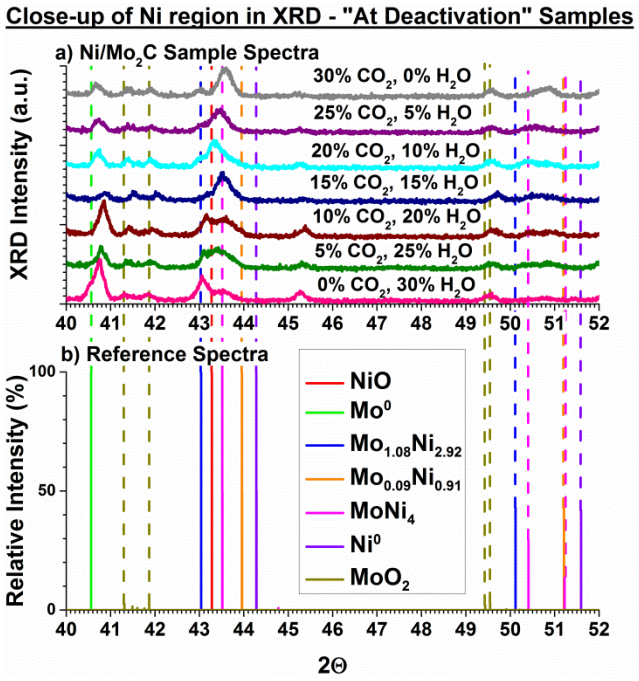

Figure B10: a) Close-up of Ni-region in XRD of catalyst "at deactivation" for all reaction conditions; b) Reference spectra with dashed lines extending into B10a for ease of phase identification.

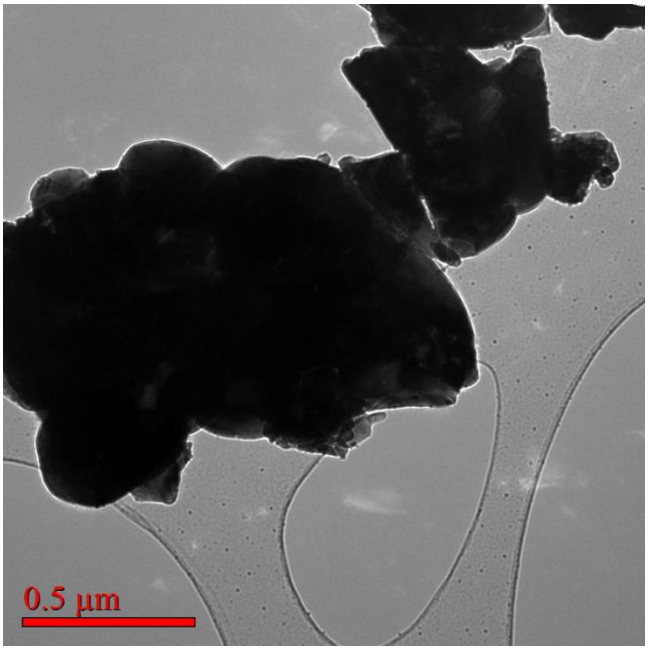

Figure B11: TEM image of NiMo-15/15-AtDeact. The small black dots on the lacey carbon film are 1-10nm in size and likely composed of Ni and Mo.

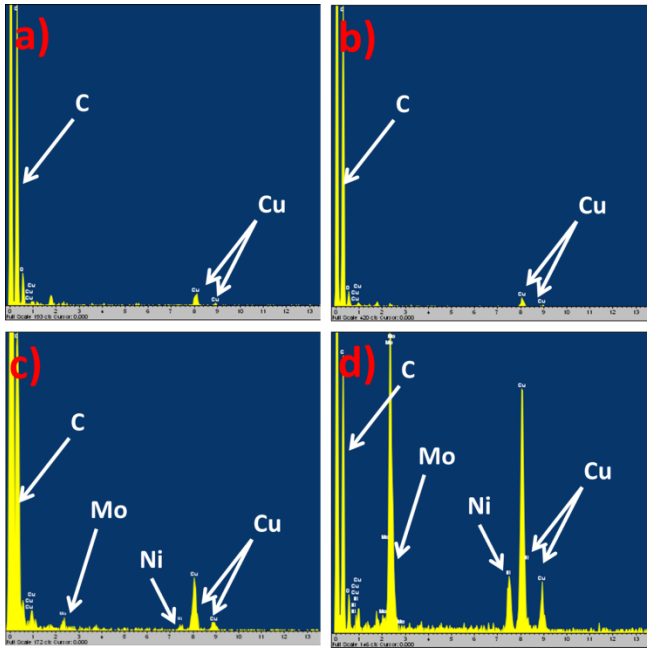

Figure B12: EDS on the carbon film of the TEM grid used to determine the composition of the small nanoparticles seen in Figures 3.5 and B11; a) NiMo-AsSyn, b) NiMo-15/15-MidRxn, c) NiMo-15/15-AtDeact, d) NiMo-15/15-1hDeact. The carbon signal at 0.3eV and the copper signals at about 1eV, 8eV and 9eV are due to the carbon film and copper TEM grid.

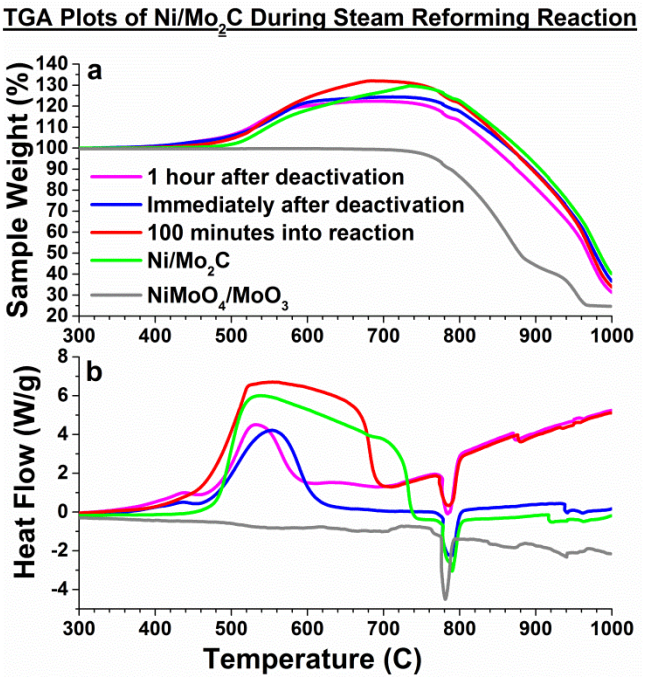

Figure B13: Air-TGA plots of sample weight percent (a) and heat flow (b) for Ni/Mo_2C at various timepoints during the steam reforming reaction. Inconsistencies in slope of Heat Flow data at higher temperatures due to instrument error over time; raw data has been presented here.

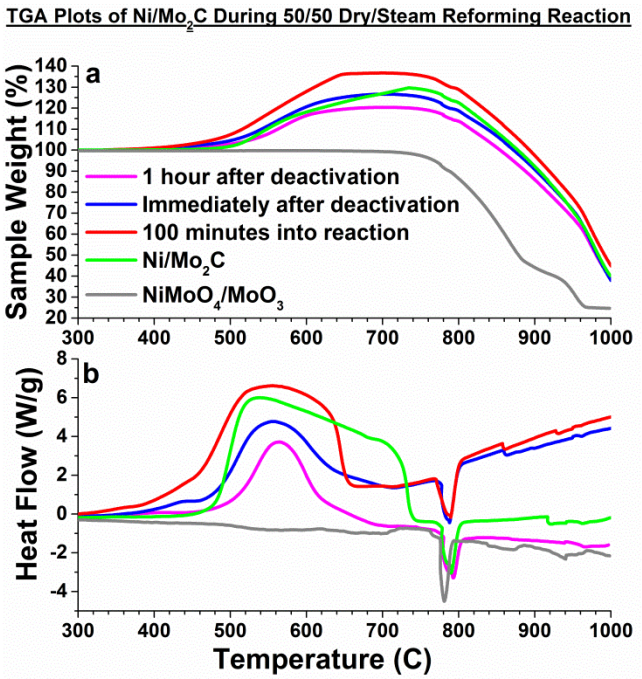

Figure B14: Air-TGA plots of sample weight percent (a) and heat flow (b) for Ni/Mo_2C at various timepoints during 15% CO_2/15% H_2O reforming reaction. Inconsistencies in slope of Heat Flow data at higher temperatures due to instrument error over time; raw data has been presented here.

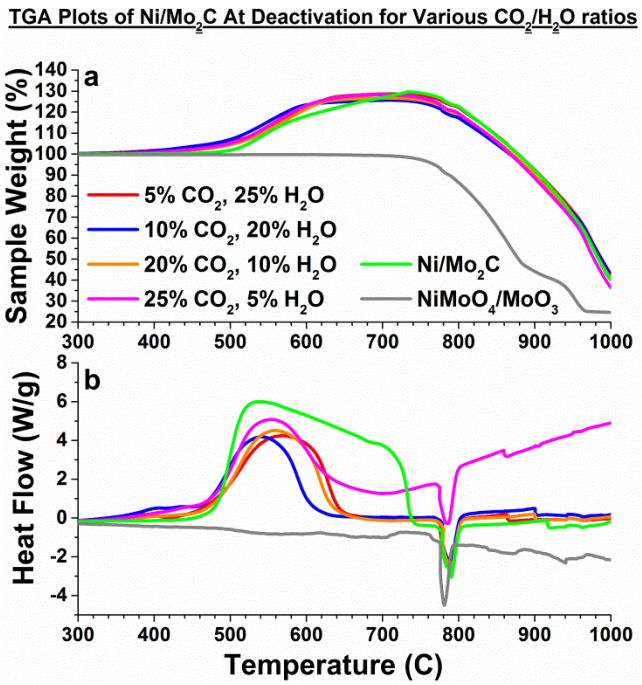

Figure B15: Air-TGA plots of sample weight percent (a) and heat flow (b) for Ni/Mo_2C "at deactivation" for various CO_2:H_2O reaction conditions. Inconsistencies in slope of Heat Flow data at higher temperatures due to instrument error over time; raw data has been presented here.

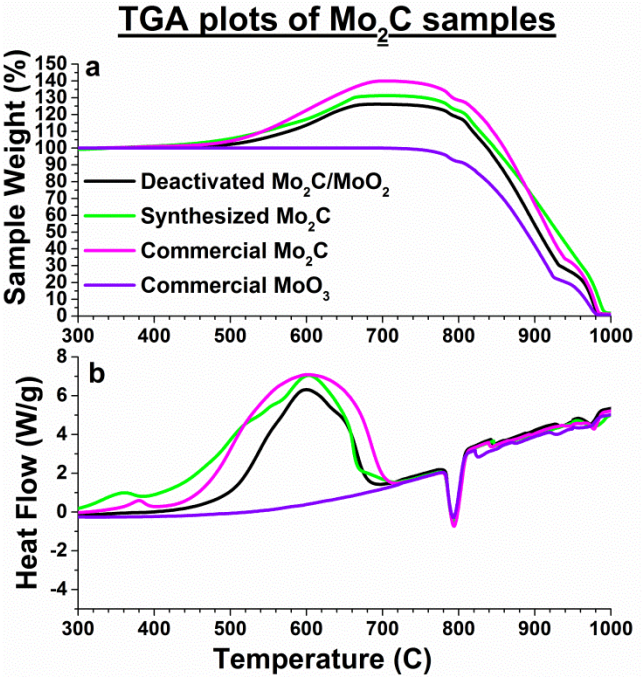

Figure B16: Air-TGA plots of sample weight percent (a) and heat flow (b) for MoO_3, commercial Mo_2C, synthesized Mo_2C, and synthesized Mo_2C subjected to 1 hour of 15% CO_2/15% H_2O reaction conditions. Upward slope of Heat Flow data at higher temperatures due to instrument error over time; raw data has been presented here.

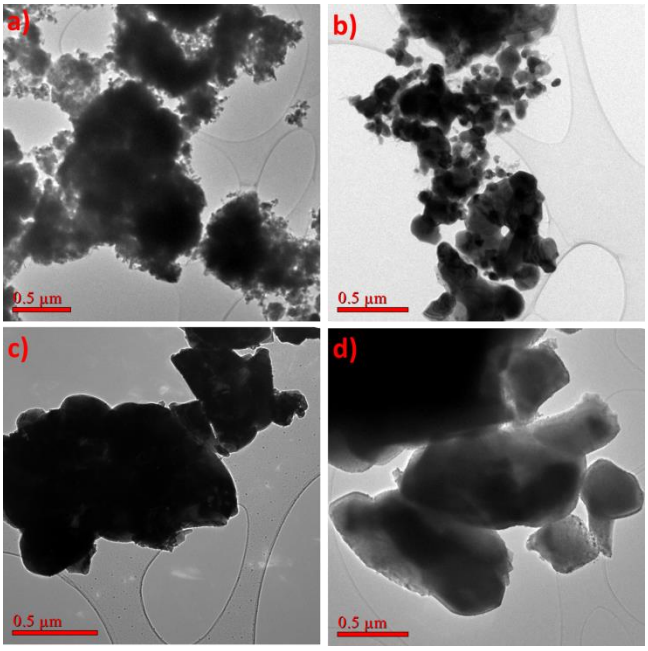

Figure B17: TEM images of the Ni/Mo_2C particles over the course of the 50/50 Dry/Steam reforming reaction: a) NiMo-AsSyn, b) NiMo-15/15-MidRxn, c) NiMo-15/15-AtDeact, d) NiMo-15/15-1hDeact.

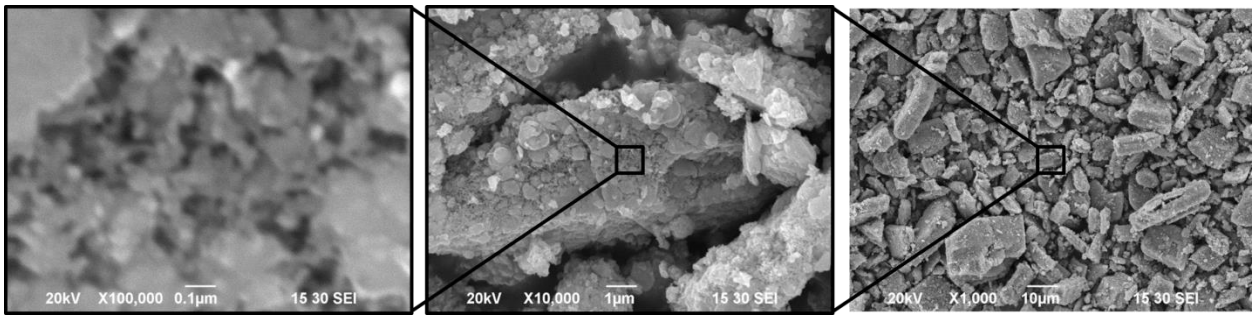

Figure B18: SEM images of NiMo-AsSyn at 1,000x (right image), 10,000x (middle image), and 100,000x (left image).

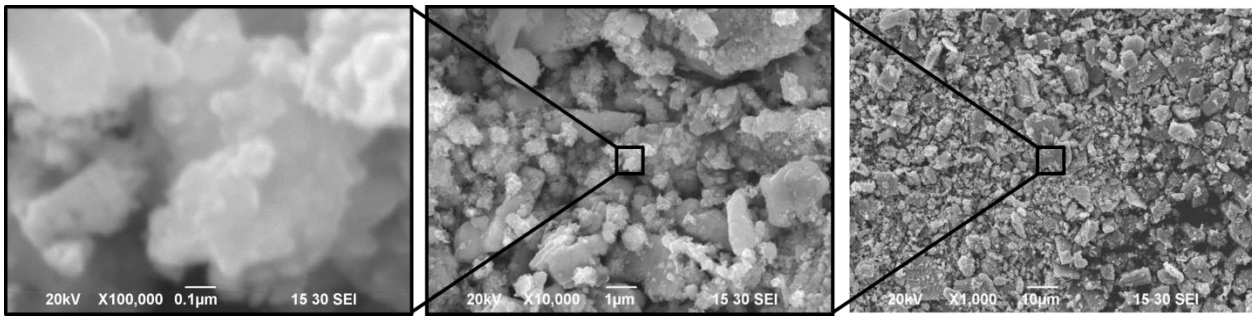

Figure B19: SEM images of NiMo-950C at 1,000x (right image), 10,000x (middle image), and 100,000x (left image).

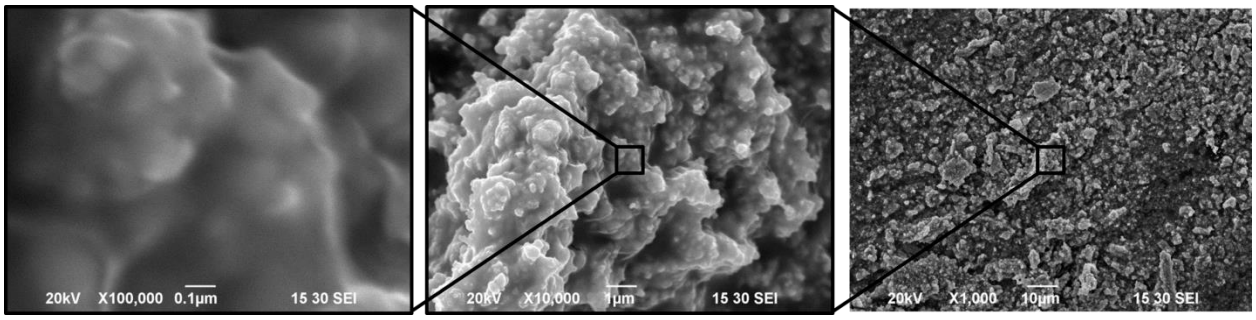

Figure B20: SEM images of NiMo-0/30-MidRxn at 1,000x (right image), 10,000x (middle image), and 100,000x (left image).

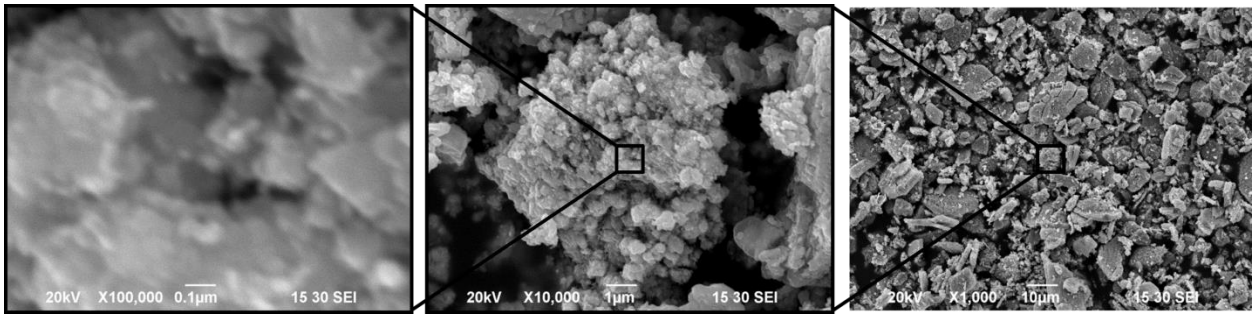

Figure B21: SEM images of NiMo-15/15-MidRxn at 1,000x (right image), 10,000x (middle image), and 100,000x (left image).

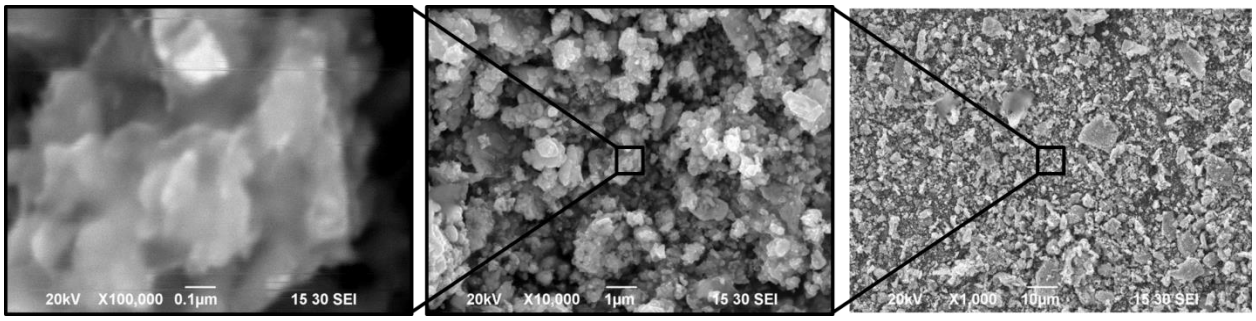

Figure B22: SEM images of NiMo-30/0-MidRxn at 1,000x (right image), 10,000x (middle image), and 100,000x (left image).

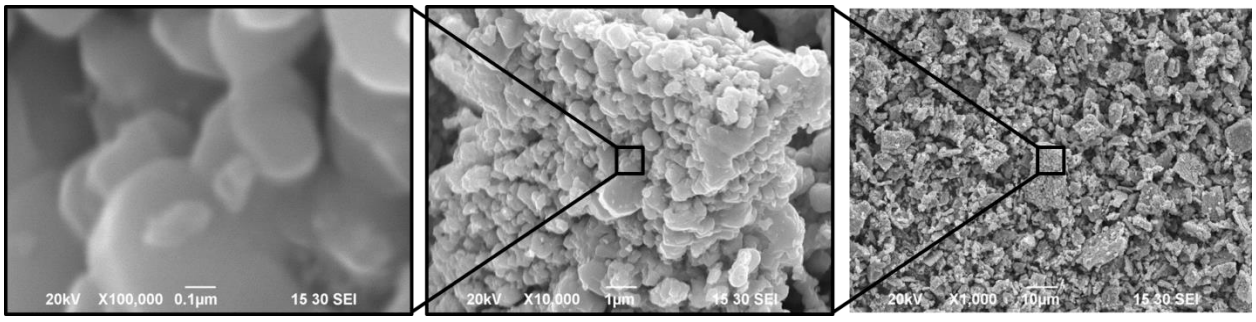

Figure B23: SEM images of NiMo-0/30-AtDeact at 1,000x (right image), 10,000x (middle image), and 100,000x (left image).

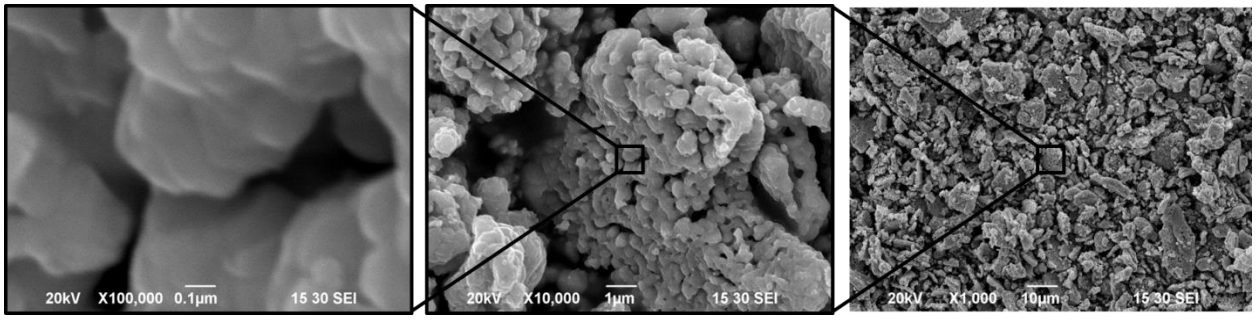

Figure B24: SEM images of NiMo-5/25-AtDeact at 1,000x (right image), 10,000x (middle image), and 100,000x (left image).

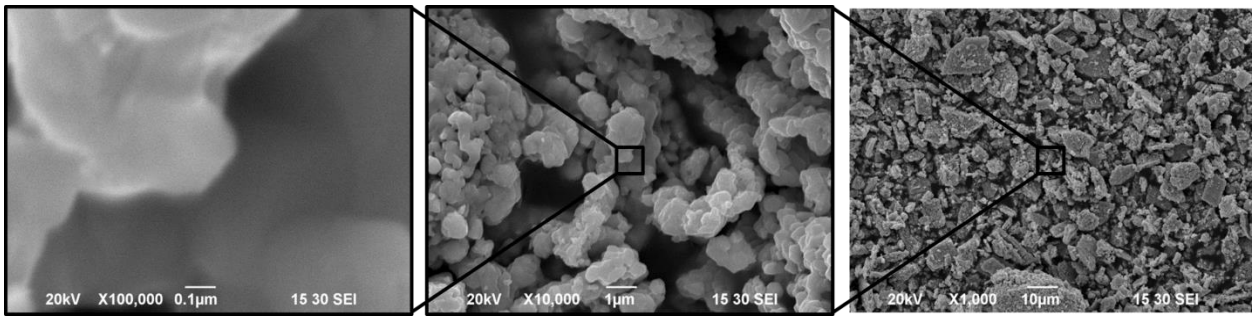

Figure B25: SEM images of NiMo-10/20-AtDeact at 1,000x (right image), 10,000x (middle image), and 100,000x (left image).

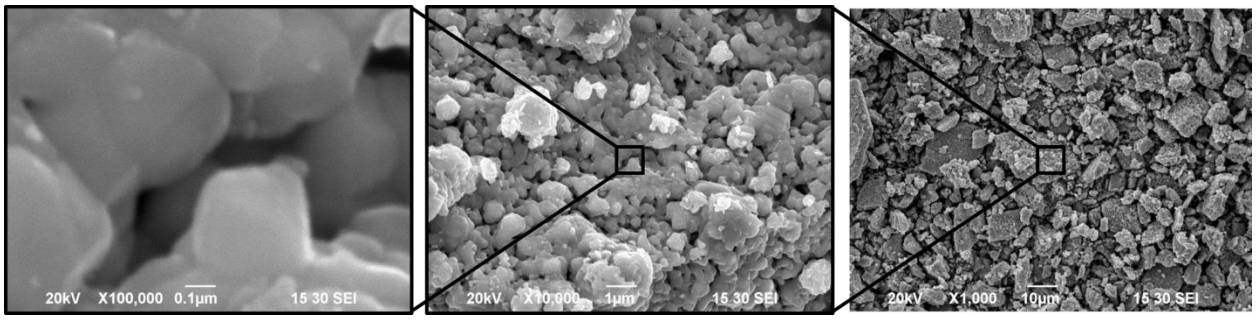

Figure B26: SEM images of NiMo-15/15-AtDeact at 1,000x (right image), 10,000x (middle image), and 100,000x (left image).

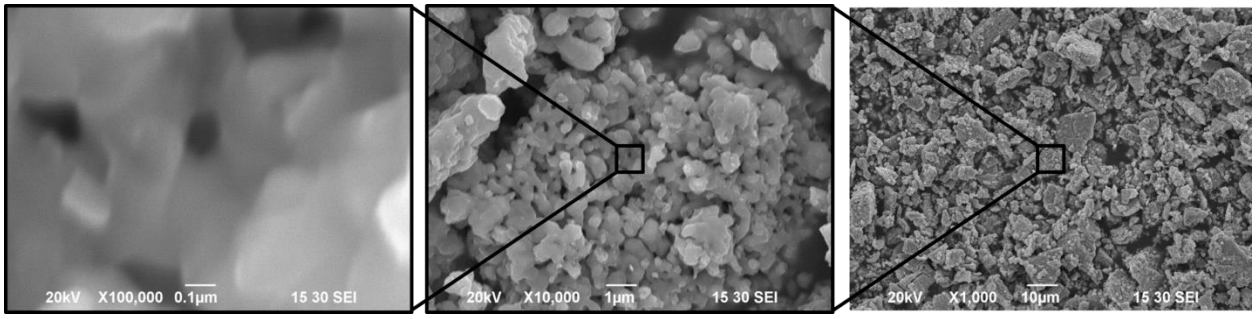

Figure B27: SEM images of NiMo-20/10-AtDeact at 1,000x (right image), 10,000x (middle image), and 100,000x (left image).

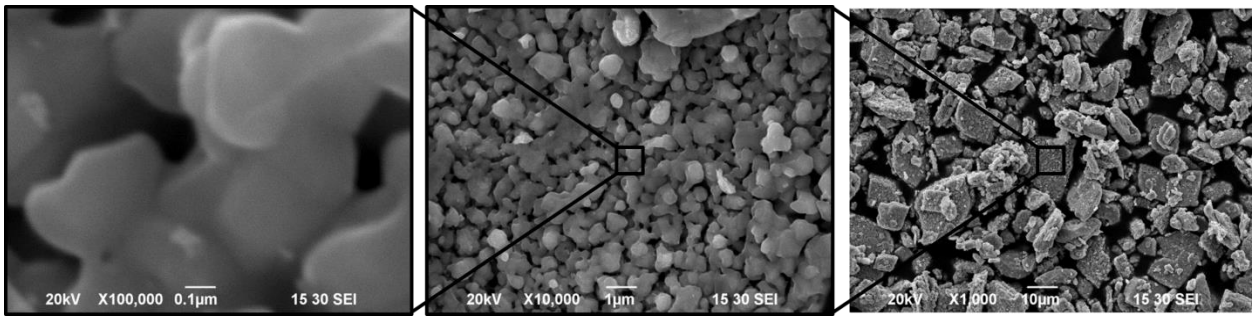

Figure B28: SEM images of NiMo-25/5-AtDeact at 1,000x (right image), 10,000x (middle image), and 100,000x (left image).

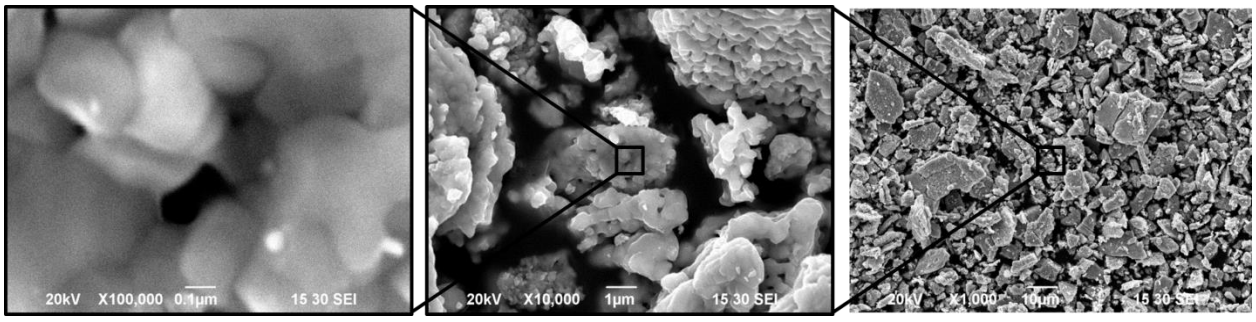

Figure B29: SEM images of NiMo-30/0-AtDeact at 1,000x (right image), 10,000x (middle image), and 100,000x (left image).

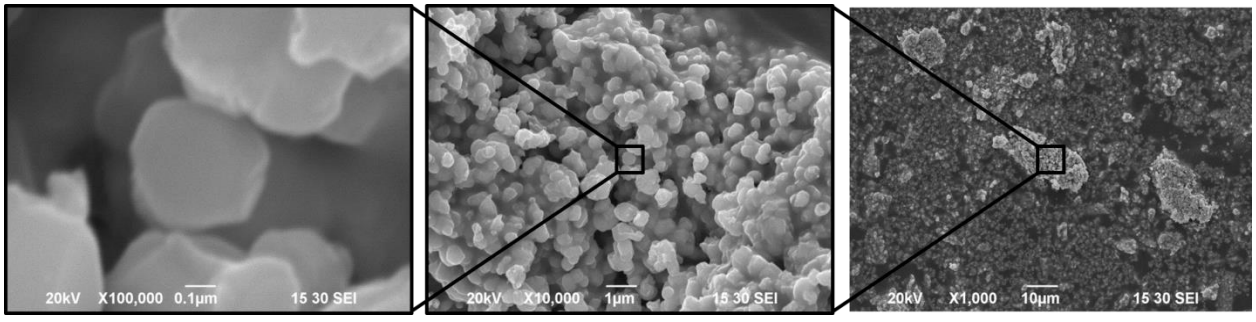

Figure B30: SEM images of NiMo-0/30-1hDeact at 1,000x (right image), 10,000x (middle image), and 100,000x (left image).

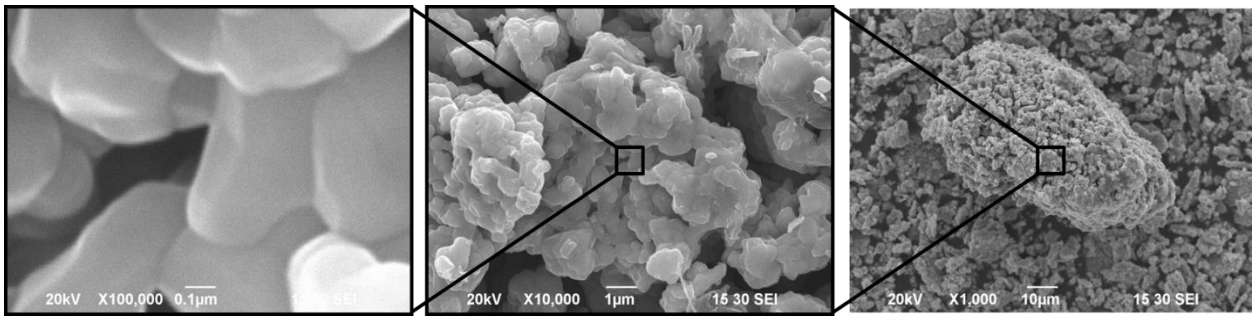

Figure B31: SEM images of NiMo-15/15-1hDeact at 1,000x (right image), 10,000x (middle image), and 100,000x (left image).

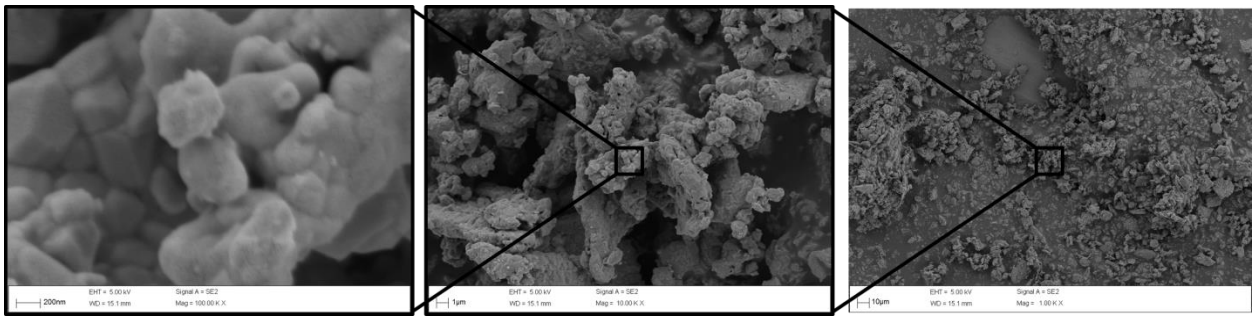

Figure B32: SEM images of NiMo-30/0-1hDeact at 1,000x (right image), 10,000x (middle image), and 100,000x (left image). Images taken with a Zeiss Supra 40VP FE-SEM.

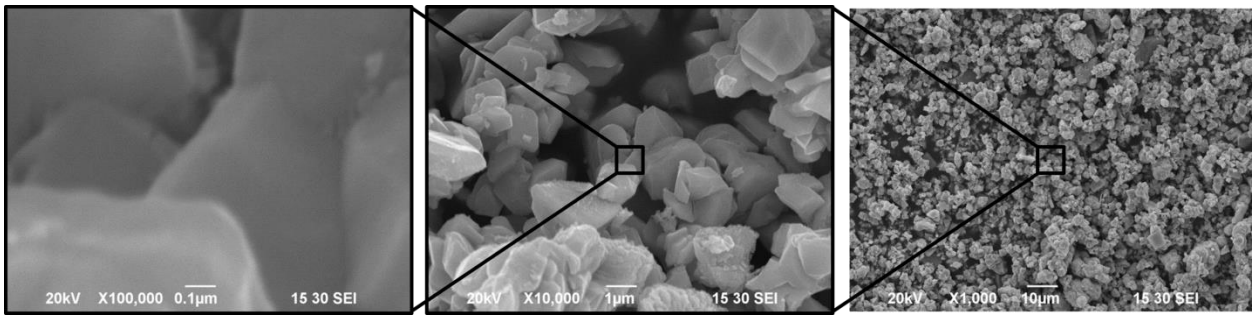

Figure B33: SEM images of Mo_2C-AsSyn at 1,000x (right image), 10,000x (middle image), and 100,000x (left image).

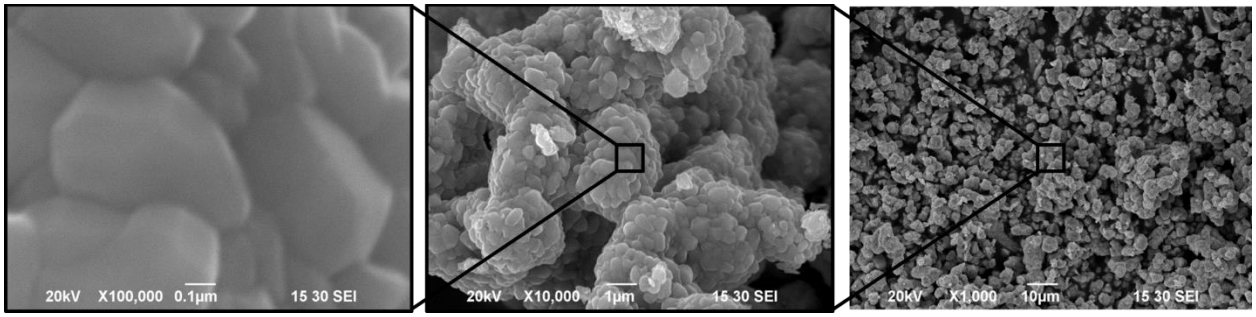

Figure B34: SEM images of Mo_2C-0/30-1hDeact at 1,000x (right image), 10,000x (middle image), and 100,000x (left image).

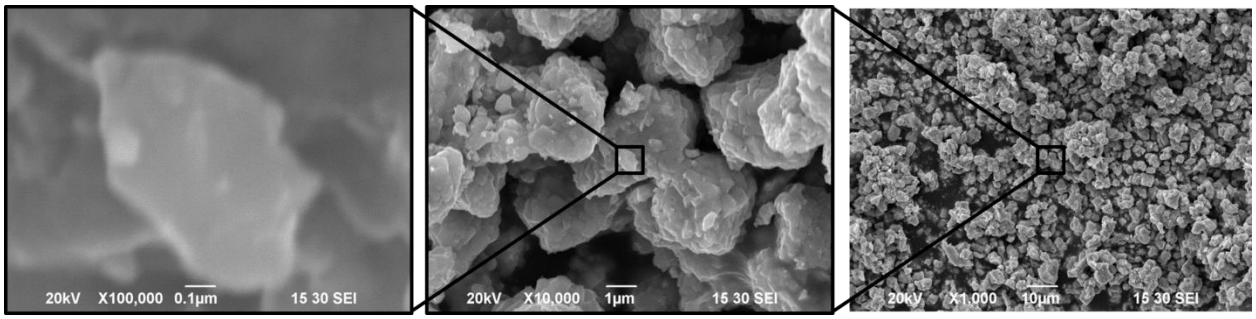

Figure B35: SEM images of Mo_2C-15/15-1hDeact at 1,000x (right image), 10,000x (middle image), and 100,000x (left image).

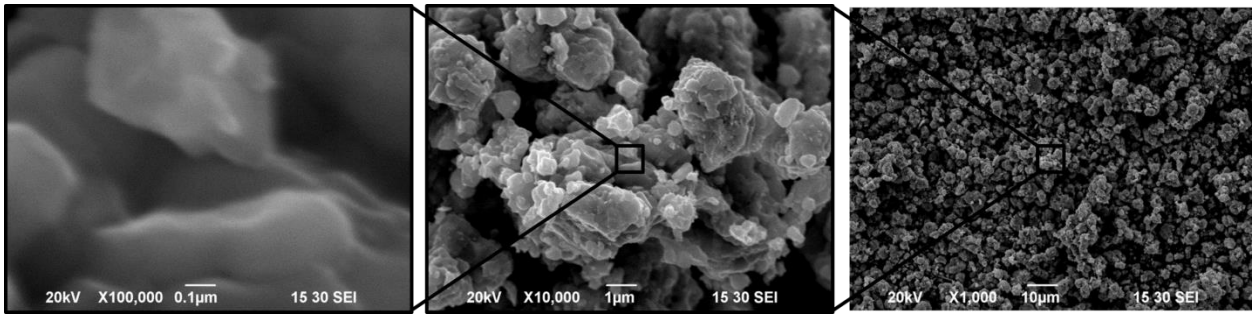

Figure B36: SEM images of Mo_2C-30/0-1hDeact at 1,000x (right image), 10,000x (middle image), and 100,000x (left image).

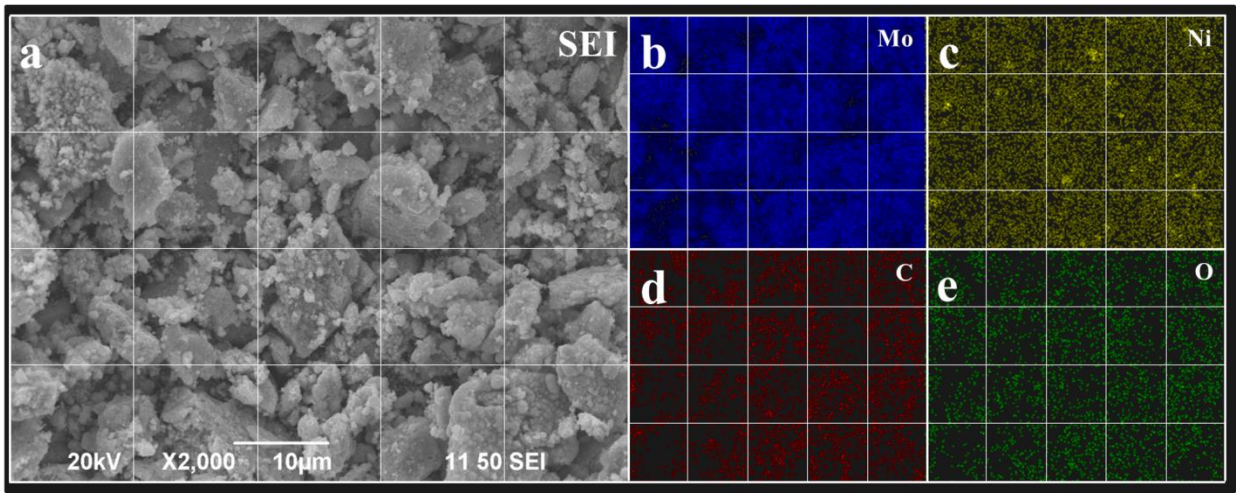

Figure B37: EDX mapping of NiMo-AsSyn at 2,000x. a) SEI; b) Mo; c) Ni; d) C; e) O.

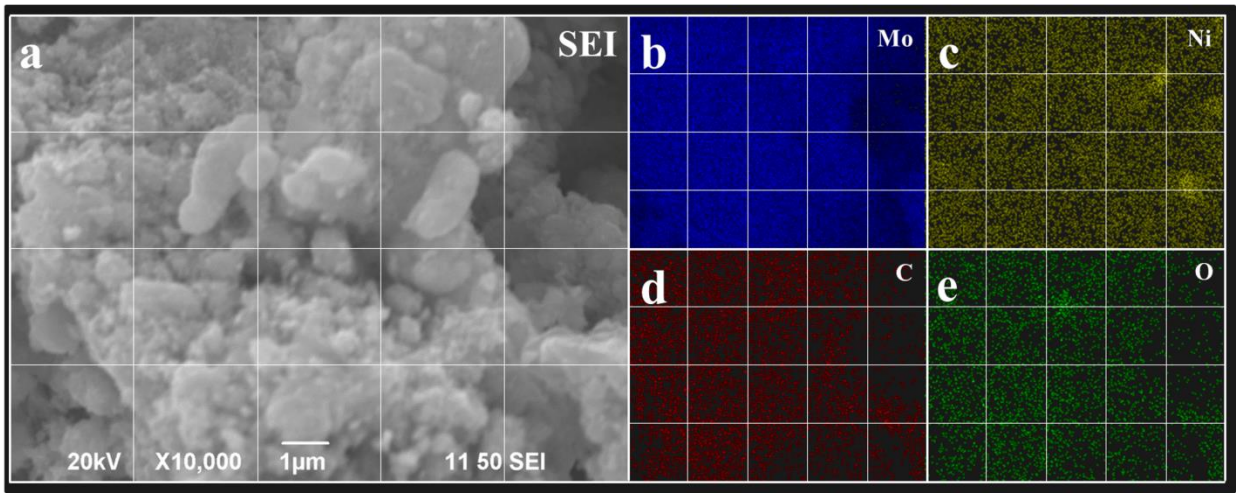

Figure B38: EDX mapping of NiMo-AsSyn at 10,000x. a) SEI; b) Mo; c) Ni; d) C; e) O

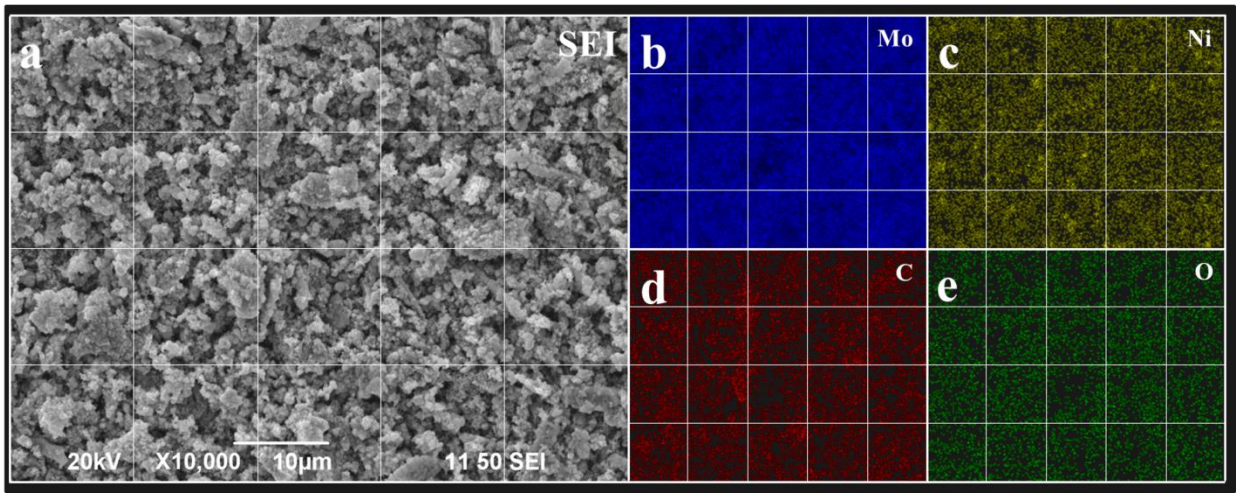

Figure B39: EDX mapping of NiMo-0/30-MidRxn at 2,000x. a) SEI; b) Mo; c) Ni; d) C; e) O

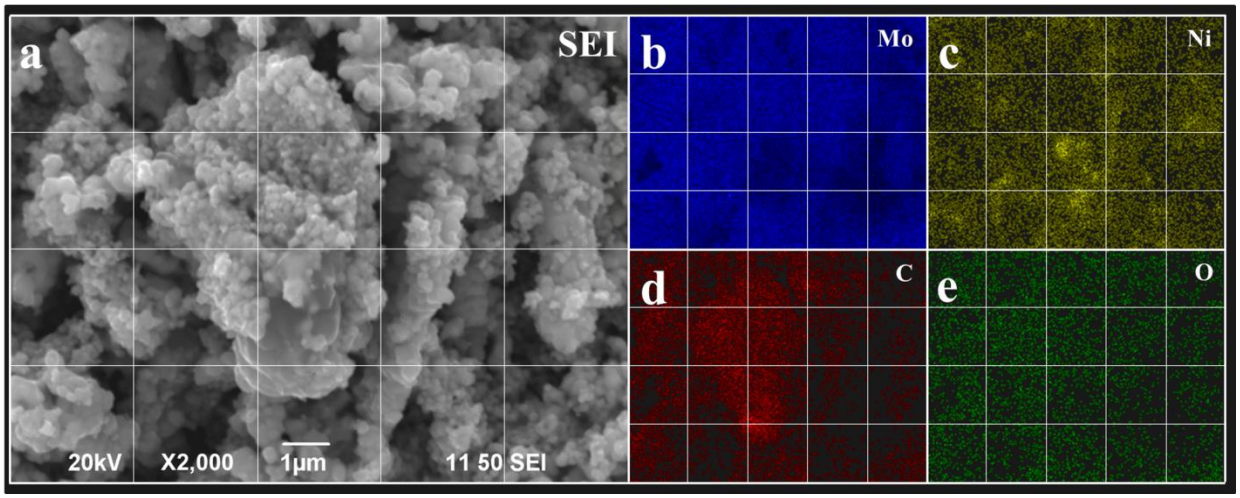

Figure B40: EDX mapping of NiMo-0/30-MidRxn at 10,000x. a) SEI; b) Mo; c) Ni; d) C; e) O

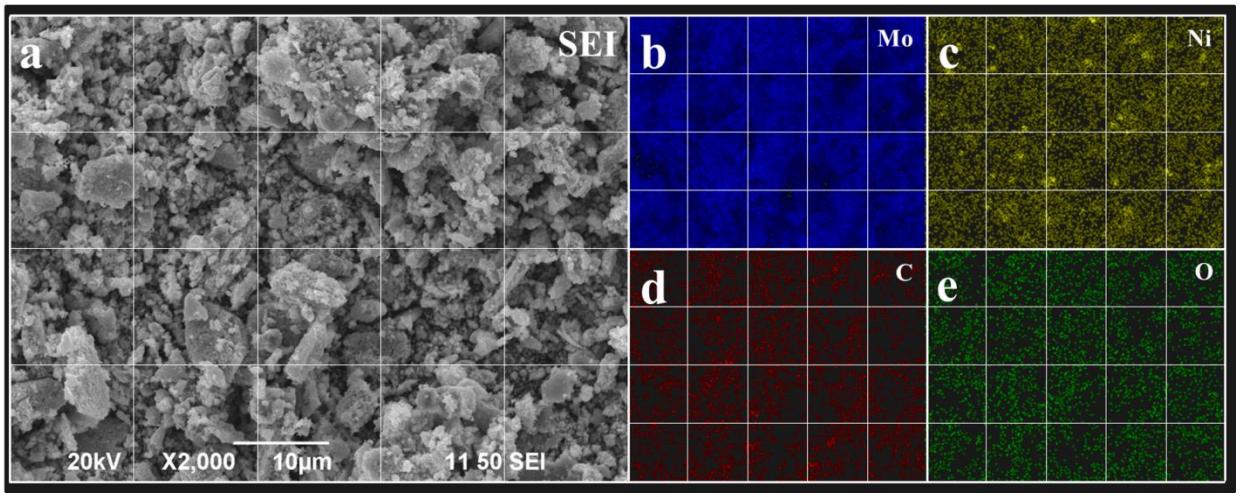

Figure B41: EDX mapping of NiMo-15/15-MidRxn at 2,000x. a) SEI; b) Mo; c) Ni; d) C; e) O

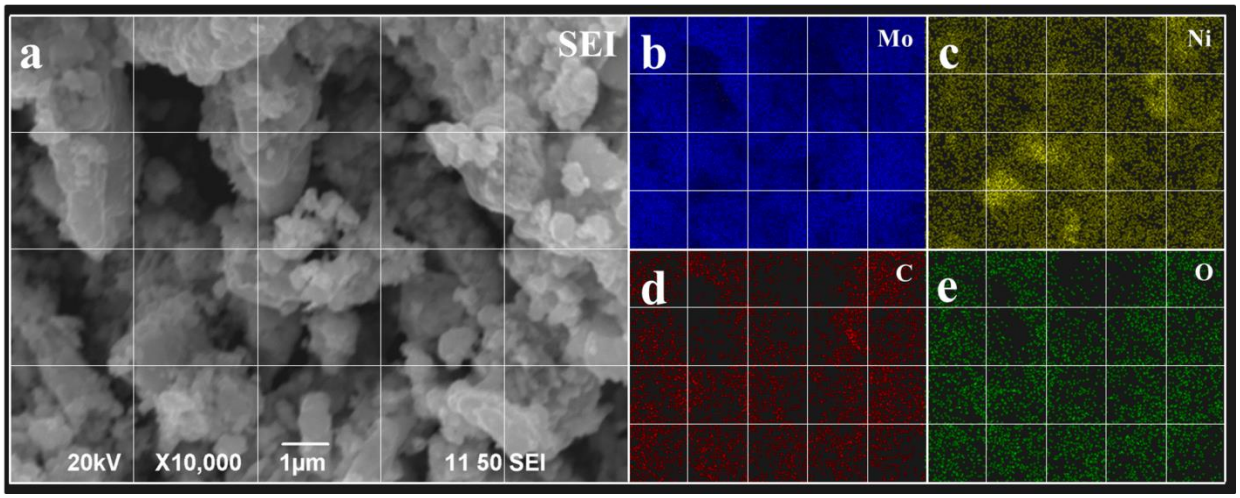

Figure B42: EDX mapping of NiMo-15/15-MidRxn at 10,000x. a) SEI; b) Mo; c) Ni; d) C; e) O

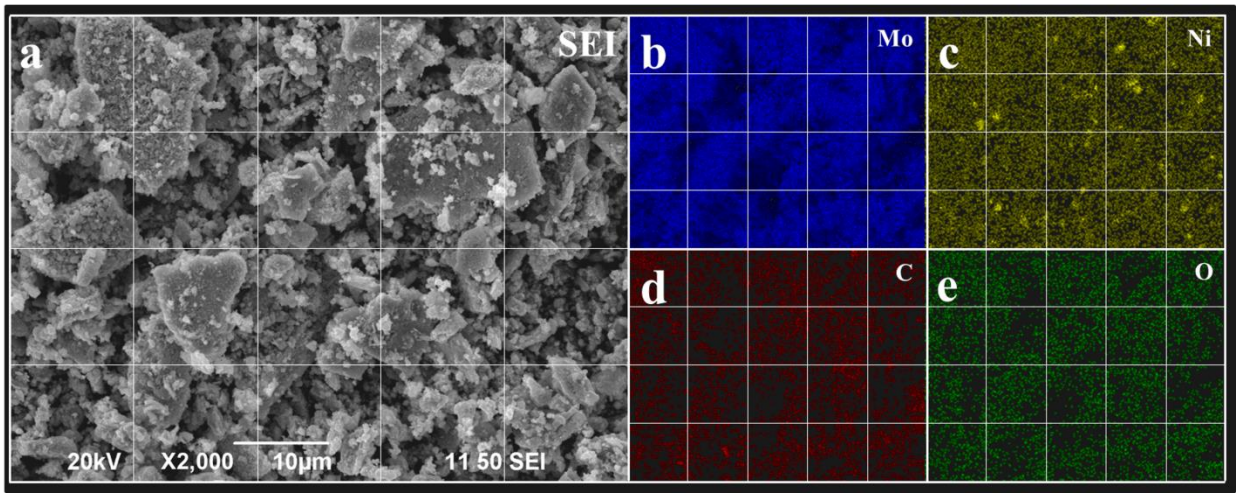

Figure B43: EDX mapping of NiMo-30/0-MidRxn at 2,000x. a) SEI; b) Mo; c) Ni; d) C; e) O

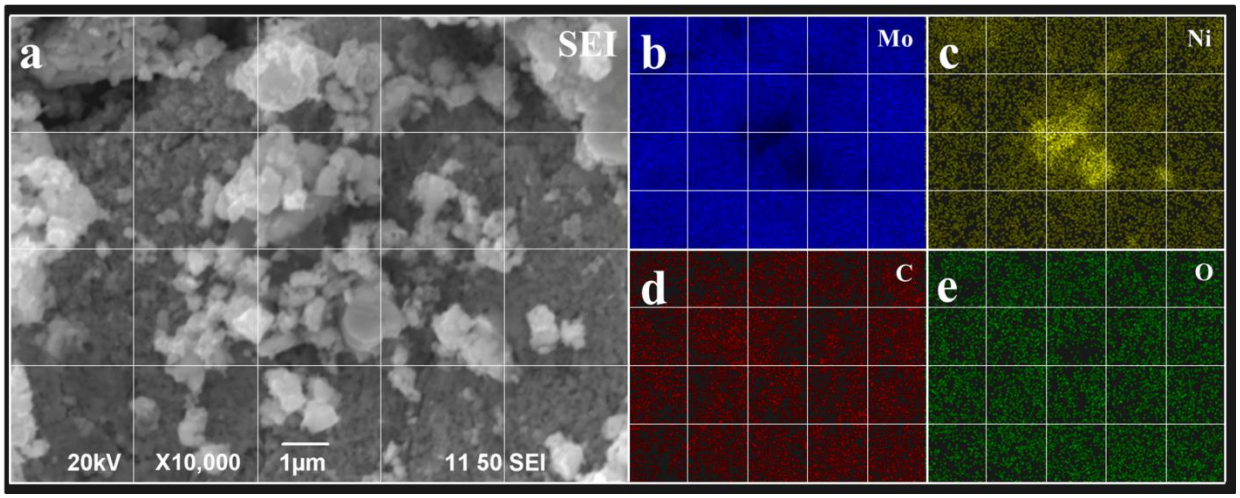

Figure B44: EDX mapping of NiMo-30/0-MidRxn at 10,000x. a) SEI; b) Mo; c) Ni; d) C; e) O

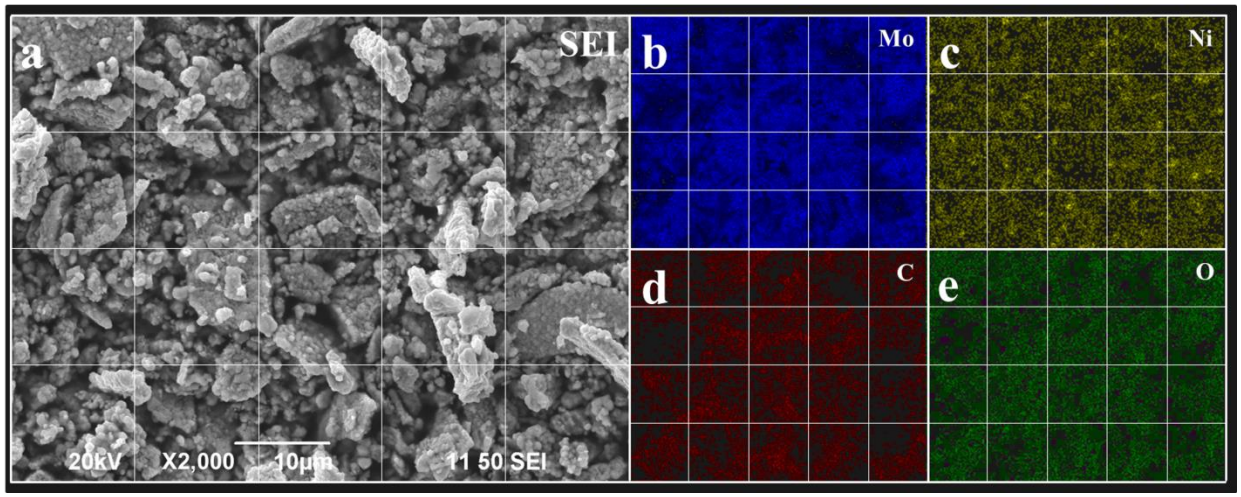

Figure B45: EDX mapping of NiMo-0/30-AtDeact at 2,000x. a) SEI; b) Mo; c) Ni; d) C; e) O

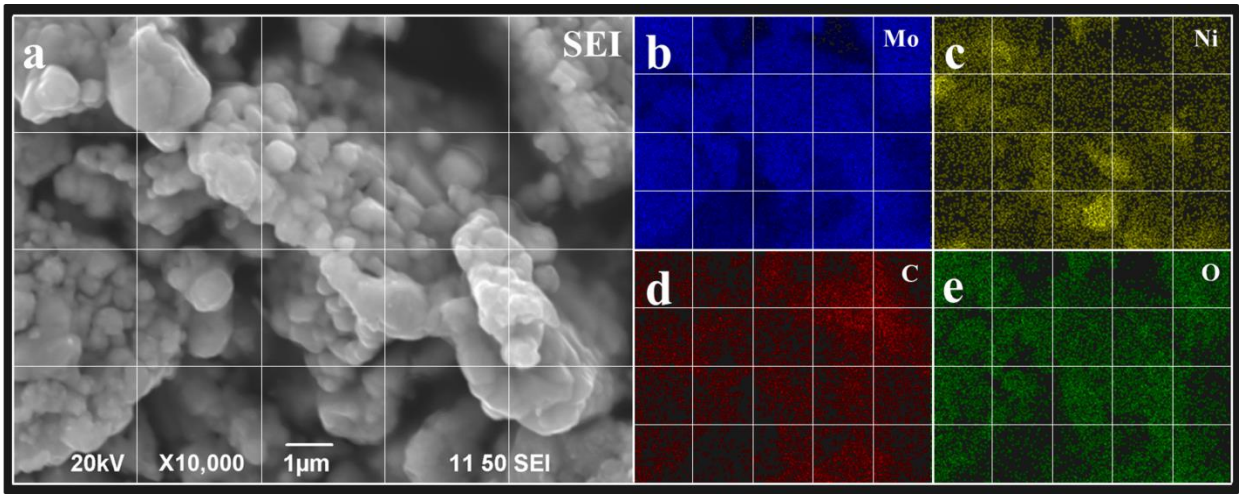

Figure B46: EDX mapping of NiMo-0/30-AtDeact at 10,000x. a) SEI; b) Mo; c) Ni; d) C; e) O

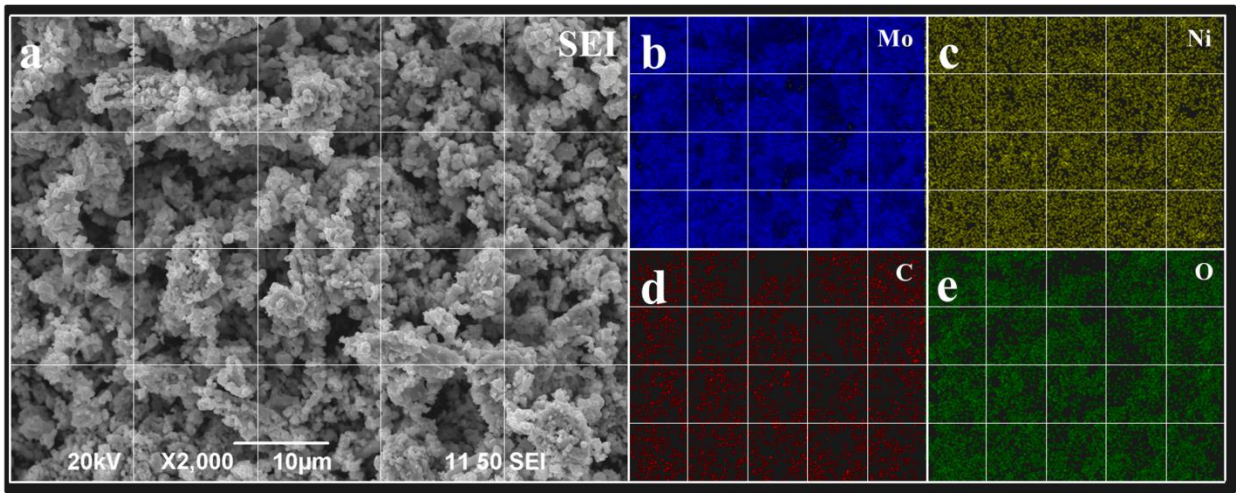

Figure B47: EDX mapping of NiMo-15/15-AtDeact at 2,000x. a) SEI; b) Mo; c) Ni; d) C; e) O

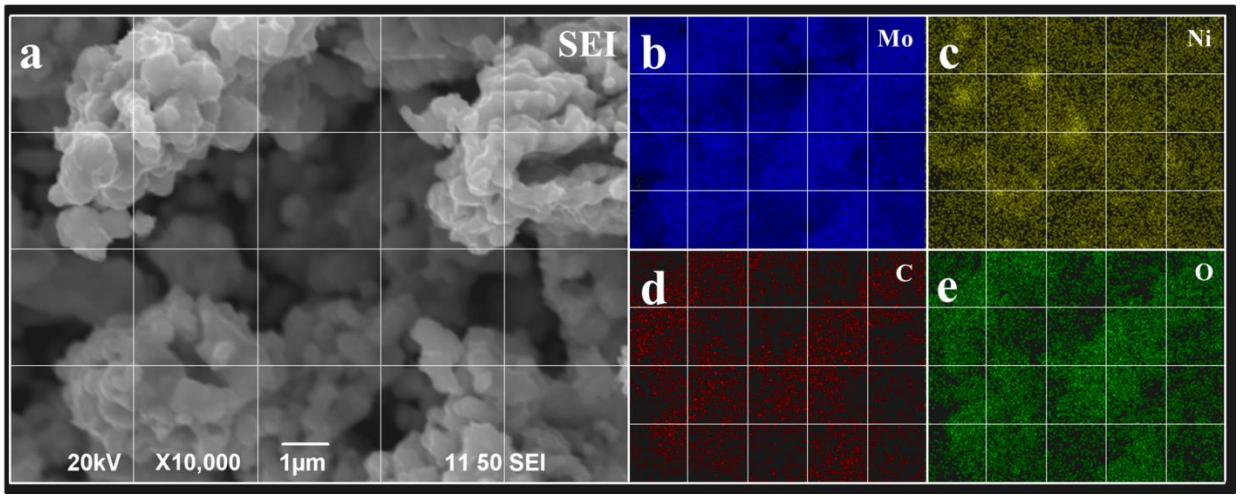

Figure B48: EDX mapping of NiMo-15/15-AtDeact at 10,000x. a) SEI; b) Mo; c) Ni; d) C; e) O

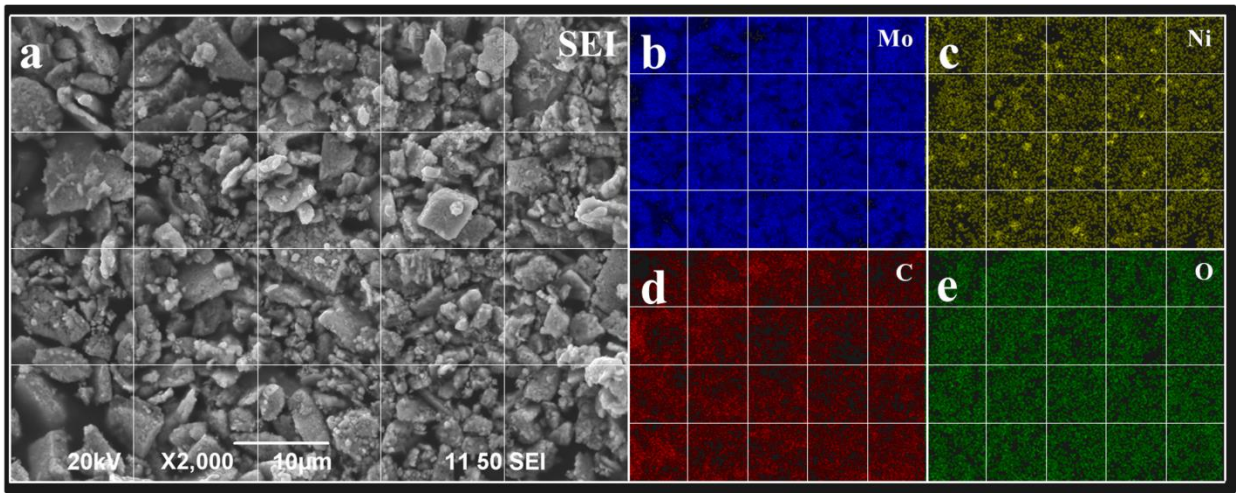

Figure B49: EDX mapping of NiMo-30/0-AtDeact at 2,000x. a) SEI; b) Mo; c) Ni; d) C; e) O

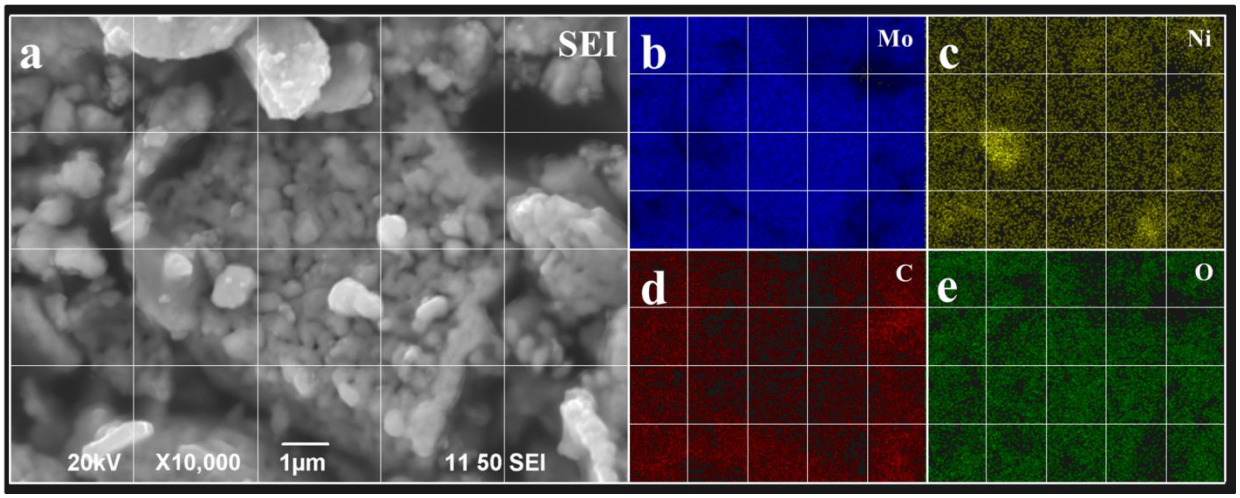

Figure B50: EDX mapping of NiMo-30/0-AtDeact at 10,000x. a) SEI; b) Mo; c) Ni; d) C; e) O

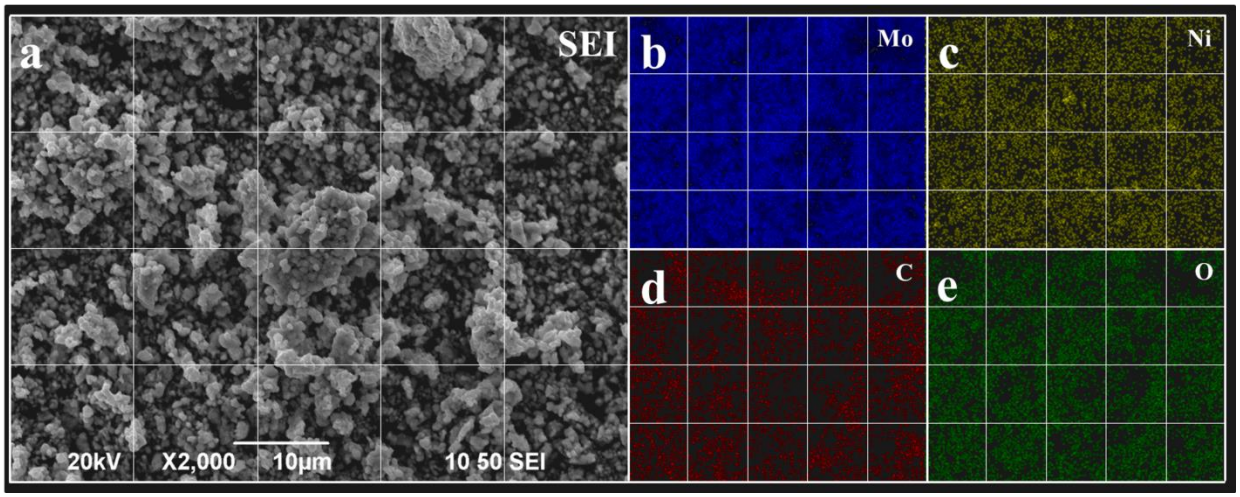

Figure B51: EDX mapping of NiMo-0/30-1hDeact at 2,000x. a) SEI; b) Mo; c) Ni; d) C; e) O

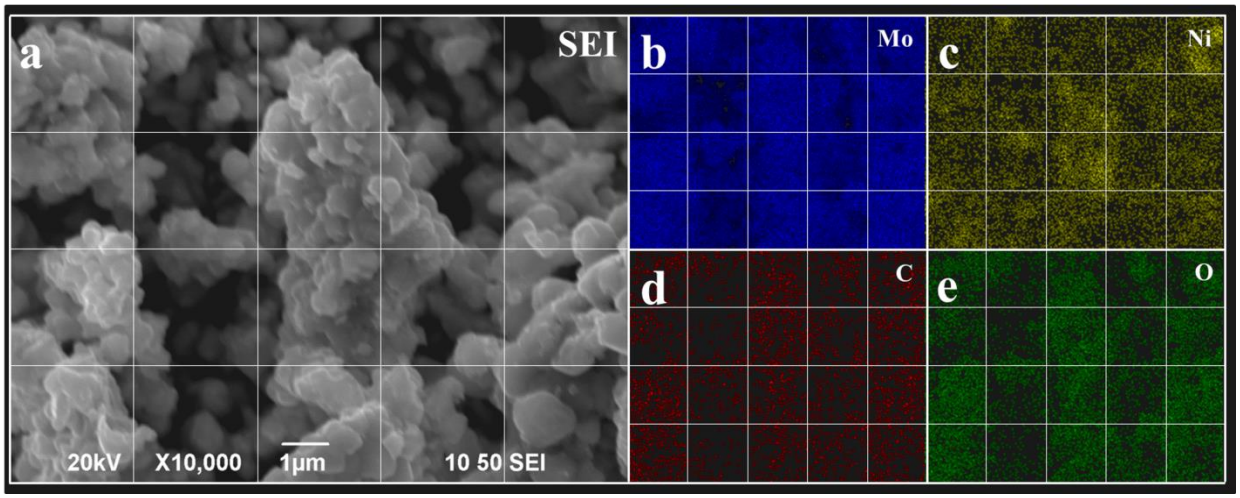

Figure B52: EDX mapping of NiMo-0/30-1hDeact at 10,000x. a) SEI; b) Mo; c) Ni; d) C; e) O

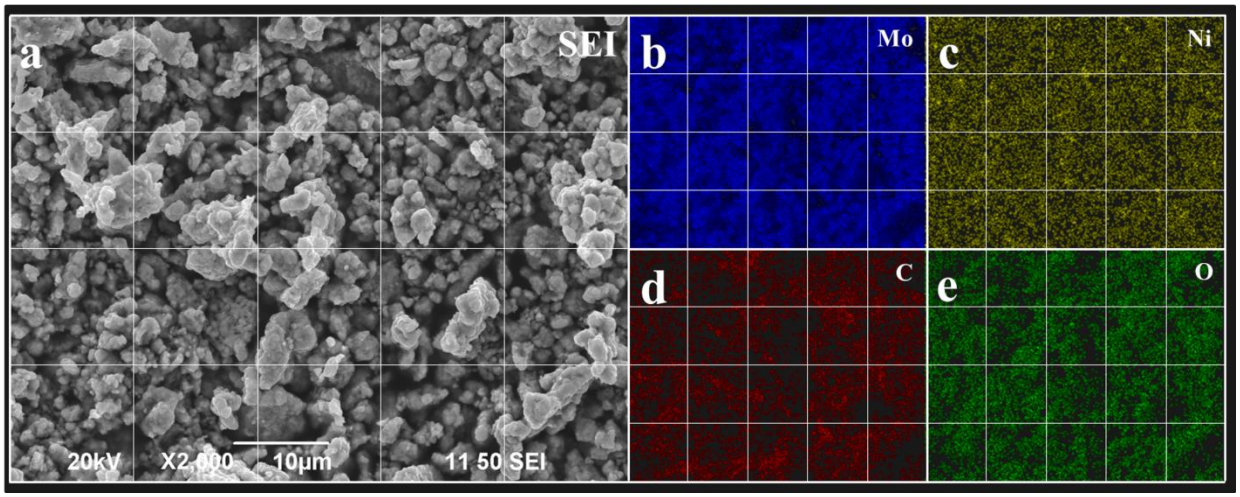

Figure B53: EDX mapping of NiMo-15/15-1hDeact at 2,000x. a) SEI; b) Mo; c) Ni; d) C; e) O

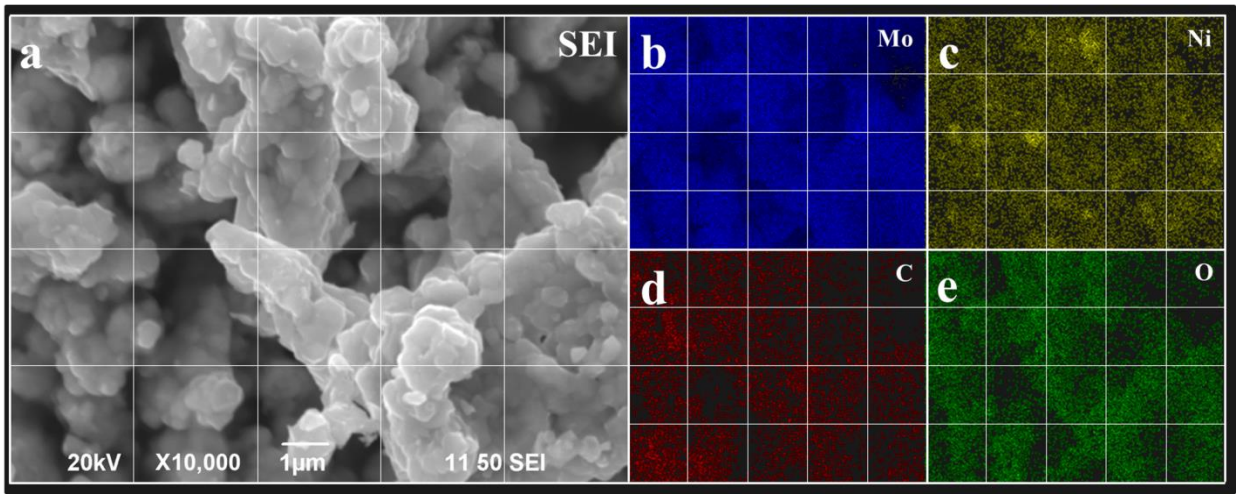

Figure B54: EDX mapping of NiMo-15/15-1hDeact at 10,000x. a) SEI; b) Mo; c) Ni; d) C; e) O

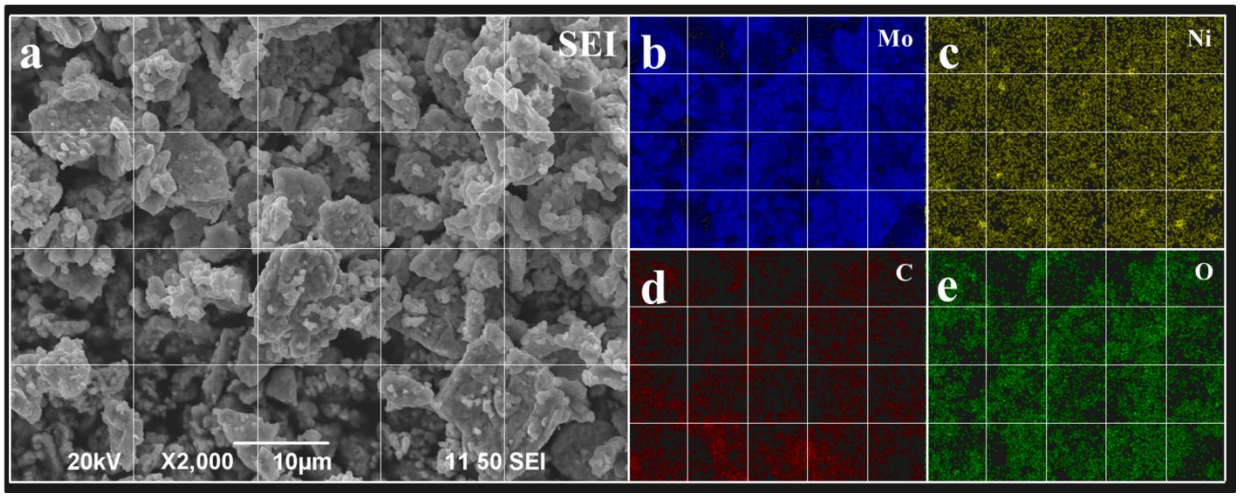

Figure B55: EDX mapping of NiMo-30/0-1hDeact at 2,000x. a) SEI; b) Mo; c) Ni; d) C; e) O

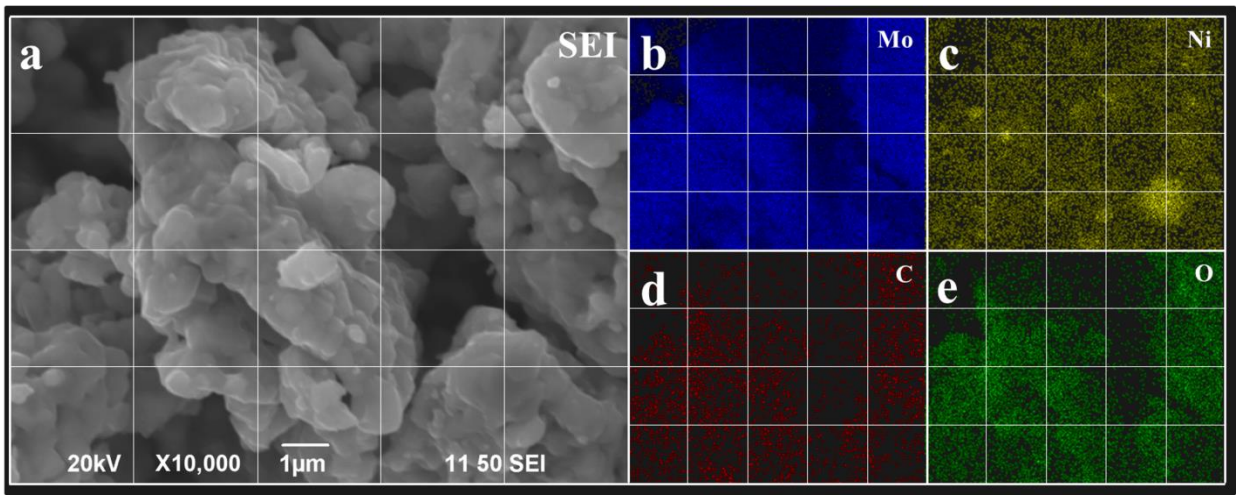

Figure B56: EDX mapping of NiMo-30/0-1hDeact at 10,000x. a) SEI; b) Mo; c) Ni; d) C; e) O

Appendix C: Supporting Information for Evidence of Methane Adsorption Over Mo_2C Involving Single C-H Bond Dissociation Instead of Facile Carbon Exchange

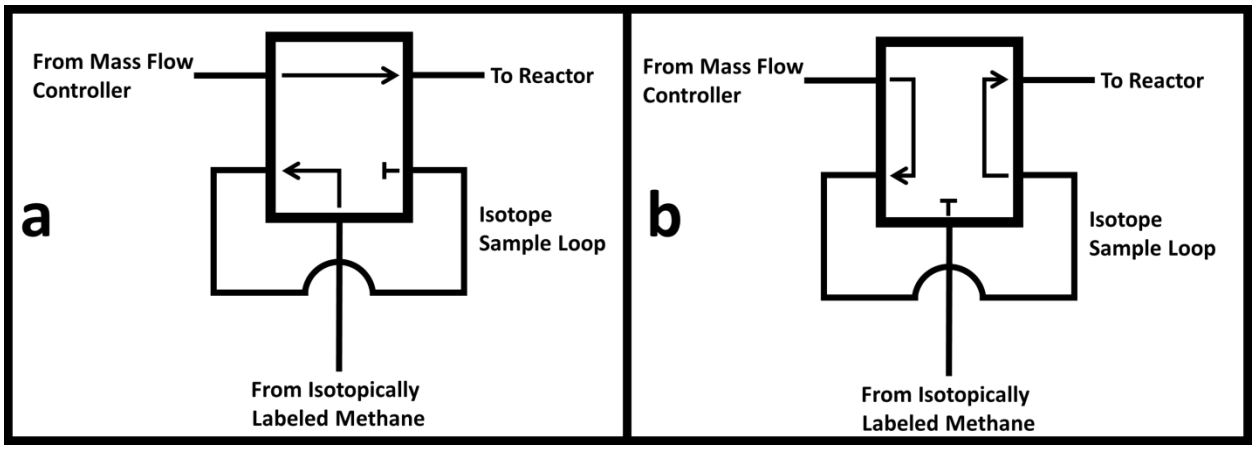

Figure C1: General flow pattern for the 5-port valve and isotope sample loop. a) "Load" position, where isotopically labeled gas is loaded into the sample loop. b) "Inject" position, used to deliver the pulse of isotopically labeled methane to the reactor

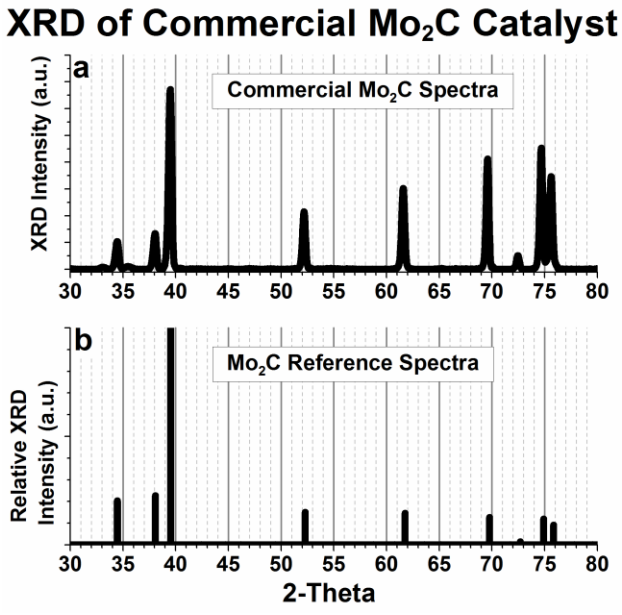

Figure C2: a) XRD spectra of Alfa Aesar Commercial Mo_2C and b) reference spectra for Mo_2C.

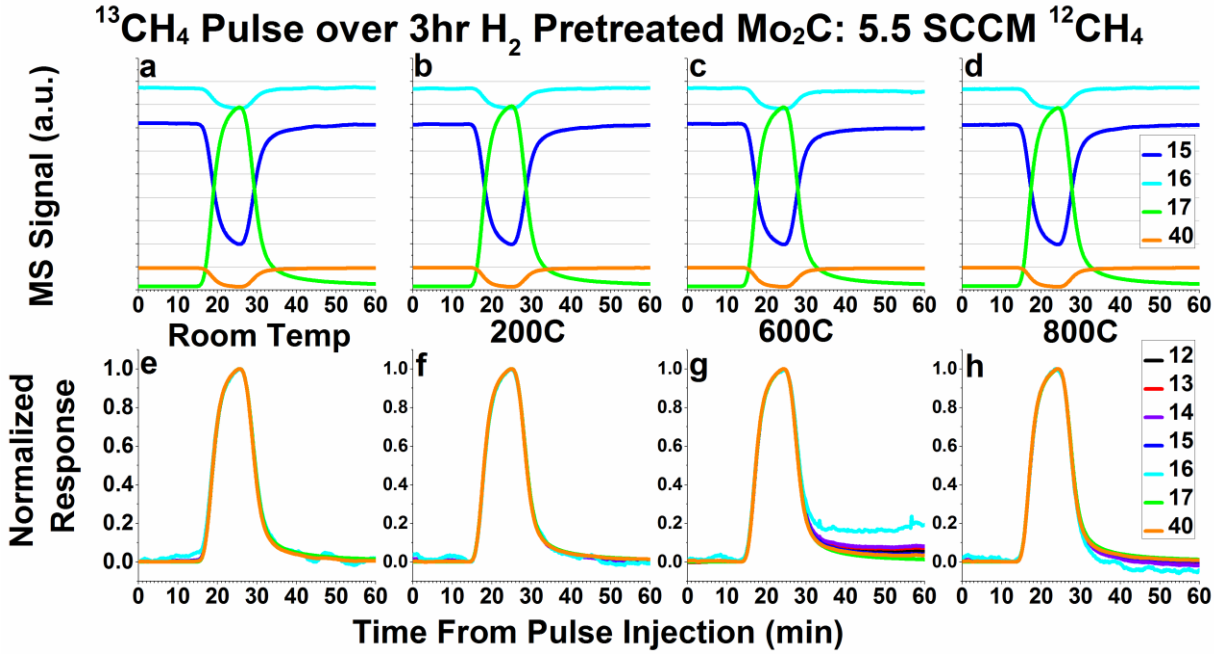

Figure C3: Raw mass spectrometry signals (a-d) and normalized responses (e-h) for $^{13}CH_4$ pulses while flowing 5.5 SCCM 95% CH_4/5% Ar over Mo_2C at room temperature (a & e), 200°C (b & f), 600°C (c & g), and 800°C (d & h). In Figures C3e-C3h, masses 12, 13, 14, 15, and 16 have been inverted in addition to normalized, in order to overlay the pulse response functions. Pretreatment was 50 SCCM flowing H_2 at 600C for 3 hours. The masses correspond to the following species or fragments: 12: ^{12}C; 13: ^{12}CH, ^{13}C; 14:$^{12}CH_2$, ^{13}CH; 15: $^{12}CH_3$, $^{13}CH_2$; 16: $^{12}CH_4$, $^{13}CH_3$; 17: $^{13}CH_4$; 40: Ar (inert tracer).

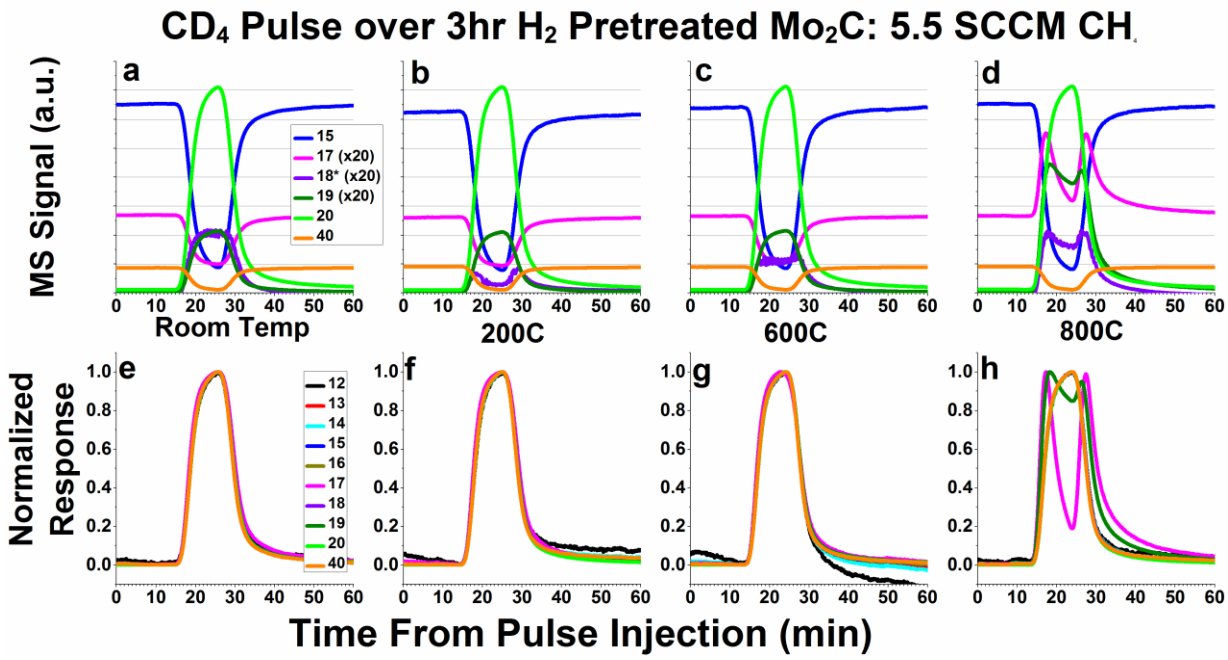

Figure C4: Mass Spectrometry signals (a-d) and normalized responses (e-h) for CD_4 pulses while flowing 5.5 SCCM 95% CH_4/5% Ar over Mo_2C in the bypass (a & e), at 200°C (b & f), at 600°C (c & g), and at 800°C (d & h). In Figures C4a-C4d, masses 17 and 19 have been multiplied by 20. In Figures C4a-C4d, mass 18 has been corrected by subtracting 0.78*(mass 20), then multiplied by 20, but has been left uncorrected for Figures C4e-C4h. In Figures C4e-C4g, masses 12, 13, 14, 15, 16, and 17 have been inverted in addition to normalized in order to overlay the pulse response functions. In Figure C4h, only masses 12, 13, 14, 15, and 16 have been inverted. The masses correspond to the following species or fragments:12: C; 13: CH; 14: CH_2, CD; 15: CH_3, CDH; 16: CH_4, CD_2, CDH_2; 17: CH_3D, CD_2H; 18: CD_3, CD_2H_2; 19: CD_3H; 20: CD_4; 40: Ar (inert tracer).

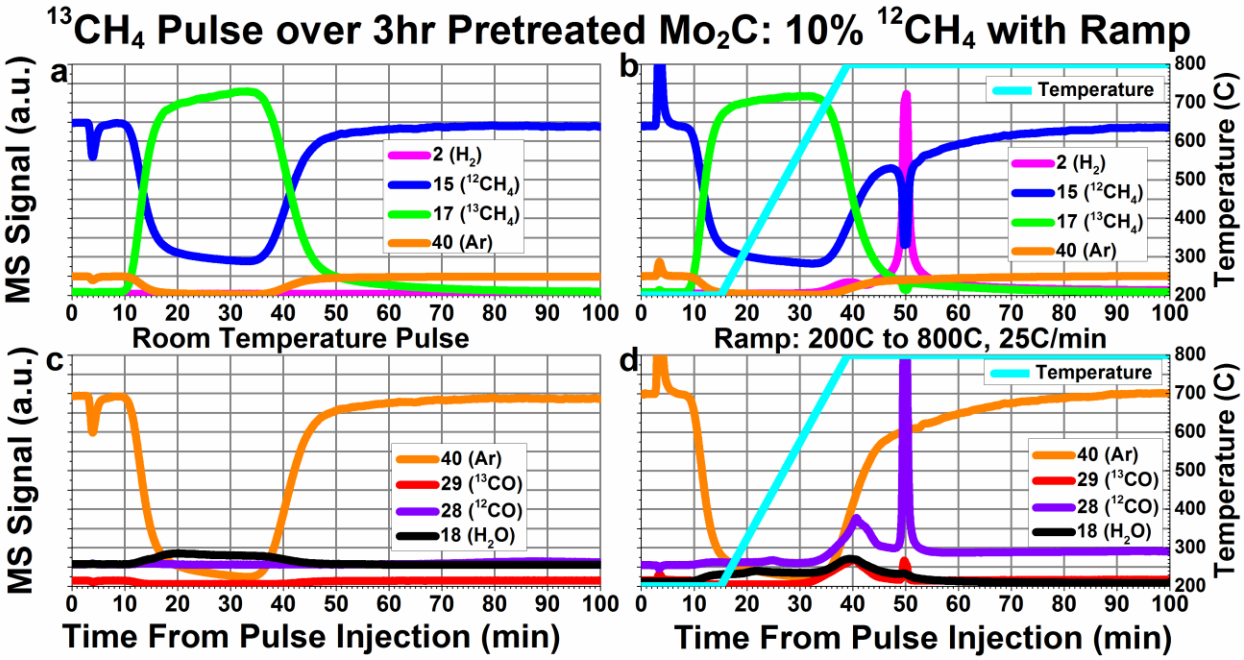

Figure C5: Raw mass spectrometry curves for $^{13}CH_4$ pulses delivered while flowing 18 SCCM He, and 2 SCCM 95% CH_4/5% Ar after 3 hours of H_2 pretreatment at 600C. Plots for masses 2 (H_2), 15 ($^{12}CH_4$), 17 ($^{13}CH_4$), and 40 (Ar) are shown in Figures C5a and C5b. Figures for masses 40 (Ar), 28 (^{12}CO), 29 (^{13}CO), and 18 (H_2O) are shown in Figures C5c and C5d, and represent a 10x magnification from Figures 4a and 4b. Figures C5a and C5c represent a pulse performed at room temperature, and Figures C5b and C5d represent a pulse performed while ramping from 200°C to 800°C at 25°C/min, as indicated by the cyan temperature curve overlaid on the mass spectrometer curves.

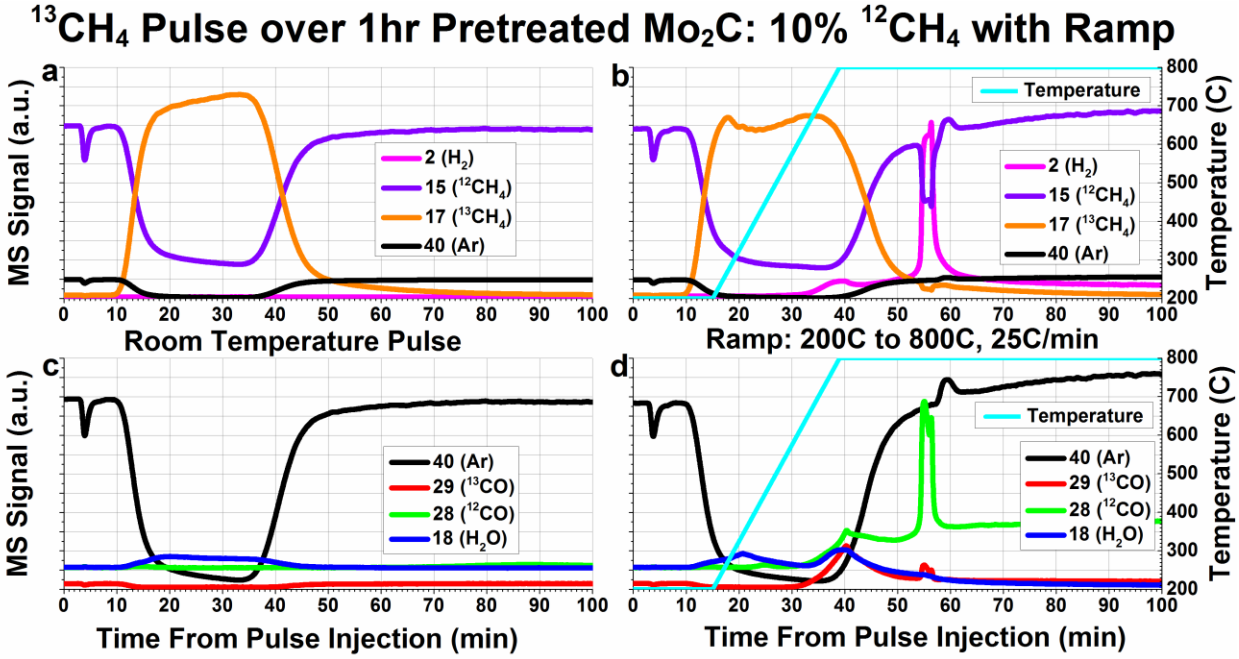

Figure C6: Raw mass spectrometry curves for $^{13}CH_4$ pulses delivered while flowing 18 SCCM He, and 2 SCCM 95% CH_4/5% Ar after 1 hour of H_2 pretreatment at 600°C. Plots for H_2, $^{12}CH_4$, $^{13}CH_4$, and Ar are shown in Figures C6a and C6b. Figures for Ar, ^{12}CO, ^{13}CO, and H_2O are shown in Figures C6c and C6d, and represent a 10x magnification from Figures C6a and C6b. Figures C6a and C6c represent a pulse performed at room temperature, and Figures C6b and C6d represent a pulse performed while ramping from 200°C to 800°C at 25°C/min, as indicated by the cyan temperature curve overlaid on the mass spectrometer curves.

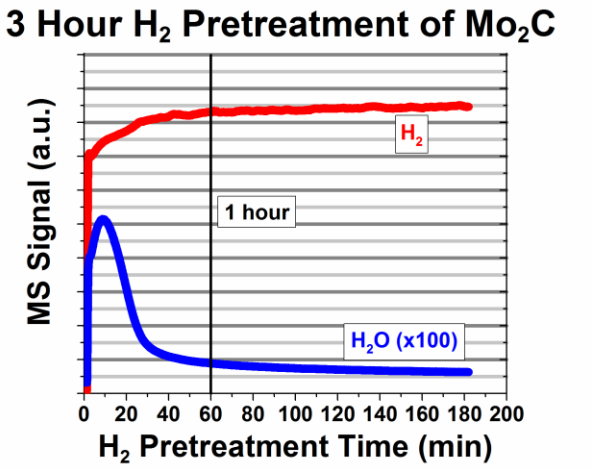

Figure C7: H_2O production during 3 hour H_2 pretreatment of Mo_2C. Line indicated the end of 1 hour of pretreatment, demonstrating the additional oxygenated species that would still be in the catalyst without the 2nd and 3rd hour of pretreatment.

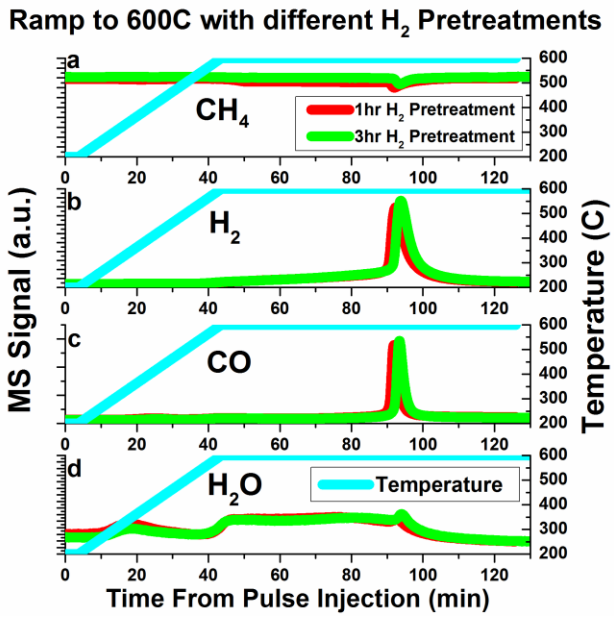

Figure C8: Mass Spectrometry signals of a) 16 (CH_4), b) 2 (H_2), c) 28 (CO), and d) 18 (H_2O) during ramp from 200°C to 600°C at 10°C/min while flowing 5.5 SCCM 95% CH_4/5% Ar. One can notice a small decrease in the CH_4 signal of the 1 hour pretreatment curve compared with the 3 hour pretreatment curve. However, a noticeable increase in H_2, CO, or H_2O production cannot be easily seen.

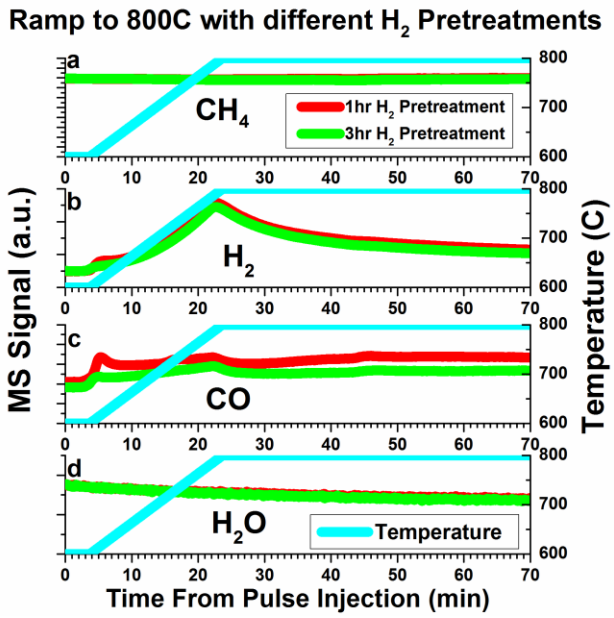

Figure C9: Mass Spectrometry signals of a) 16 (CH_4), b) 2 (H_2), c) 28 (CO), and d) 18 (H_2O) during ramp from 600°C to 800°C at 10°C/min while flowing 5.5 SCCM 95% CH_4/5% Ar. There appears to be the presence of oxygenated species reduced by the flowing methane, and possibly a slightly larger amount in the 1 hour pretreatment sample, as seen in Figure C9b of the H_2 plots and Figure C9c of the CO plots.

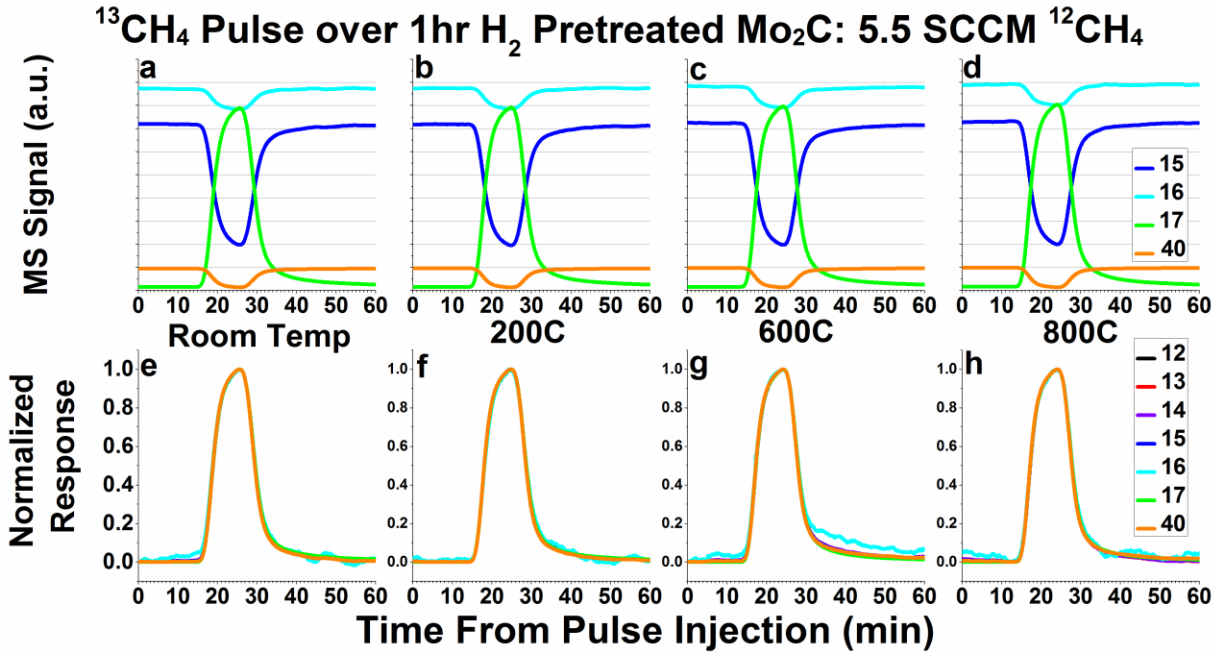

Figure C10: Raw mass spectrometry signals (a-d) and normalized responses (e-h) for $^{13}CH_4$ pulses while flowing 5.5 SCCM 95% CH_4/5% Ar over Mo_2C at room temperature (a & e), 200°C (b & f), 600°C (c & g), and 800°C (d & h). In Figures C10e-C10h, masses 12, 13, 14, 15, and 16 have been inverted in addition to normalized, in order to overlay the pulse response functions. Pretreatment was 50 SCCM flowing H_2 at 600°C for 1 hour. The masses correspond to the following species or fragments: 12: ^{12}C; 13: ^{12}CH, ^{13}C; 14:$^{12}CH_2$, ^{13}CH; 15: $^{12}CH_3$, $^{13}CH_2$; 16: $^{12}CH_4$, $^{13}CH_3$; 17: $^{13}CH_4$; 40: Ar (inert tracer).

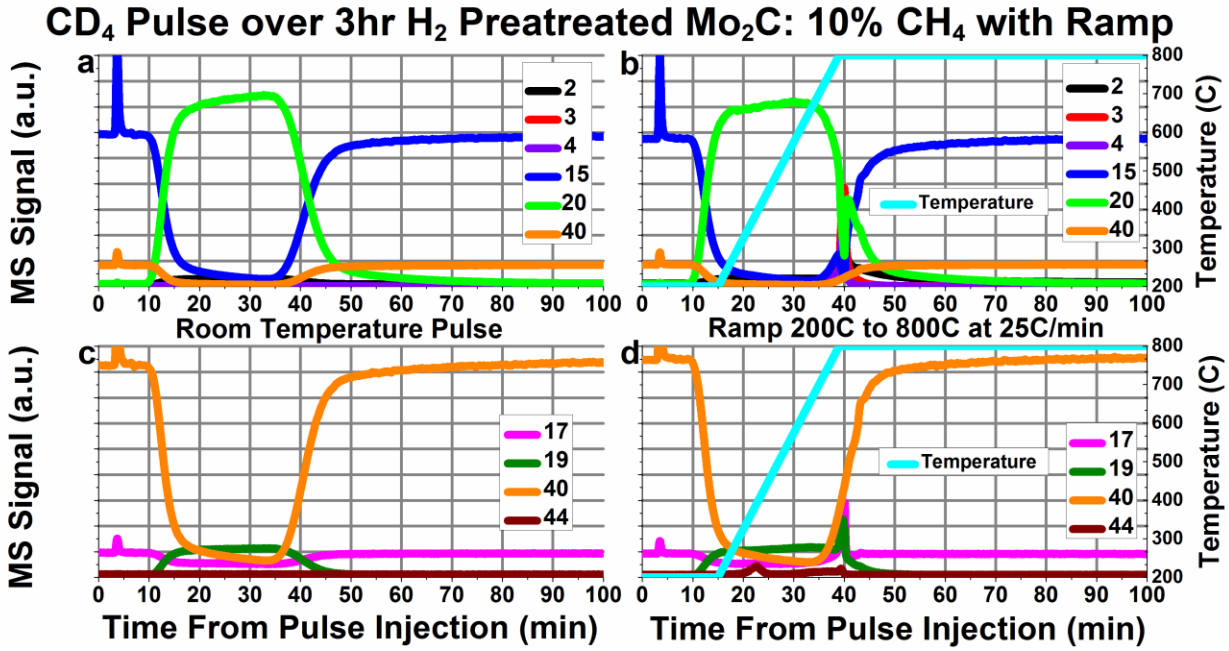

Figure C11: Raw mass spectrometry curves for CD_4 pulses delivered while flowing 18 SCCM He, and 2 SCCM 95% CH_4/5% Ar after 3 hours of H_2 pretreatment at 600°C. Plots for 2 (H_2), 3(HD), 4 (D_2), 15 (CH_4), 20 (CD_4) and 40 (Ar) are shown in Figures C11a and C11b. Figures for 17 (CH_3D and H_2O fragment), 19 (CD_3H and HDO), 40 (Ar), and 44 (CO_2) are shown in Figures C11c and C11d, and represent a 10x magnification from Figures C11a and C11b. Figures C11a and C11c represent a pulse performed at room temperature, and Figures C11b and C11d represent a pulse performed while ramping from 200°C to 800°C at 25°C/min, as indicated by the cyan temperature curve overlaid on the mass spectrometer curves.

References

1 *Annual Energy Outlook*, U.S. Energy Information Administration, 2017.

2 R. H. Crabtree, *Chem. Rev.*, 1995, **95**, 987–1007.

3 E. F. Sousa-Aguiar, F. B. Noronha and A. Faro, Jr., *Catal. Sci. Technol.*, 2011, **1**, 698.

4 D. J. Wilhelm, D. R. Simbeck, A. D. Karp and R. L. Dickenson, *Fuel Process. Technol.*, 2001, **71**, 139–148.

5 J. Ross, in *Heterogeneous Catalysis*, 2012, pp. 47–65.

6 G. Attard and C. Barnes, *Surfaces*, Oxford University Press Inc., New York, 1998.

7 J. Ross, in *Heterogeneous Catalysis*, 2012, pp. 97–123.

8 J. L. Holmes, K. J. Jobst and J. K. Terlouw, *J. Label. Compd. Radiopharm.*, 2007, **50**, 1115–1123.

9 T. Junk and W. J. Catallo, *Chem. Soc. Rev.*, 1997, **26**, 401–406.

10 S. Shannon and J. G. J. Goodwin, *Chem. Rev.*, 1995, **95**, 677–695.

11 C. Ledesma, J. Yang, D. Chen and A. Holmen, *ACS Catal.*, 2014, **4**, 4527–4547.

12 A. J. Brush, M. Pan and C. B. Mullins, *J. Phys. Chem. C*, 2012, **116**, 20982–20989.

13 A. Brush, E. J. Evans, G. M. Mullen, K. Jarvis and C. B. Mullins, *Fuel Process. Technol.*, 2016, **153**, 111–120.

14 A. Brush, S. McDonald, R. DuPre, S. Kota, G. M. Mullen and C. B. Mullins, *Submitt. React. Chem. Eng.*, 2017.

15 A. Brush, G. M. Mullen, R. Dupré, S. Kota and C. B. Mullins, *React. Chem. Eng.*, 2016, **1**, 667–674.

16 A. S. K. Hashmi and G. J. Hutchings, *Angew. Chem. Int. Ed.*, 2006, **45**, 7896–7936.

17 M. Haruta, *Catal. Today*, 1997, **36**, 153–166.

18 M. Haruta, T. Kobayashi, H. Sano and N. Yamada, *Chem. Lett.*, 1987, 405–408.

19 M. Haruta, N. Yamada, T. Kobayashi and S. Iijima, *J. Catal.*, 1989, **115**, 301–309.

20 G. C. Bond, P. A. Sermon, G. Webb, D. A. Buchanan and P. B. Wells, *J. Chem. Soc., Chem. Commun.*, 1973, **13**, 444–445.

21 B. Nkosi, M. D. Adams, N. J. Coville and G. J. Hutchings, *J. Catal.*, 1991, **386**,

378–386.

22 M. Date and M. Haruta, *J. Catal.*, 2001, **201**, 221–224.

23 F. Boccuzzi, A. Chiorino, M. Manzoli, P. Lu, T. Akita, S. Ichikawa and M. Haruta, *J. Catal.*, 2001, **202**, 256–267.

24 Q. Fu, H. Saltsburg and M. Flytzani-Stephanopoulos, *Science (80-.).*, 2003, **301**, 935–8.

25 Q. Fu, A. Weber and M. Flytzani-Stephanopoulos, *Catal. Lett.*, 2001, **77**, 87–95.

26 P. Claus, *Appl. Catal. A-Gen.*, 2005, **291**, 222–229.

27 L. McEwan, M. Julius, S. Roberts and J. C. Q. Fletcher, *Gold Bull.*, 2010, **43**, 298–306.

28 A. Corma and P. Serna, *Science (80-.).*, 2006, **313**, 332–334.

29 C. Mohr, H. Hofmeister, J. Radnik and P. Claus, *J. Am. Chem. Soc.*, 2003, **125**, 1905–1911.

30 J. Gong, R. A. Ojifinni, T. S. Kim, J. M. White and C. B. Mullins, *J. Am. Chem. Soc.*, 2006, **128**, 9012–9013.

31 T. Yan, J. Gong and C. B. Mullins, *J. Am. Chem. Soc.*, 2009, **131**, 16189–16194.

32 X. Deng and C. M. Friend, *J. Am. Chem. Soc.*, 2005, **127**, 17178–17179.

33 J. Gong, D. W. Flaherty, T. Yan and C. B. Mullins, *ChemPhysChem*, 2008, **9**, 2461–2466.

34 J. Gong and C. B. Mullins, *Accounts. Chem. Res.*, 2009, **42**, 1063–1073.

35 M. Pan, D. W. Flaherty and C. B. Mullins, *J. Phys. Chem. Lett.*, 2011, **2**, 1363–1367.

36 X. Deng and C. M. Friend, *Surf. Sci.*, 2008, **602**, 1066–1071.

37 M. Boronat, P. Concepción, A. Corma, S. González, F. Illas and P. Serna, *J. Am. Chem. Soc.*, 2007, **129**, 16230–16237.

38 T. Fujitani, I. Nakamura, T. Akita, M. Okumura and M. Haruta, *Angew. Chem. Int. Ed.*, 2009, **48**, 9515–9518.

39 B. Hammer and J. K. Norskov, *Nature*, 1995, **376**, 238–240.

40 A. G. Sault and R. J. Madix, *Surf. Sci.*, 1986, **169**, 347–356.

41 M. Pan, Z. D. Pozun, W.-Y. Yu, G. Henkelman and C. B. Mullins, *J. Phys. Chem. Lett.*, 2012, **3**, 1894–1899.

42 G. Kok, A. Noordermeer and B. E. Nieuwenhuys, *Surf. Sci.*, 1983, **135**, 65–80.

43 D. W. Goodman, J. T. Yates and T. Madey, *Surf. Sci.*, 1980, **93**, L135–L142.

44 H. Sakurai and M. Haruta, *Appl. Catal. A-Gen.*, 1995, **127**, 93–105.

45 A. Gazsi, A. Koós, T. Bánsági and F. Solymosi, *Catal. Today*, 2011, **160**, 70–78.

46 A. Gazsi, T. Bánsági and F. Solymosi, *Catal. Lett.*, 2009, **131**, 33–41.

47 M. Pan, A. J. Brush, G. Dong and C. B. Mullins, *J. Phys. Chem. Lett.*

48 A. E. Baber, T. J. Lawton and E. C. H. Sykes, *J. Phys. Chem. C*, 2011, **115**, 9157–9163.

49 J. E. Davis, S. G. Karseboom, P. D. Nolan and C. B. Mullins, *J. Chem. Phys.*, 1996, **105**, 8362–8375.

50 M. Bartram and B. E. Koel, *Surf. Sci.*, 1989, **213**, 137–156.

51 K. H. Bornscheuer, S. R. Lucas, W. J. Choyke, W. D. Partlow and J. T. Yates, *J. Vac. Sci. Technol. A*, 1993, **11**, 2822–2826.

52 U. Bischler and E. Bertel, *J. Vac. Sci. Technol. A*, 1993, **11**, 458–460.

53 J. V. Barth, H. Brune, G. Ertl and R. J. Behm, *Phys. Rev. B*, 1990, **42**, 9307–9318.

54 C. Woll, S. Chiang, R. J. Wilson and P. H. Lippel, *Phys. Rev. B*, 1989, **39**, 7988–7991.

55 B. K. Min, A. R. Alemozafar, D. Pinnaduwage, X. Deng and C. M. Friend, *J. Phys. Chem. B*, 2006, **110**, 19833–19838.

56 B. K. Min, X. Deng, D. Pinnaduwage, R. Schalek and C. M. Friend, *Phys. Rev. B*, 2005, **72**, 121410.

57 J. Gong, D. W. Flaherty, R. A. Ojifinni, J. M. White and C. B. Mullins, *J. Phys. Chem. C*, 2008, **112**, 5501–5509.

58 D. Ehlers, A. Spitzer and H. Luth, *Surf. Sci.*, 1985, **160**, 57–69.

59 J. Matthiesen, R. S. Smith and B. D. Kay, *J. Phys. Chem. Lett.*, 2011, **2**, 557–561.

60 R. S. Smith, P. Ayotte and B. D. Kay, *J. Chem. Phys.*, 2007, **127**, 244705.

61 R. B. Levy and M. Boudart, *Science (80-.).*, 1973, **181**, 547–549.

62 H. H. Hwu and J. G. Chen, *Chem. Rev.*, 2005, **105**, 185–212.

63 J. G. Chen, B. Fruhberger, J. Eng, Jr. and B. E. Bent, *J. Mol. Catal. A Chem.*, 1998, **131**, 285–299.

64 J. G. Chen, *Chem. Rev.*, 1996, **96**, 1477–1498.

65 A.-M. Alexander and J. S. J. Hargreaves, *Chem. Soc. Rev.*, 2010, **39**, 4388–4401.

66 L. Leclercq, M. Provost, H. Pastor, J. Grimblot, A. M. Hardy, L. Gengembre and G. Leclercq, *J. Catal.*, 1989, **117**, 371–383.

67 L. Leclercq, M. Provost, H. Pastor and G. Leclercq, *J. Catal.*, 1989, **117**, 384–395.

68 A. Hanif, T. Xiao, A. P. E. York, J. Sloan and M. L. H. Green, *Chem. Mater.*, 2002, **14**, 1009–1015.

69 J. Sehested, C. J. H. Jacobsen, S. Rokni and J. R. Rostrup-Nielsen, *J. Catal.*, 2001, **201**, 206–212.

70 J. Patt, D. J. Moon, C. Phillips and L. Thompson, *Catal. Letters*, 2000, **65**, 193–195.

71 N. M. Schweitzer, J. A. Schaidle, O. K. Ezekoye, X. Pan, S. Linic and L. T. Thompson, *J. Am. Chem. Soc.*, 2011, **133**, 2378–2381.

72 J. B. Claridge, A. P. E. York, A. J. Brungs, C. Marquez-Alvarez, J. Sloan, S. C. Tsang and M. L. H. Green, *J. Catal.*, 1998, **100**, 85–100.

73 A. P. E. York, J. B. Claridge, A. J. Brungs, S. C. Tsang and M. L. H. Green, *Chem. Commun.*, 1997, 39–40.

74 A. J. Brungs, A. P. E. York, J. B. Claridge, C. Marquez-Alvarez and M. L. H. Green, *Catal. Letters*, 2000, **70**, 117–122.

75 B. K. Min and C. M. Friend, *Chem. Rev.*, 2007, **107**, 2709–24.

76 T. Xiao, A. Hanif, A. P. E. York, Y. Nishizaka and M. L. H. Green, *Phys. Chem. Chem. Phys.*, 2002, **4**, 4549–4554.

77 T. Xiao, H. Wang, J. Da, K. S. Coleman and M. L. H. Green, *J. Catal.*, 2002, **211**, 183–191.

78 S. S.-Y. Lin, W. J. Thomson, T. J. Hagensen and S. Y. Ha, *Appl. Catal. A Gen.*, 2007, **318**, 121–127.

79 A. R. S. Darujati and W. J. Thomson, *Appl. Catal. A Gen.*, 2005, **296**, 139–147.

80 A. C. Lausche, J. a. Schaidle and L. T. Thompson, *Appl. Catal. A Gen.*, 2011, **401**, 29–36.

81 A. R. S. Darujati, D. C. LaMont and W. J. Thomson, *Appl. Catal. A Gen.*, 2003, **253**, 397–407.

82 D. C. LaMont, A. J. Gilligan, A. R. . Darujati, A. S. Chellappa and W. J. Thomson, *Appl. Catal. A Gen.*, 2003, **255**, 239–253.

83 T. Xiao, A. Hanif, A. P. E. York and M. L. H. Green, *Catal. Today*, 2009, **147**, 196–202.

84 D. C. LaMont and W. J. Thomson, *Chem. Eng. Sci.*, 2005, **60**, 3553–3559.

85 D. C. Lamont and W. J. Thomson, *Appl. Catal. A Gen.*, 2004, **274**, 173–178.

86 J. Cheng and W. Huang, *Fuel Process. Technol.*, 2010, **91**, 185–193.

87 C. Shi, A. Zhang, X. Li, S. Zhang, A. Zhu, Y. Ma and C. Au, *Appl. Catal. A Gen.*, 2012, **431**–**432**, 164–170.

88 A. Zhang, A. Zhu, B. Chen, S. Zhang, C. Au and C. Shi, *Catal. Commun.*, 2011, **12**, 803–807.

89 K. T. Jung, W. B. Kim, C. H. Rhee and J. S. Lee, *Chem. Mater.*, 2004, **16**, 307–314.

90 T. Xiao, A. P. E. York, H. Al-megren, C. V. Williams, H.-T. Wang and M. L. H. Green, *J. Catal.*, 2001, **109**, 100–109.

91 S. Izhar, H. Kanesugi, H. Tominaga and M. Nagai, *Appl. Catal. A Gen.*, 2007, **317**, 82–90.

92 J. Wei and E. Iglesia, *J. Catal.*, 2004, **224**, 370–383.

93 C. Liu, J. Ye, J. Jiang and Y. Pan, *ChemCatChem*, 2011, **3**, 529–541.

94 A. P. E. York, T. Xiao, M. L. H. Green and J. B. Claridge, *Catal. Rev.*, 2007, **49**, 511–560.

95 D. L. Trimm, *Catal. Today*, 1997, **37**, 233–238.

96 M. C. J. Bradford and M. A. Vannice, *Appl. Catal. A Gen.*, 1996, **142**, 73–96.

97 J. Sehested, *Catal. Today*, 2006, **111**, 103–110.

98 O. Muraza and A. Galadima, *Int. J. Energy Res.*, 2015, **39**, 1196–1216.

99 C. Shi, S. Zhang, X. Li, A. Zhang, M. Shi, Y. Zhu, J. Qiu and C. Au, *Catal. Today*, 2014, **233**, 46–52.

100 Q. Zhu, B. Zhang, J. Zhao, S. Ji, J. Yang, J. Wang and H. Wang, *J. Mol. Catal. A Chem.*, 2004, **213**, 199–205.

101 M. Nagai, A. M. Zahidul and K. Matsuda, *Appl. Catal. A Gen.*, 2006, **313**, 137–145.

102 J. L. G. Fierro, *Catal. Letters*, 1993, **22**, 67–91.

103 D. Pakhare and J. Spivey, *Chem. Soc. Rev.*, 2014, **43**, 7813–7837.

104 P. M. Mortensen and I. Dybkjær, *Appl. Catal. A Gen.*, 2015, **495**, 141–151.

105 H. Al-Megeren and T. Xiao, in *Advances in Natural Gas Technology*, ed. H. Al-Megeren, InTech, 2012, pp. 387–406.

106 J. Chase, M. W., *J. Phys. Chem. Ref. Data, Monogr. 9*, 1998.

107 J. J. English, in *Binary and Ternary Phase Diagrams of Cb, Mo, Ta, and W, DMIC Rep. 152*, 1961, p. 41.

108 L. Brewer and R. H. Lamoreaux, in *Binary Alloy Phase Diagrams, Vol. 3*, ed. T. B. Massalski, II., 1990, pp. 2639–2641.

109 A. N. R. Bos, L. Lefferts, G. B. Marin and M. H. G. M. Steijns, *Appl. Catal. A Gen.*, 1997, **160**, 185–190.

110 C. Mirodatos, *Catal. Today*, 1991, **9**, 83–95.

111 R. J. Berger, F. Kapteijn, J. A. Moulijn, G. B. Marin, J. De Wilde, M. Olea, D. Chen, A. Holmen, L. Lietti, E. Tronconi and Y. Schuurman, *Appl. Catal. A Gen.*, 2008, **342**, 3–28.

112 J. Happel, *Chem. Eng. Sci.*, 1978, 33.

113 J. Happel, I. Suzukl, P. Kokayeff and V. Fthenakis, *J. Catal.*, 1980, **65**, 59–77.

114 J. Happel, H. Y. Cheh, M. Otarod, S. Ozawa, A. J. Severdia, T. Yoshida and V. Fthenakis, *J. Catal.*, 1982, **75**, 314–328.

115 C. O. Bennett, *Catal. Rev.*, 1976, **13**, 121–148.

116 P. Biloen, *J. Mol. Catal. A Chem.*, 1983, **21**, 17–24.

117 D. NIST Mass Spec Data Center, S.E. Stein, in *NIST Chemistry WebBook, NIST Standard Reference Database Number 69*.

118 H. Shou and R. J. Davis, *J. Catal.*, 2013, **306**, 91–99.

119 N. Lohitharn and J. G. Goodwin, *Catal. Commun.*, 2009, **10**, 758–762.

120 J. Gao, X. Mo and J. G. Goodwin, *J. Catal.*, 2010, **275**, 211–217.

121 D. M. Stockwell and C. O. Bennett, *J. Catal.*, 1988, **110**, 354–363.

122 D. M. Stockwell, J. S. Chung and C. O. Bennett, *J. Catal.*, 1988, **112**, 135–144.

123 S. Hanspal, Z. D. Young, H. Shou and R. J. Davis, *ACS Catal.*, 2015, 1737–1746.

124 Y. Qi, J. Yang, D. Chen and A. Holmen, *Catal. Letters*, 2015, **145**, 145–161.

125 C. Ledesma, J. Yang, E. A. Blekkan, A. Holmen and D. Chen, *ACS Catal.*, 2016, **6**, 6674–6686.

126 T. Xiao, A. P. E. York, K. S. Coleman, J. B. Claridge, J. Sloan, J. Charnock and M. L. H. Green, 2001, 3094–3098.

127 A. J. Medford, A. Vojvodic, F. Studt, F. Abild-Pedersen and J. K. Nørskov, *J. Catal.*, 2012, **290**, 108–117.

128 H. Tominaga and M. Nagai, *Appl. Catal. A Gen.*, 2007, **328**, 35–42.

129 P. Liu and J. A. Rodriguez, *J. Phys. Chem. B*, 2006, **110**, 19418–19425.

130 X. R. Shi, S. G. Wang and J. Wang, *J. Mol. Catal. A Chem.*, 2016, **417**, 53–63.

131 S. Naito, A. Takada, S. Tokizawa and T. Miyao, *Appl. Catal. A Gen.*, 2005, **289**, 22–27.

Vita

Adrianna Brush grew up in Cincinnati, Ohio, and attended Walnut Hills High School. She attended the University of California, Berkeley for undergraduate studies, and graduated with B.S. in Chemical Engineering in 2008. She worked at the Clorox Company, then Lawrence Berkeley National Laboratory until she started her graduate work at the University of Texas, Austin in the Mullins lab in 2011. In 2016, she came out as an openly transgender woman. She is proud that her entire education, from kindergarten through PhD has been at public schools.

Email: adrianna.brush@gmail.com

This dissertation was typed by Adrianna Brush